SHEAR-INDUCED MICROSTRUCTURE IN HOLLOW FIBER MEMBRANE DOPES

A Thesis
Presented to
The Academic Faculty

By

Emily Cassidy Peterson

In Partial Fulfillment
Of the Requirements for the Degree
Doctor of Philosophy in the
School of Chemical and Biomolecular Engineering

Georgia Institute of Technology
December 2013

SHEAR-INDUCED MICROSTRUCTURE IN HOLLOW FIBER MEMBRANE DOPES

Approved by:

Dr. Victor Breedveld, Advisor
School of Chemical & Biomolecular Engineering
Georgia Institute of Technology

Dr. William Koros
School of Chemical & Biomolecular Engineering
Georgia Institute of Technology

Dr. Sven Behrens
School of Chemical & Biomolecular Engineering
Georgia Institute of Technology

Dr. Carson Meredith
School of Chemical & Biomolecular Engineering
Georgia Institute of Technology

Dr. David Bucknall
School of Materials Science & Engineering
Georgia Institute of Technology

Date Approved: August 13, 2013

Dedicated to my uncle and godfather,

Gary W. Kingry

ACKNOWLEDGEMENTS

I would like to express my appreciation to all those who have assisted me in completing this thesis. First, I would like to thank my advisor, Dr. Victor Breedveld. It has been a privilege to work under the mentorship of such a talented teacher and researcher. His enthusiasm for learning has made this process truly enjoyable and rewarding. I would also like to thank my committee members, Dr. Bill Koros, Dr. Sven Behrens, Dr. David Bucknall, and Dr. Carson Meredith, for the helpful guidance they provided in the course of this work.

I am very grateful to have had the opportunity to work with the many talented members of the Complex Fluids Research Group who have made my time at Georgia Tech memorable and fun: Kyung Hee Oh, Dr. Lester Li, Dr. Balamurali Balu, Dr. Kayode Olanrewaju, Dr. Tracie Owens, Sricharan Yarlagadda, Zhenguan Tang, Won Tae Choi, and Dr. Vikram Prasad. It was also a pleasure to work with the many undergraduate students who have been a part of the group, especially Sean Patterson, who assisted me with my experiments last summer.

This work would not have been possible without the love and support of my friends and family. I cannot imagine the past four years without the friendship of Amy Ethier; without her, I certainly could not have survived the stress of graduate school and four years away from home. I would also like to thank Megan Brown for her unfailing friendship, even when distance and busy schedules made it difficult. I thank my sister, Molly Schottelkotte, who supported me, made me laugh, and cheered me on during both successes and struggles. I also owe a wealth of gratitude to my uncle and aunt, Gary and

Maureen Kingry. Gary inspired me to enter the field of chemical engineering, and the encouragement and support they have provided is immeasurable. Words could never express the gratitude I owe my parents, Dominic and Eileen Peterson. From the very beginning, they have believed in me and supported me in every endeavor. Every child should be so lucky. I would also like to acknowledge my grandparents, Larry and Olivia Cassidy and Bill and Rosemary Peterson, for their example of a life filled with faith, family, and ambition. To the many other family members and friends who have offered prayers and kind words of encouragement—thank you!

Most importantly, I would like to thank my best friend and fiancé, Dane Blackburn. More so than anyone, he provided day-to-day encouragement and a constant reminder of life beyond research. I could never express my gratitude for his love, perspective, sense of humor, and his incredible patience.

TABLE OF CONTENTS

ACKNOWLEDGEMENTS iv

LIST OF TABLES x

LIST OF FIGURES xi

NOMENCLATURE xv

SUMMARY xviii

1. INTRODUCTION 1

1.1 Rheology & Hollow Fiber Membrane Spinning 1

1.1.1 Hollow Fiber Spinning 2

1.1.2 Fiber Microstructure 5

1.2 Polymer Effects: Shear History & Shear-Induced Demixing 8

1.2.1 Considering Shear History 8

1.2.2 Shear-Induced Demixing 10

1.3 Particle Effects: Shear-Induced Aggregation & Orientation 14

1.3.1 Flow-Oriented Structure 17

1.3.2 Vorticity-Oriented Structure 20

1.4 Particle Effects: Shear-Induced Migration 23

1.5 Objectives & Thesis Overview 27

2. SHEAR-INDUCED DEMIXING IN POLYMERIC MEMBRANE DOPES 29

2.1 Introduction 29

2.2 Materials and Methods 31

2.2.1 Dope Preparation 31

2.2.2 Shear History Control 32

2.2.3 Shear-SALS Experiments 33

2.2.4 Extrusion Experiments 35

2.3 Results and Discussion 37

2.4 Conclusions 48

3. SHEAR-INDUCED AGGREGATION AND VORTICITY ORIENTATION 49

3.1 Introduction 49

3.2 Materials and Methods 51

3.2.1 Sample Preparation 51

3.2.2 Rheology & Shear-SALS Experiments 53

3.2.3 SALS Pattern Analysis 54

3.3 Results and Discussion 54

3.3.1 Viscosity and First Normal Stress Difference 54

3.3.2 Shear-SALS 55

3.3.2.1 Effect of Structure Formation Shear Rate 55

3.3.2.2 Effect of Recovery Shear Conditions 64

3.3.2.3 Shear-Enhanced Concentration Fluctuations & Their Effect on Particle Structure 67

3.3.2.4 Viscosity and Intensity Effects 70

3.3.2.5. Effect of Particle Concentration 75

3.3.2.6. Structure Formation in a Boger Fluid Suspension 77

3.4. Conclusions 79

4. VISCOELASTICITY-INDUCED PARTICLE MIGRATION 81

4.1 Introduction 81

4.2 Materials and Methods 83

4.2.1 Suspension Preparation 83

4.2.2 Experimental Setup 85

4.2.3 Image Analysis 88

4.3 Results 91

4.3.1 Suspending Fluid Rheology 91

4.3.2 Migration Results 92

4.3.2.1 Ultem®-Luvitec® Suspension 92

4.3.2.2 Ultem® 23.5% Suspension 98

4.3.2.3 Boger Fluid Suspension 102

4.4 Discussion 105

4.4.1 Ultem® 30% Suspension 107

4.4.2 String Formation 111

4.4.3 A Note Regarding the Boger Fluid Observations 112

4.4.4 Implications for Mixed Matrix Fiber Spinning 113

4.5 Conclusions 116

5. CONCLUSIONS AND RECOMMENDATIONS 118

5.1 Polymer Effects: Shear History & Shear-Induced Demixing 119

5.2 Particle Effects: Shear-Induced Aggregation & Orientation 121

5.3 Particle Effects: Shear-Induced Migration 125

REFERENCES 129

VITA.....140

LIST OF TABLES

Table 1.1 A table reproduced from Rangel-Nafaile et al. summarizing many of the early observations of shear-induced demixing [49]. 13

Table 2.1 Shear rate profile for step-shear experiments..... 35

Table 4.1 The volumetric flow rates used and the corresponding wall shear rates..... 87

LIST OF FIGURES

Figure 1.1 Schematic diagram of the polymeric hollow fiber spinning process..... 3

Figure 1.2 Schematic of a dual-layer, mixed matrix fiber spinning operation. 4

Figure 1.3 SEM micrograph illustrating the asymmetric nature of a hollow fiber membrane, from [20]. 5

Figure 1.4 Hollow fiber containing many macrovoids, from [22]. 6

Figure 1.5 Diagram showing the flow geometry and appearance of opacity in the experiments of Ver Strate and Philippoff [45]. 11

Figure 1.6 Progression of flow-oriented string formation observed by Michele et al.; the suspension consisted of 60-70 μm glass spheres in an aqueous polyacrylamide solution (0.5%) [19]. 15

Figure 1.7 Diagram illustrating the selectivity benefits of large aspect ratio molecular sieves that are aligned perpendicular to the gas transport direction. 16

Figure 1.8 Various microstructures observed by Scirocco et al.: (a) flow-oriented strings in a shear-thinning solution; (b) flow-oriented bundles in a solution with a Weissenberg ratio much greater than (a); (c) homogeneous distribution of particles in a Boger fluid [67]. 18

Figure 1.9 Structure observed by Won and Kim for non-colloidal particles in a Boger fluid under reciprocating shear [69]. 19

Figure 1.10 Simulation results from Santos de Oliveira et al. showing the development of strings of particles suspended in a wormlike micelle solution [70]..... 20

Figure 1.11 Definition of flow, gradient, and vorticity axes in simple shear flow. 21

Figure 1.12 Optical image (left) and characteristic butterfly scattering pattern illustrating the aggregated, vorticity-oriented structure formed due to shear [72]. 21

Figure 1.13 Line spectra showing the distribution of zeolites as a function of radial location in the fiber wall for four different air gaps: (a) 0 cm, (b) 1.5 cm, (c) 2.5 cm, and (d) 6 cm [90]. 25

Figure 2.1 Shear-SALS setup..... 34

Figure 2.2 SALS patterns recorded during step-shear experiments for seven different syringe-loading rates. The first six columns are time-averaged patterns for

the entire two-minute shear interval. The last column contains images obtained after shear was stopped. The scale bar indicates a scattering vector of 1 μm^{-1} 38

Figure 2.3 Intensity vs. time profiles for the step-shear experiments shown in Figure 2.2. For each experiment, the inset shows the average pattern for minutes 10-12. 39

Figure 2.4 The upper data set shows the normalized SALS pattern intensity resulting from step-shear experiments conducted using seven different syringe speeds. The lower data show the macrovoid count from the corresponding extrusion experiments. 42

Figure 2.5 SEM images illustrating the effect of shear history on macrovoid formation; the fibers were extruded after filling syringes with shear rates of (a) 4.1 s^{-1} and (b) 3.7 s^{-1}. 43

Figure 2.6 Image intensity as a function of time for two step-shear experiments. One was loaded using a 'nucleating' syringe rate and immediately thereafter was subjected to the shear-step profile described in Table 2.1 (blue line). The other (red line) was loaded at the same nucleating shear rate, sheared at a 'mixing' shear rate of 0.8 s^{-1} for 20 minutes and *then* subjected to the same step-shear profile. The beginning of the step-shear portion of the experiment corresponds to $t = 0$ s. 45

Figure 3.1 Viscosity (open symbols; left vertical axis) and N_1 (closed symbols; right axis) for the Ultem® solution (triangles) and Boger fluid (circles). The arrows labeled a, b, c, and d indicate the four shear rates that were used during Interval 1 for the experiments discussed in Section 3.3.2.1. 55

Figure 3.2 Evolution of alignment factor $A_{f,ave.}$ for four different Interval 1 shear rates. In the SALS image insets, the vertical direction represents the flow (x) direction, and the horizontal direction is the vorticity (z) direction. The shaded regions represent Interval 1. 57

Figure 3.3 Intensity vs. q for the butterfly patterns observed at the beginning of Interval 2, for the 30 and 60 s^{-1} experiments. The black lines represent the profiles for the 30 s^{-1} experiment, while the gray lines are from the 60 s^{-1} experiment. The butterfly pattern observed in the 30 s^{-1} case was larger, resulting in larger intensities over the entire q range. 60

Figure 3.4 (a) Comparison of $A_{f,ave.}$ during the recovery interval for four different Interval 1 shear rates. In all cases, the recovery shear rate was 0.3 s^{-1}; (b) sketch illustrating the transition from vorticity to flow orientation, followed by an isotropic structure. 62

Figure 3.5 $A_{f,ave.}$ as a function of time for experiments in which Interval 2 conditions were varied. The inset shows $A_{f,ave.}$ as a function of total deformation. 67

Figure 3.6 Alignment factor as a function of scattering vector for two representative patterns obtained during Interval 1 of the experiment shown in Figure 3.2(c) (Interval 1 shear rate = 30 s^{-1}); these images demonstrate the effect of shear-enhanced concentration fluctuations in the continuous phase on the average alignment factor, which accounts for the noise observed in the first minute of the experiment. 69

Figure 3.7 $A_{f,ave.}$ evolution for two experiments with identical samples and shear conditions (5 wt.% silica; Interval 1 shear rate of 30 s^{-1} and Interval 2 shear rate of 0.3 s^{-1}); the difference between the two experiments is that in one case, shear-enhanced concentration fluctuations caused $A_{f,ave.}$ to be negative (gray line) in Interval 1, while in the other case (black line), without the fluctuations, $A_{f,ave.}$ was positive. 70

Figure 3.8 Measured viscosity and intensities during the recovery interval after an Interval 1 shear rate of 30 s^{-1}. In (a), the recovery shear rate was 0.3 s^{-1} and in (b), it was 0.6 s^{-1}. 72

Figure 3.9 Viscosity and intensities measured at a low shear rate before and after one minute of (a) shear at 30 s^{-1} and (b) rest. 75

Figure 3.10 $A_{f,ave}$ measured for two different silica concentrations. The gray line represents a sample containing 5 wt.% silica, and the black line 0.5 wt.%; the Interval 1 shear rate was 30 s^{-1} and the Interval 2 shear rate was 0.3 s^{-1}. 76

Figure 3.11 $A_{f,ave.}$ during Interval 2 for a Boger fluid suspension (black line), with the previously discussed Ultem® result shown for comparison. 78

Figure 4.1 The two potential results of sieve migration in the annular spinneret channel: (a) migration towards the centerline and (b) migration toward the walls. 82

Figure 4.2 Coordinate definitions and capillary dimensions (not to scale). 85

Figure 4.3 Example of a section of an intensity profile exhibiting an "edge peak". 90

Figure 4.4 Flow curves for the four fluids used in this study. Open symbols are the viscosity (left axis) and closed symbols are N_1 (right axis). 92

Figure 4.5 Intensity profiles for the Ultem®-Luvitec® suspension. 94

Figure 4.6 Confocal images and the corresponding intensity profiles showing (a) the uniform particle distribution obtained at 3 s^{-1} and (b) the particle distribution from the 500 s^{-1} experiment, in which particles accumulated in the center. Both images were obtained at L/d = 900. 95

Figure 4.7 Profile focusing for the Ultem®-Luvitec® suspension. 96

Figure 4.8 Center peak analysis for the Ultem®-Luvitec® suspension. 97

Figure 4.9 Edge peak analysis for the Ultem®-Luvitec® suspension. 97

Figure 4.10 Intensity profiles for the 23.5% Ultem® suspension. 99

Figure 4.11 Confocal images showing the particle distribution observed in the 23.5% Ultem® suspension at shear rates of (a) 500 s^{-1} and (b) 1000 s^{-1}. Images on the right (which have been inverted for clarity) show the particle strings observed at the walls. 100

Figure 4.12 Profile focusing analysis for the Ultem® 23.5% suspension. 101

Figure 4.13 Center peak analysis for the Ultem® 23.5% suspension. 102

Figure 4.14 Edge peak analysis for the Ultem® 23.5% suspension. 102

Figure 4.15 Intensity profiles for the Boger fluid suspension. 103

Figure 4.16 Profile focusing analysis for (a) the Boger fluid suspension and (b) the Boger fluid, Ultem®-Luvitec®, and Ultem® 23.5% suspensions at L/d = 900. .. 104

Figure 4.17 Center peak analysis for the Boger fluid suspension. 104

Figure 4.18 Edge peak analysis for the Boger fluid suspension. 105

Figure 4.19 Comparison of the 23.5% and 30% Ultem® suspensions in terms of (a) profile focusing, (b) p_{center}, and (c) p_{edge}. 108

Figure 4.20 Pathline analysis of a Boger fluid flowing through a capillary; the bent streamlines at the advancing front of the fluid illustrate the secondary recirculation flows in this region. 113

Figure 4.21 Confocal images showing fibers extruded and phase separated using shear rates of 3 and 500 s^{-1}; the upper images show the fiber cross sections, while the lower images show the outer surfaces of the fibers. 116

NOMENCLATURE

A_f	alignment factor
$A_{f,ave.}$	average alignment factor
$A_{occ.}$	percentage of the channel cross-sectional area occupied by particles in shear-induced migration experiments
d	gap size in slit flow
h	gap size, either in slit flow or parallel plate measurements
I	intensity
$I_{ave.}$	average intensity
I_{flow}	intensity along the flow direction in light scattering
$I_{vort.}$	intensity along the vorticity direction in light scattering
L	total channel length, or distance along a channel
M_n	number-average molecular weight
M_v	viscosity-average molecular weight
M_w	weight-average molecular weight
n	shear-thinning index
N_1	first normal stress difference
NMP	n-methyl-2-pyrrolidone
PB	polybutene
p_{center}	ratio quantifying the presence of a peak at the center of an intensity profile
p_{edge}	ratio quantifying the presence of peaks at the edges of an intensity profile
PIB	polyisobutene

PS	polystyrene
Q	volumetric flow rate
q	scattering vector
R	tube radius
r^*	radial position denoting the boundary between the center- and wall-attractive regions, as used by D'Avino et al.
SEM	scanning electron microscopy
SEM-EDX	scanning electron microscopy with energy-dispersive X-ray spectroscopy
shear-SALS	shear-small-angle light scattering
t	time
THF	tetrahydrofuran
$t_{res.}$	average residence time of a fluid in a channel
v	velocity
v_x	velocity profile in the x direction
$\langle v_x \rangle$	average velocity in the x direction
x	velocity axis in simple shear or pressure-driven flow
y	velocity gradient axis in simple shear or pressure-driven flow
y'	normalized y position in slit flow
y_{max}	distance between the first and last particles in migration experiments
z	vorticity axis in simple shear or pressure-driven flow
γ	strain
$\dot{\gamma}$	shear rate
$\dot{\gamma}_{max}, \dot{\gamma}_{wall}$	maximum or wall shear rate in pressure driven flow
$\dot{\gamma}_{wall,app.}$	apparent wall shear rate in pressure driven flow

$\dot{\gamma}_{wall,corr.}$	wall shear rate, corrected for shear-thinning effects, in pressure-driven flow
η	viscosity
φ	azimuthal angle in light scattering
θ	scattering angle
τ, τ_c	characteristic time scale

SUMMARY

Hollow fiber membranes offer the opportunity to dramatically reduce the energy required to perform gas separations in the chemical industry. The membranes are fabricated from highly non-Newtonian precursor materials, including concentrated polymer solutions that sometimes also contain dispersed particles. These materials are susceptible to shear-induced microstructural changes during processing, which can affect the characteristics of the resulting membrane. This thesis explores several shear-related effects using materials and flow conditions that are relevant for fiber spinning. The findings are discussed as they relate to membrane processing, and also from the standpoint of enhancing our fundamental understanding of the underlying phenomena.

First, the effect of shear on polymeric dope solutions was investigated. Shear-induced demixing—a phenomenon not previously studied in membrane materials—was found to occur in membrane dopes. Phase separation experiments also showed that shear-induced demixing promotes macrovoid formation. The demixing process was found to depend not only on the instantaneous shear conditions, but also on the shear history of the solution. This suggests that low-shear flow processes that occur in the upstream tubing and channels used for fiber spinning can affect macrovoid formation.

The effect of viscoelastic media on dispersed particles was also explored. Shear-small-angle light scattering results showed that particles suspended in membrane dope solutions formed aggregated, vorticity-oriented structures when shear rates in the shear-thinning regime of the polymer solution were applied. Shear rates well below the shear-thinning regime did not produce any structure. In fact, the application of a Newtonian

shear rate to a sample already containing the vorticity structure caused the sample to return to isotropy. Measurements using a highly elastic, constant-viscosity Boger fluid showed that strong normal forces alone are not sufficient to form the vorticity structures, but that shear thinning is also required.

Lastly, a study was conducted examining cross-stream migration of particles dispersed in viscoelastic media. Fluids exhibiting varying degrees of shear thinning and normal forces were found to have different effects on the particle distribution along the shear gradient axis in Poiseuille flow. Shear thinning was found to promote migration toward the channel center, while normal stresses tended to cause migration toward the channel walls.

In addition to hollow fiber spinning, many other industrially relevant applications involve polymer solutions and suspensions of particles in viscoelastic media. Often, the properties and performance of the material depend strongly on the internal microstructure. The results from the research described in this thesis can be used to guide the design of materials and processing conditions, so that the desired microstructural characteristics can be achieved.

CHAPTER 1

INTRODUCTION

1.1 Rheology & Hollow Fiber Membrane Spinning

Asymmetric hollow fiber membranes offer a promising alternative to traditional, energy-intensive thermal separation techniques (e.g., distillation) for purifying gas mixtures in the chemical industry. Compared to other types of membranes, hollow fibers offer several particularly attractive features. Their durability and geometry allow them to withstand large transmembrane pressure drops. Also, hollow fibers are generally made from polymeric materials, which are relatively inexpensive and easy to process, compared to the inorganic materials that are sometimes used to produce membranes. Perhaps their most important characteristic, however, is that they provide extremely large surface areas per unit volume, allowing them to handle large gas flow capacities with a small equipment footprint [1-3].

In recent decades, significant improvements have been made to hollow fiber technology, but there are still some obstacles to widespread implementation. Developing advanced materials and improving the versatility of fiber fabrication methods have been identified as two of the most critical challenges [3, 4]. Each of these challenges has an important rheological component. The materials being developed for next-generation hollow fibers include highly engineered polymers and composite materials, both of which possess extremely non-Newtonian characteristics that affect processing. Fiber fabrication (i.e., fiber spinning) involves complex flow conditions that can greatly affect the microstructure of the aforementioned materials, and hence the properties of the final

product. The aim of this thesis is to identify ways to improve hollow fiber technology by bridging the fields of rheology and membrane research. The remainder of this chapter will provide a description of the fiber spinning process and the rheological complexities involved, followed by a discussion of the shear-related phenomena that are explored in this thesis and a list of specific aims.

1.1.1 Hollow Fiber Spinning

Polymeric hollow fiber membranes are prepared through a spinning process (shown in Figure 1.1) in which a concentrated polymeric solution (the "dope") is extruded through the annular channel of a spinneret, with a bore fluid co-extruded in the center to generate the hollow core of the fiber. The extruded filament enters into a quench bath where it is thermodynamically phase separated, undergoing a liquid-to-solid transition by extracting solvent from the fiber. Prior to entering the quench bath, the filament is sometimes first passed through an air gap (so-called dry-jet wet spinning), where partial solvent evaporation takes place. This evaporation aids in the formation of a thin skin layer that provides selectivity without hindering mass transfer [5-7]. After solidification, the fiber is finally wound onto an uptake drum. The take-up speed of the solidified fiber is typically greater than the velocity at which the filament exits the spinneret, which results in strong extensional flow of the liquid in the air gap. The ratio between spinning velocity and take-up velocity is referred to as the draw ratio. During post-processing, which is not the focus of this thesis, the fibers are ultimately cut into segments that are bundled to form a membrane module.

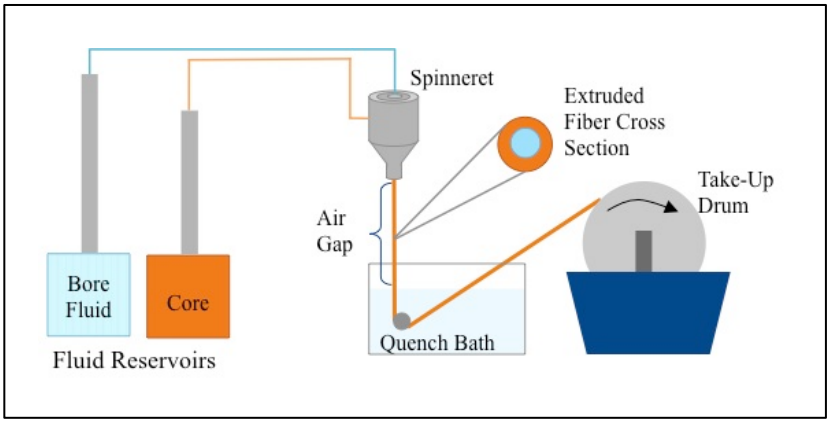

Figure 1.1 Schematic diagram of the polymeric hollow fiber spinning process.

The process described above for purely polymeric fibers already contains many rheological complexities. For example, the polymeric dope solutions are generally prepared at high concentrations, in the entangled regime, which is characterized by strong viscoelasticity and shear thinning [8]. Furthermore, some of the most promising new hollow fiber membrane designs, known as mixed matrix membranes, incorporate molecular sieve particles into a polymer matrix [9-15]. Because these particulate materials tend to be expensive and because they only contribute significantly to membrane functionality when located in the outer layer of the fiber, dual-layer spinning processes have been developed. In this approach, a second layer of membrane dope containing the molecular sieves (the 'sheath' layer) is extruded on the outside of a purely polymeric core, as shown in Figure 1.2.

Molecular sieves are materials with extremely well defined pore sizes, such as zeolites or molecular organic framework (MOF) particles. As their name indicates, these materials offer great size specificity for molecular separations. The addition of these particulates to an already non-Newtonian material further exacerbates the rheological difficulties associated with fiber spinning. Adding particles to a fluid can affect the

overall rheology of the suspension, for example by enhancing its shear-thinning properties, introducing transient stress effects, and causing the formation of anisotropic structures during shear [16-19].

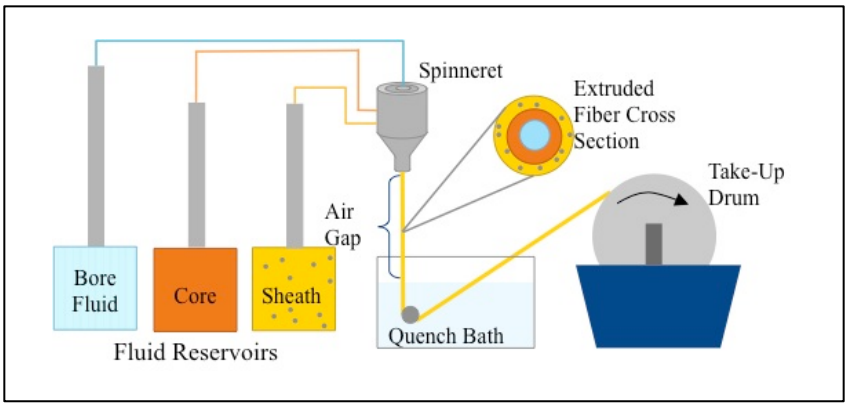

Figure 1.2 Schematic of a dual-layer, mixed matrix fiber spinning operation.

There are several compelling reasons to better understand the role of rheology in hollow fiber spinning. On a very basic level, rheology is important in spinning because the viscosity of the dope determines whether it is 'spinnable' or not. The dope must not be so viscous as to prevent it from being pumped through the narrow spinneret at fairly high rates, but its viscosity should also not be so low that the liquid filament easily breaks apart in the air gap or the quench bath. In addition to quantifying shear viscosity, which is often identified as a key spinning parameter, rheological measurements can provide much more information. They can help to detect, diagnose, and understand any underlying flow-induced structural transitions that may occur within a fluid, allowing us to connect microscopic features to the bulk flow properties of a material. This latter aspect of rheological studies is particularly relevant for fiber spinning, because fibers must possess

the correct micromorphology in order to be suitable for separation applications. These considerations will be discussed further in the following section.

1.1.2 Fiber Microstructure

Hollow fiber membranes typically have an external diameter of 200-300 μm, with a fiber wall thickness of roughly 50-100 μm. These fibers should have several microstructural characteristics. First of all, they should be asymmetric in the sense that the fiber wall should be composed of two regions with different morphologies. The inner portion of the fiber, which provides the mechanical support, should have an open, porous structure to minimize mass transfer resistance. The outer portion of the fiber should possess a thin, dense skin layer, that provides a high selectivity for molecular separations [20]. This asymmetric morphology is illustrated in Figure 1.3 and applies to both purely polymeric and mixed matrix membrane fibers.

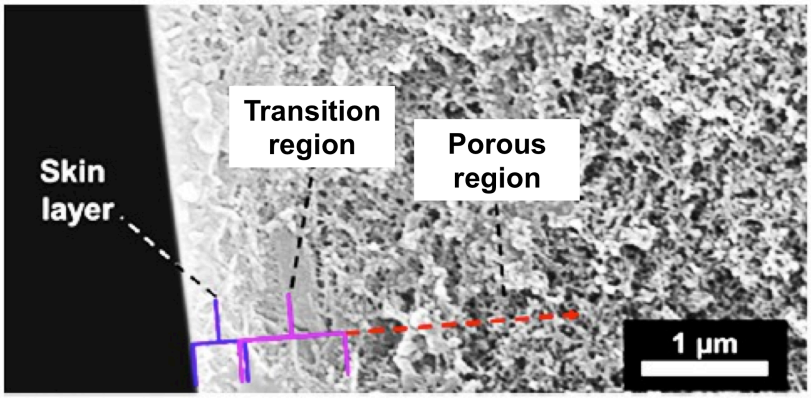

Figure 1.3 SEM micrograph illustrating the asymmetric nature of a hollow fiber membrane, from [20].

Another important challenge is the need to eliminate fiber defects. The most commonly observed defects are the teardrop shaped voids shown in Figure 1.4. These defects are often called macrovoids, and they pose several problems. First, macrovoids compromise the mechanical integrity of a fiber, limiting the pressure drops that can be imposed on the membrane unit [21]. Secondly, if these voids penetrate the selective skin layer, they become leak sources that undermine the selectivity of the entire fiber.

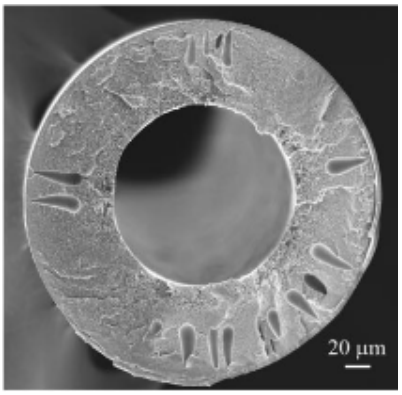

Figure 1.4 Hollow fiber containing many macrovoids, from [22].

It is well documented that macrovoids in mixed matrix fibers often originate at the location of a molecular sieve, indicating that the presence of particles promotes macrovoid formation. It has been reported that these particle-initiated macrovoids can be suppressed by the use of a large draw ratio and/or smaller sieve particles [22]. Strong elongational flow has also been found to suppress macrovoid formation in particle-free fibers [23]. However, the mechanism responsible for this effect is not fully understood, and the elimination of defects remains an important challenge during membrane spinning. For mixed matrix fibers, there are additional desired characteristics regarding the dispersed particulate phase. First, particles must remain well dispersed throughout the

process, since agglomerated particles are more likely to cause defects in the surrounding matrix. Also, the distribution of particles along the radial direction is important. To maximize the beneficial effects from the added sieves, one would like to have as large a concentration as possible in the skin layer, provided that the presence of the sieves does not cause unwanted defects in the polymer matrix. Sieve particles that are located outside the skin layer, i.e. embedded in the porous support, do not enhance the selectivity of the fiber and are effectively useless. It is important to note that the skin layer can be as thin as tens of nanometers, while the total thickness of the sheath layer containing the particles can be tens of microns. As will be discussed later, non-Newtonian effects can cause unexpected changes in particle distribution under flow, which could potentially result in a non-uniform distribution of particles within the sheath layer. As a result, one cannot simply assume that the skin layer sieve concentration will be the same as the overall concentration of the sheath dope. The efficient use of sieve particles is of significant economical concern, because they tend to be the most expensive component of a mixed matrix membrane.

With these considerations in mind, the overarching objective of this thesis is to investigate the effect of shear on the microstructure of dope solutions, both with and without dispersed particles. Three particular shear-related phenomena were identified as being of interest based on several criteria. Each involves shear-induced effects that could potentially affect fiber performance, either negatively or positively. Also, prior rheology literature indicates that these phenomena occur in materials that are rheologically similar to the dope solutions used to spin hollow fibers, making them potentially relevant for

fiber spinning. Finally, none of these effects have been explored extensively, if at all, in terms of membrane materials. The three topics to be explored are

- Shear history and shear-induced demixing in polymer solutions
- Shear-induced aggregation and alignment of particles dispersed in polymer solutions
- Shear-induced particle migration in polymer solutions

The following sections will briefly introduce each of these topics and provide the motivation for studying their particular effects in membrane spinning. They also contain reviews of the prior work that has been reported in these areas, both in the rheology literature and by the membrane research community.

1.2 Polymer Effects: Shear History & Shear-Induced Demixing

The first topic to be addressed involves the effect of shear on polymeric dope solutions. Although this portion of the research will focus on dope solutions without particles, the same effects apply to the polymeric portion of a mixed matrix dope. The purpose of this section is to discuss how two effects—shear history and shear-induced demixing—could affect defect formation in hollow fiber spinning.

1.2.1 Considering Shear History

Many studies in the past have attempted to correlate fiber-spinning conditions with separation performance of the final membrane. For example, researchers have investigated the effect of elongation [22-24], quench bath conditions [25-28], and dope composition [27-32]. While there have also been some studies investigating the effect of

shear rate during spinning, these have been less conclusive [33-36]. In one of these studies, for example, Chung et al. observed variations in separation performance with changes in shear conditions, but the resulting fibers contained many defects, even for the best performing fibers, which made the results difficult to interpret [35].

One reason that these studies may have failed to produce major insights into the effect of shear is that they were focused on the instantaneous shear conditions at the narrow spinneret exit. At first sight, this is not an unreasonable choice, since shear at the exit represents the highest shear rate (smallest channel) present in the process, and because it represents the final shear step before the dope enters the air gap, where shear is replaced by extensional flow and phase separation is initiated.

There are, however, compelling reasons to also consider the effect of shear during other phases of the spinning process. First, even if a useful correlation can be made between shear at the spinneret exit and membrane separation performance, this is not necessarily a convenient parameter to adjust. In order to change the shear rate at the spinneret exit, one would either have to change the spinneret geometry, which is expensive, or the dope flow rate, which could lead to undesirable changes in the fiber dimensions due to die swell effects. Another reason to consider shear in other phases of the process is that the total strain (i.e., the total amount of deformation) associated with this final high-shear step only represents a small fraction of the total deformation experienced by the dope solution during spinning. Upstream channels, tubing, and piping comprise much of the total strain applied to the dope solution. The strain within the final spinneret channel scales as L/h, where L is the channel length and h the gap size; for a typical spinneret, L/h is on the order of 10. By comparison, if ¼” diameter tubing is used

upstream of the spinneret, as little as 2.5 inches of this tubing would provide enough strain to exceed the total deformation within the final spinneret channel.

Shear history is particularly important when considering scale-up from laboratory spinning to larger industrial settings. The actual spinneret dimensions would likely not change significantly in the scale-up process, since the desired size of the fibers does not change. However, upstream tubing, etc. is often considered unimportant, and therefore might be altered with little consideration if, for example, some particular tubing size happened to be cheaper or more readily available than the size that was used in the original design. Fiber spinning professionals in industry sometimes report puzzling differences in fiber quality at separate production sites that utilize seemingly identical spinning conditions [37], suggesting that we should reevaluate conventional wisdom about the relevance of various phases of the process with regards to fiber quality. Therefore, a more comprehensive understanding of shear conditions could help to improve the overall versatility and reliability of the spinning process by providing universal guidelines that are not specific for a certain dope formulation (e.g., polymer/solvent combination and concentration).

1.2.2 Shear-Induced Demixing

Another shear-related issue that has thus far gone largely unexplored in the membrane field is shear-induced demixing. Shear-induced demixing (also referred to as shear-induced phase separation, or shear-enhanced concentration fluctuations, depending on the extent of the behavior) is a phenomenon that has been of interest in the polymer research community for many decades [38-45]. One of the earliest accounts came from Ver Strate

and Philippoff, who discovered that a polymer solution flowing through the converging section of a contraction channel like the one shown in Figure 1.5 exhibited visible turbidity in the regions of high shear rate [45]. This turbidity was caused by the presence of a separate phase that formed in the solution as a result of the higher shear rate in the narrower section of the channel.

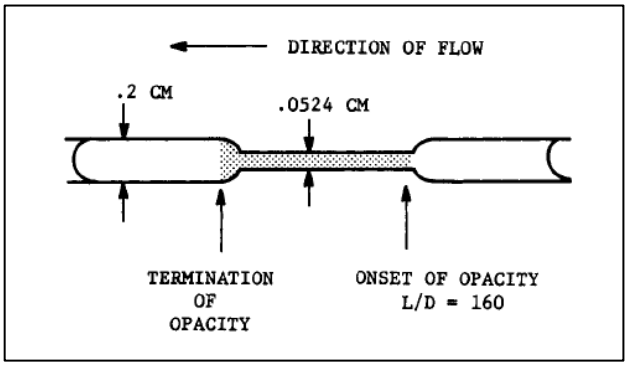

Figure 1.5 Diagram showing the flow geometry and appearance of opacity in the experiments of Ver Strate and Philippoff [45].

The study by Ver Strate and Philipoff included solutions of polystyrene (4.3 vol.%, M_w 1.8x10^6 and 2x10^6 g/mol) in either dioctyl phthalate or decalin. Interestingly, the turbidity seemed to disappear shortly after the solution left the narrow section of the channel, suggesting that the phase separation was reversed once the shear rate was reduced.

Since this work, a large body of research has developed on shear-induced demixing. While the mechanism is still not entirely understood, the most generally accepted theory is that it occurs due to a large disparity in molecular dynamics among the components of a mixture [38, 46-48]. It occurs most commonly in polymer solutions, which consist of long, slow polymer chains and small, fast-diffusing solvent molecules. In such solutions,

random, thermally induced concentration fluctuations (which are necessarily present in any multi-component system) result in localized regions that are slightly enriched in polymer entanglements, and therefore have a higher viscosity, and lower-viscosity regions with slightly higher solvent concentrations. The application of deformation then causes an unequal distribution of stress among these regions. Domains rich in polymer entanglements bear a larger fraction of the stress, and tend to squeeze solvent into nearby low-viscosity, solvent-rich regions. As a result, the concentration fluctuations become amplified, often to the point of visible phase separation.

Ten years after the previously mentioned study, Rangel-Nafaile et al. published a paper in which they reviewed the various findings on shear-induced demixing [49]. To illustrate how puzzling and diverse this phenomenon can be, a table from their paper that summarizes some key observations from past research is reproduced in Table 1.1. As this list shows, the shear rates required to induce demixing can vary over many orders of magnitude. In fact, the use of more sensitive techniques like light scattering has since allowed researchers to observe enhancements of concentration fluctuations at shear rates even lower than the ones reported in this table (sometimes as low as 10^{-2} s^{-1}) [48, 50-53]. While most studies have involved high molecular weight polymers (10^6 g/mol or more), the effect has also been observed for polymers of lower molecular weight, on the order of 10^5 g/mol [39]. Another interesting observation from the data review in Table 1.1 is the fact that the shear-induced demixing is sometimes reversible, while in other cases it is found to be irreversible.

Table 1.1 A table reproduced from Rangel-Nafaile et al. summarizing many of the early observations of shear-induced demixing [49].

Table I
Compilation of Literature Data on Stress-Induced Phase Separations in Polymeric Solutions and Melts

polymer–solvent system	crit shear rate, s^{-1}	system used to produce the phenomenon	comments	ref
poly(methacrylic acid) in distilled water	10		irreversible effect	Eliassaf et al.[8]
poly(methyl methacrylate) in dimethyl phthalate	approx 20	cone and plate	small gellike particles	Lodge[9]
polystyrene in dimethyl phthalate	approx 20	cone and plate	small gellike particles	Lodge[9]
muscle proteins in distilled water	100 Hz	oscillatory plate	viscosity changes	Ohnishi[10]
poly(vinyl alcohol) in water	approx 200		irreversible formation of associates	Peter and Noetzel[11]
aqueous solutions of tobacco mosaic virus	approx 14 400	concentric cylinders	irreversible phenomenon	Joly[1]
aqueous solutions of serum albumin	290	concentric cylinders	reversible effect	Joly[1]
poly(methyl methacrylate) in Aroclor	20	cone and plate	reversible phenomenon	Peterlin and Turner[12]
poly(methyl methacrylate) in Aroclor	20	cone and plate	irreversible for large deformations	Peterlin et al.[13]
poly(methyl methacrylate) in Aroclor	20	cone and plate	reversible phenomenon	Peterlin et al.[14]
polyesters and epoxy compounds in toluene and ethylbenzene		concentric cylinders	quasi-crystallites and rheological networks	Steg and Katz[15]
polyethylene in xylene	150 rpm	concentric cylinders, stirrers	irreversibly precipitated	Pennings and Kiel[2]
polyacrylamide Separan AP-30 in distilled water	approx 200	inflow expt	reversible haze	Metzner et al.[6]
polyacrylamide in water		inflow expt	reversible haze	Giesekus[7]
poly(methyl methacrylate) in Aroclor	20	cone and plate	reversible aggregates	Matsuo et al.[16]
polystyrene in Aroclor	approx 150	concentric cylinders	reversible formation	Munk and Peterlin[18]
polystyrene in cyclohexanone	up to 400	concentric cylinders	irreversible	Deveaubois et al.[17]
isotactic polypropylene melt		converging flow	enhanced orientation and melting points	Sieglaff and O'Leary[21]
high-density polyethylene in xylene or diphenyl ether	2000 or more	extensional flow	crystallization	Frank et al.[20]
poly(vinyl alcohol) in distilled water		concentric cylinders	irreversibly precipitated	Yamaura et al.[22]
poly(ethylene oxide) in Aroclor	approx 100	cone and plate	strong time dependence irreversible effect	Laufer et al.[23]
high-density polyethylene melt	50	extensional flow	also observed probable crystallization on flow through screens at 140 °C	Mackley and Keller[24]
polystyrene in DOP	approx 100	capillary and concentric cylinders	reversible phenomenon	Ver Strate and Philippoff[25]
polystyrene in decalin	approx 100	capillary and concentric cylinders	reversible phenomenon	Ver Strate and Philippoff[25]
poly(ethylene oxide) melt		concentric cylinders	obsd an increase in nucleation rate with shearing	Fritsche and Price[26]
polyisobutylene in oil	5	cone and plate		Michele[27]
polyacrylamide dissolved in water–glycerin mixture	order of 10 s^{-1} (exten)	ductless siphon		Kanel[19]
polystyrene in *tert*-butyl acetate		concentric cylinders	reversible	Wolf[28]
polycapramide–caprolactam	1–500	concentric cylinders	reversible and irreversible phenomenon	Malkin et al.[29]

Surprisingly, shear-induced demixing has never been investigated for membrane materials, even though some researchers have speculated that it could play a role in the fiber spinning process. Husain and Koros, for example, suggest that shear-induced demixing could help to suppress macrovoid formation by accelerating the phase separation that occurs in the quench bath [22].

The first aim of this thesis is to determine the effect of shear conditions that occur during spinning on the polymeric dope solutions that are typically used to produce hollow fiber membranes. Specific questions to be addressed are: Does shear-induced demixing occur in membrane dopes? If so, does it depend only on the instantaneous shear conditions, or is shear history important? Finally, what effect does shear-induced demixing have on macrovoid formation? The details and findings regarding these questions will be discussed in Chapter 2.

1.3 Particle Effects: Shear-Induced Aggregation & Orientation

The remaining topics to be discussed relate to polymeric fibers containing molecular sieves. As mentioned before, mixed matrix spinning possesses an additional layer of rheological complexity due to the presence of dispersed particles. Not only do they further complicate the rheological properties of an already non-Newtonian dope, but they can also cause specific problems such as promoting defects in the surrounding polymer matrix, including macrovoids and "sieve-in-a-cage" defects in which the polymer matrix does not properly adhere to the particle surface [22]. Additionally, suspensions of particles in polymeric media can exhibit transient viscosity effects that could create difficulties in maintaining the stability of the liquid filament in the air gap [17, 18, 54-56]. For some fibers containing large loadings of particles, especially if they are geometrically anisotropic, jamming and shear-thickening effects can become problematic. The second objective of this thesis is therefore to gain a better understanding of the effect of shear conditions during processing on the microstructure of a composite dope and the properties of the resulting fiber after phase separation.

The rheology literature offers an abundance of examples of shear-induced structure in suspensions of particles in viscoelastic media [57-62]. In many cases, experimental observations have been reported without a full mechanistic understanding. Studying shear-induced microstructure in composite membrane dope materials therefore provides a two-fold benefit. First, we can gain an understanding of the types of behavior that may occur during spinning, thereby improving the versatility of composite fiber technology. Additionally, a meaningful contribution can be made to the growing body of rheology research on the topic by answering some fundamental questions about the underlying phenomena.

Work in the area of shear-induced suspension microstructure began with a seminal publication by Michele et al. in 1977 [19]. In this work, monolayers of non-colloidal (60-70 μm) glass beads in various viscoelastic polymer solutions were found to form long strings that oriented along the flow direction (see Figure 1.6). The authors also noted that the formation of this structure seemed to require a Weissenberg number (the dimensionless ratio of N_1, the first normal stress difference, to shear stress) exceeding a value of 10.

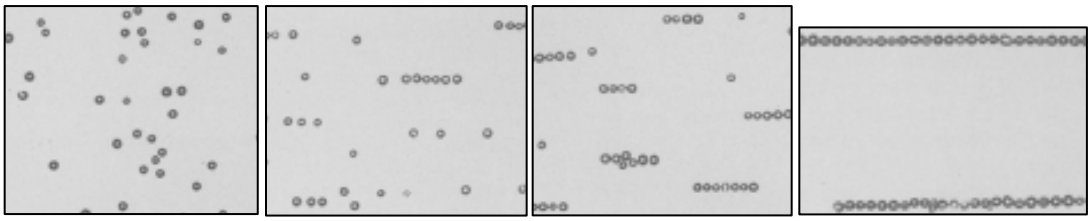

Figure 1.6 Progression of flow-oriented string formation observed by Michele et al.; the suspension consisted of 60-70 μm glass spheres in an aqueous polyacrylamide solution (0.5%) [19].

This behavior is potentially relevant for fiber spinning in a few ways. As mentioned earlier, particle aggregation is undesirable in fiber spinning due to the fact that aggregated particles are more likely to initiate defects in the surrounding polymer. We are not currently aware of any reports indicating that structures like those in Figure 1.6 have been observed in hollow fiber spinning. However, spun fibers are usually examined primarily through electron microscopy of cross-sectional cuts, which would likely not reveal such features; flow-oriented strings would be oriented along the axial direction of a hollow fiber, perpendicular to the plane of view of the microscope.

The effect of shear on the orientation of particles is also significant, since geometrically anisotropic sieves are sometimes used [63-66]. The potential benefit of high aspect ratio sieves is that they can create a more tortuous path for excluded molecules when they are oriented perpendicular to the permeation direction in a fiber, as illustrated in Figure 1.7, thus enhancing selectivity of the separation. Achieving this benefit, however, relies on alignment of the sieves, so it is beneficial to develop an understanding of the potential orientation effects that can occur in viscoelastic media.

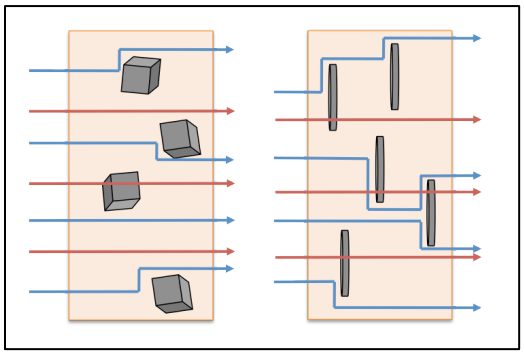

Figure 1.7 Diagram illustrating the selectivity benefits of large aspect ratio molecular sieves that are aligned perpendicular to the gas transport direction.

The next sections will review the findings on shear-induced structure from the rheology community. Flow-oriented structures similar to those observed by Michele et al. will be discussed first, followed by a less common type of structure that has since been observed: vorticity-oriented structures.

1.3.1 Flow-Oriented Structure

Understanding flow-oriented, string-like structures remains an important topic in rheology research, and many questions remain unanswered. For example, it is still unclear whether this is primarily a surface effect, or if alignment also occurs in the bulk. The requirements for the formation of such structures are also still subject of debate. Specifically, researchers would like to know whether it is sufficient to have a continuous phase that is elastic, or if shear thinning is also required in order to generate string formation.

A recent study by Scirocco et al. involved polystyrene particles (2.7 μm) in fluids with varying degrees of elasticity and shear thinning [67]. They found particle chaining at Weissenberg number values ranging from 0.5 to 16.5, which was in contradiction with earlier reports claiming that structure formation required a minimum ratio of 10 [19, 59]. The study by Scirocco showed that chain formation occurred in the bulk of the sample, and did not depend on the size of the gap between the shearing surfaces. Another interesting finding from this paper is that particles suspended in a Boger fluid (a highly elastic, non-shear-thinning fluid that is a useful rheological model system for isolating the effects of elasticity) did not exhibit any structure formation, even at much larger

Weissenberg numbers; this result indicates that shear thinning is also a requirement for string formation. These results are illustrated in Figure 1.8.

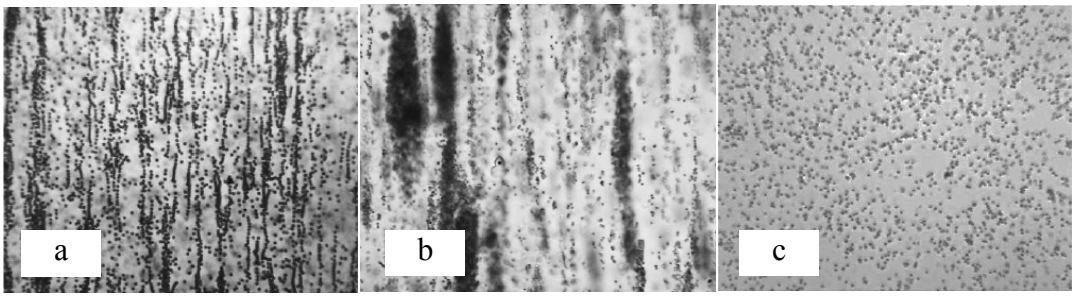

Figure 1.8 Various microstructures observed by Scirocco et al.: (a) flow-oriented strings in a shear-thinning solution; (b) flow-oriented bundles in a solution with a Weissenberg ratio much greater than (a); (c) homogeneous distribution of particles in a Boger fluid [67].

However, in a subsequent study from the same group, surface effects were found to be of importance [68]: all particles (sizes ranging from 1-3 μm) were found to form flow-oriented strings at sufficiently high shear rates, but only at the shearing surfaces and *not* in the bulk. Interestingly, for the smallest particles in the study, shear rates *below* the onset of shear thinning were found to result in short, vorticity-oriented clusters, a phenomenon that will be discussed in more detail in Section 1.3.2.

Although the previously mentioned study by Scirocco et al. did not find any string formation in suspensions of particles in a Boger fluid, some researchers have observed shear-induced structure in these purely elastic fluids. Won and Kim studied large particles (diameter ~300 μm) in various fluids using a reciprocating shear apparatus and found that at large shear rates, particles in a Boger fluid formed a distinctive zigzag pattern of non-contacting particles with very regular interparticle spacing (see Figure 1.9) [69]. Their findings regarding string formation in shear-thinning fluids were in agreement

with the Scirocco study; like Scirocco et al., Won and Kim also observed long, straight strings in these fluids. Yet the contradictory results for the Boger fluid case provide another example of how puzzling this behavior can be, and suggest that the underlying mechanisms are more complex than originally thought.

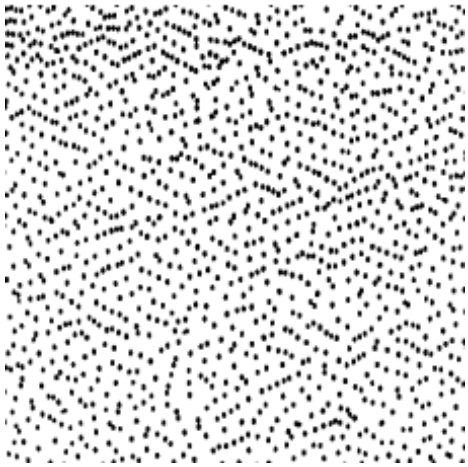

Figure 1.9 Structure observed by Won and Kim for non-colloidal particles in a Boger fluid under reciprocating shear [69].

In addition to experimental investigations, researchers have attempted to understand particle chaining through simulations. Recently, simulations using the responsive particle dynamics method (RaPiD) have successfully reproduced experimental results of particle string formation [70, 71]. RaPiD uses Brownian particles with varying interparticle degrees of freedom to simulate entanglements [70]. Using this technique, Santos de Oliveira et al. investigated particle chaining in shear-thinning fluids, including solutions of polymers and wormlike micelles (Figure 1.10). Their study showed that shear alters the distribution of polymer molecules around the dispersed particles, causing polymer-lean wakes downstream of the particles, and polymer accumulation on the upstream side. When particles approach each other, the wakes create a strongly depleted region between

the particles, resulting in a net attraction. Their results also show that for a given polymer system, a critical viscosity exists, below which particle strings are observed; above the critical viscosity, strings do not occur [71]. This could explain the lack of structure formation that is sometimes observed in Boger fluids. It is possible that shear-induced strings do not form in Boger fluids because their shear rate-independent viscosity is above the critical value for string formation.

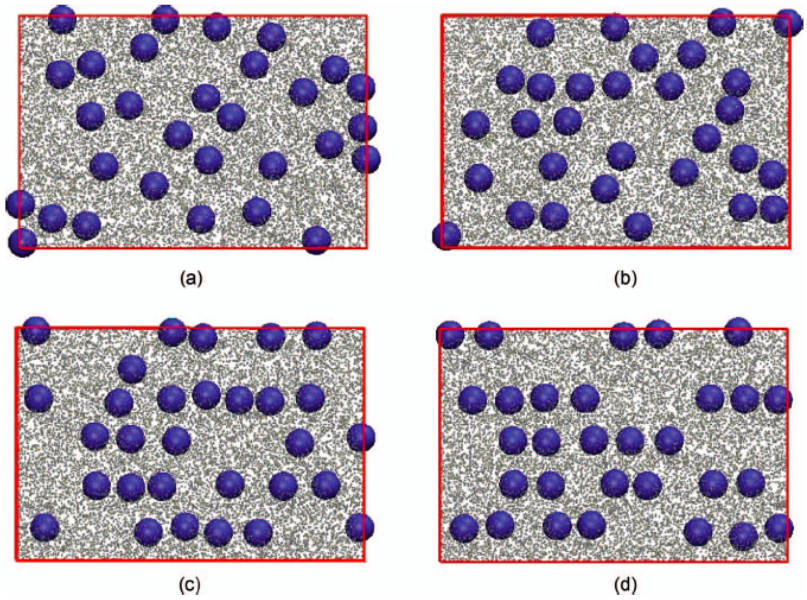

Figure 1.10 Simulation results from Santos de Oliveira et al. showing the development of strings of particles suspended in a wormlike micelle solution [70].

1.3.2 Vorticity-Oriented Structure

While the mechanism that leads to shear-induced aggregation of particles is still somewhat puzzling, the tendency of these aggregates to orient themselves along the flow direction is at least somewhat intuitive. An arguably more intriguing phenomenon is vorticity-oriented structure formation, in which alignment occurs along the vorticity, or neutral axis, of the shear field, as shown in Figure 1.11.

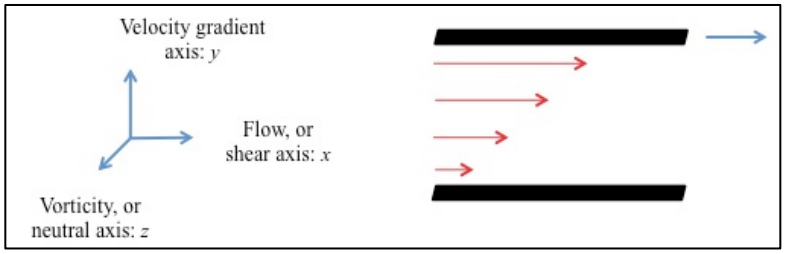

Figure 1.11 Definition of flow, gradient, and vorticity axes in simple shear flow.

One of the early observations of vorticity-oriented aggregates was reported by DeGroot et al. [72]. In this paper, the authors studied suspensions of colloidal silica (50 nm) in a polymer melt (polydimethylsiloxane, or PDMS). Shear caused the particles to flocculate and orient along the vorticity axis, as shown in Figure 1.12. They hypothesized that the flocculation was due to polymer bridging, but the orientation along the vorticity axis was not fully explained.

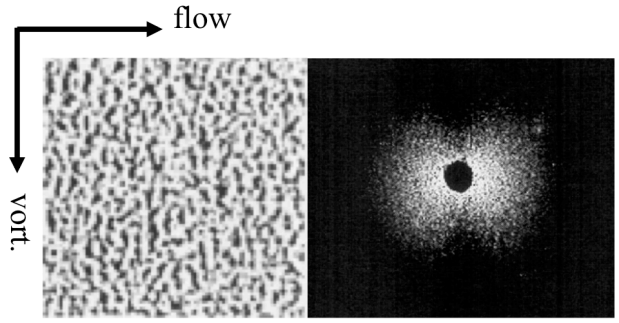

Figure 1.12 Optical image (left) and characteristic butterfly scattering pattern illustrating the aggregated, vorticity-oriented structure formed due to shear [72].

One interesting feature of the structure in this system is the fact that the vorticity orientation and the anisotropy of the resulting light scattering pattern both disappeared within seconds after shear was stopped. Despite the fact that the particles are fairly small,

the authors pointed out that this rapid restoration of isotropy cannot be attributed to Brownian diffusion because of the high viscosity of the suspending polymer melt. Instead, they postulated that the disappearance of the structure is due to stored elasticity within the aggregates. They suggest that the aggregates contract and form rolling cylindrical structures during flow, and then are able to relax by releasing this stored energy upon cessation of shear flow.

Another instance of vorticity-oriented structure was mentioned briefly in Section 1.3.1. This observation was made by Pasquino et al. [68] during a study that was focused primarily on flow-oriented string formation. In their experiments, these authors found that the smallest particles, at the lowest shear rates explored (which were below the onset of shear thinning in the polymer solution used as the suspending fluid) tended to form short clusters of 2-4 particles that became oriented in the vorticity direction.

Since one of the defining features of polymeric materials is their ability to exert stresses normal to flow, one might initially think that vorticity-oriented aggregates are caused by localized, microscopic manifestations of these normal stresses. However, in the experiments by Pasquino, vorticity orientation was observed at shear rates that were well within the Newtonian regime of the solution. Under these conditions, polymer chains are not significantly stretched, so that normal forces should be negligible. In fact, at the shear rate that resulted in vorticity orientation, the suspending fluid exhibited a Weissenberg ratio of ~0.5, which strongly suggests that shear forces should dominate over normal stresses. The fact that a vorticity orientation is observed under these conditions is quite surprising.

Based on the multitude of experimental observations briefly reviewed above, there is no clear prediction of the types of shear-induced microstructure that might occur during composite fiber spinning. By studying suspensions of particles in membrane dopes, we can first identify the structures that can form in these materials, and use this information to provide guidance to the design of fiber spinning processes. However, there are also many other applications involving particles dispersed in non-Newtonian media that would benefit from an enhanced understanding of these phenomena [73-75]. Therefore, this thesis will focus on understanding the mechanisms of shear-induced aggregation and orientation, so that the findings can then be used to provide future improvements to fiber spinning and other industrially relevant applications.

1.4 Particle Effects: Shear-Induced Migration

As mentioned earlier, the radial location of sieves in a mixed matrix fiber is important. The skin layer represents only a small fraction of the total sheath layer, so a non-uniform distribution of particles within the sheath layer could result in either a depletion or enrichment of sieves in the skin layer of the fiber where their presence is most desirable. A non-uniform distribution can occur if particles exhibit lateral migration during flow. Lateral migration refers to any motion of a particle that is perpendicular to the bulk flow direction.

For a neutrally buoyant, single particle in a Newtonian fluid under laminar flow conditions, lateral migration cannot occur. There are, however, several effects that are known to produce migration. One example is inertia, which causes particles in Poiseuille flow to migrate to an annular region ~0.6 radii from the center of a tube [76-84]. Since

the Reynolds number for a colloidal molecular sieve particle flowing through a spinneret is essentially zero (due to the small particle size and high fluid viscosity), this is not applicable to fiber spinning. Migration can also occur for concentrated suspensions in which particles get preferentially pushed out of the high-stress regions (e.g., near the walls of a tube) toward low-stress regions because of the more frequent interparticle interactions at high shear rates [85-89]. A third possible source of migration, and the one that is most likely to occur in hollow fiber spinning, is the presence of a non-Newtonian suspending medium.

Although there are a few examples of studies in the membrane field seeking to understand the radial distribution of sieves in composite fibers, none have attempted to investigate the effect of shear. Two studies by Chung and co-workers measured the sieve distribution in fibers spun using different air gaps and draw ratios [90, 91]. They concluded that the liquid fiber as it leaves the spinneret contains a parabolic sieve distribution (see Figure 1.13 (a2) below). That is, more sieves are located in the center of the fiber wall. This is an undesirable scenario, as explained previously. By increasing the air gap or the draw ratio, the sieve concentration in the outer portion of the fiber was increased, which is more favorable for membrane separations. However, the technique these authors used to measure the particle distribution (scanning electron microscopy with energy-dispersive X-ray spectroscopy, or SEM-EDX) produces very noisy, inconclusive profiles that are difficult to interpret. The authors also provide a rather vague, unsatisfactory explanation on why a parabolic distribution might develop ("The particles may rotate and move to the position with lower energy requirement that is located near the central part of the flow with lower shear rates."). They never truly

address the issue of shear, nor do they vary the flow rate to see how this would affect the profile. If their hypothesis and conclusions are correct, and particles are indeed migrating away from the channel walls due to shear, a rheological explanation must exist. Furthermore, migration away from the fiber wall could potentially be limited or even reversed by carefully manipulating the rheological properties of the solution, providing another approach (in addition to varying the air gap and draw ratio) to enhance the performance of mixed matrix fibers.

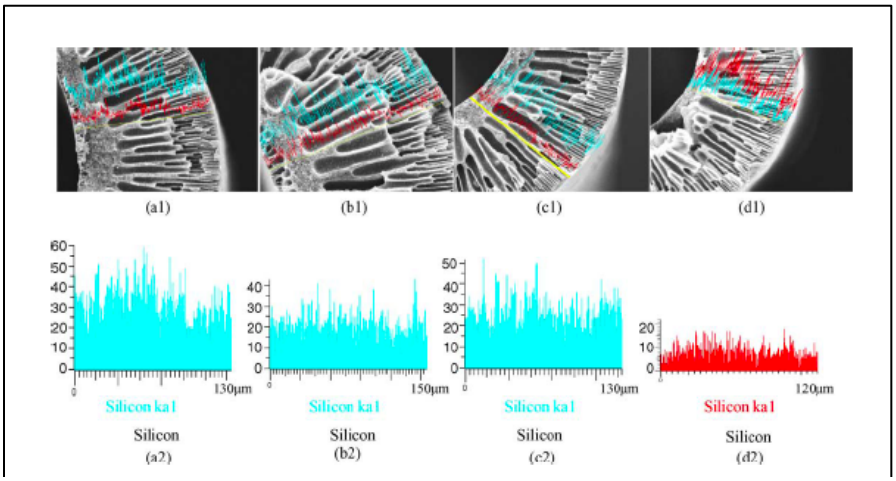

Figure 1.13 Line spectra showing the distribution of zeolites as a function of radial location in the fiber wall for four different air gaps: (a) 0 cm, (b) 1.5 cm, (c) 2.5 cm, and (d) 6 cm [90].

The rheology literature contains a plethora of experimental and theoretical research investigating particle migration induced by a non-Newtonian continuous phase [92-94]. A large portion of published research is devoted to suspensions in rheometric flow geometries, such as Couette flow, since particle migration during standard rheological measurements can produce erroneous results when trying to determine the rheological properties of these materials [95-99].

Industrial applications have also provided motivation to understand this phenomenon. One example is a study by Tehrani, who investigated particle migration in hydraulic fracturing fluids [73]. In this study, fluids that were dominantly shear thinning caused particles to migrate to the low-shear region in the center of the channel. Fluids that were predominantly elastic produced either very slight migration toward the wall, or no migration at all. These results are in apparent disagreement with an earlier study by Mason et al., who found that shear-thinning fluids caused particles to migrate toward the wall in tube flow, while an elastic fluid without strong shear thinning caused particles to migrate to the center [97].

Recently, the need for 'particle focusing' in microfluidic devices (e.g., for counting or sorting of cells and particles in biomedical applications) has sparked renewed interest in shear-induced migration. These studies typically involve particles in confined flow (i.e., particle diameters approximately one-fifth the channel height). Both experiments [100-102] and simulations [103-105] have been conducted, but the results have failed to fully clarify even the most basic aspects of this phenomenon, such as in which direction particles should migrate and what the requirements are for lateral migration.

In a recent study by D'Avino and coworkers, a bistability scenario was predicted and experimentally observed [106]. For particles flowing in a cylindrical microchannel, they found that there is some radial position, r^*, above which particles will migrate toward the wall, and below which particles will migrate toward the channel center. This finding could help explain the conflicting results observed in previous studies. The authors showed that by tuning the characteristics of the suspending fluid, the value of r^* could be manipulated. Strongly shear-thinning fluids were found to move this critical value toward

the center, thereby promoting migration to the channel walls. Less shear-thinning fluids promoted migration to the center. Based on these results, one might be surprised that composite fibers do not exhibit any evidence of migration toward the spinneret channel walls, as membrane dope solutions typically possess a substantial degree of shear thinning. One explanation is that spinnerets do not provide a sufficiently large strain for particles to complete their trajectory toward the wall.

As was the case for shear-induced aggregation and orientation effects, there is still much to be learned about viscoelasticity-induced particle migration. Not only does the rheology community desire a greater fundamental understanding of migration, but studying particle migration in dope-like materials can also help identify methods to improve composite fiber technology.

1.5 Objectives & Thesis Overview

In summary, this thesis has the following three aims:

1. **Investigate shear-induced demixing in a polymeric dope solution and determine what effect this phenomenon has on macrovoid formation.**

   These studies were carried out using shear-small-angle light scattering (shear-SALS) to monitor the phase behavior of dope solutions *in situ* under simple shear. The scattering patterns from shear-SALS were used to determine whether the solutions were in a homogeneous or demixed state, and to gain information about the features of the demixed microstructure. To understand the effect of shear history on shear-induced demixing, solutions were sheared at various rates prior to the shear-SALS experiments, and the resulting patterns were compared. Finally,

syringe extrusions were used to determine whether shear history and shear-induced demixing affect macrovoid formation in phase-separated fibers. Details regarding the experiments and results from this work are presented in Chapter 2.

2. **Investigate shear-induced aggregation and structure formation in a mixed matrix dope.**

   Suspensions of spherical silica particles in a polymer solution were used to simulate a mixed matrix membrane dope. Shear-SALS was used to measure aggregation and orientation effects within the suspension. The findings on this topic (Chapter 3) are of most interest from a rheological standpoint, but some potential implications for composite fiber spinning are also discussed later in Chapter 5.

3. **Determine the effect of viscoelasticity-induced particle migration on the radial distribution of molecular sieves in mixed matrix fibers.**

   To study lateral migration, particles were suspended in fluids with varying degrees of shear thinning and normal forces. The suspensions were then flowed through narrow rectangular glass capillaries using a wide range of flow rates. The effect of shear on particle distribution was analyzed using confocal microscopy to directly measure the particle concentration distributions within the channel. Details of this work are described in Chapter 4.

Finally, Chapter 5 provides the concluding remarks and recommendations for future work.

CHAPTER 2

SHEAR-INDUCED DEMIXING IN POLYMERIC MEMBRANE DOPES[1]

2.1 Introduction

This chapter focuses on the first aim of this thesis, which is to investigate the role of shear in macrovoid formation during hollow fiber spinning. Historically, membrane researchers have studied the effects of shear by focusing on 1) the shear conditions at the spinneret exit, and 2) the changes in molecular conformation that occur as a result of those conditions [33-35]. In this study, a different approach was taken. Rather than considering only the conditions at the spinneret exit, the following question has been explored: for a given shear process, how does the shear *history* of a solution affect its microstructure? Also, rather than focusing on changes in molecular conformation, this work explores shear-induced demixing, an effect that is known to occur in polymer solutions similar to those used for membrane spinning [39, 40, 45, 48-53].

These choices were made based on several considerations, which were discussed in Chapter 1. First, understanding the effects of shear history can potentially provide another useful process parameter to adjust in hollow fiber spinning, without having to change the dope flow rate or the spinneret dimensions; simple, inexpensive modifications to upstream tubing, for example, could improve membrane performance. Additionally, investigating shear-induced demixing in membrane dopes (rather than shear-induced chain stretching) offers a promising route to understanding the role of flow conditions on

---

[1] The contents of this chapter were previously published as: E. C. Peterson and V. Breedveld, *Shear-induced demixing in polymeric membrane dopes*, Journal of Membrane Science **431**, 131-138 (2013).

macrovoid formation, since such liquid-liquid demixing processes yield microstructural features with length scales similar to those over which macrovoids are formed.

The study described below consisted of two sets of experiments. In the first set, shear-induced demixing was investigated using shear-small-angle light scattering (shear-SALS). The experiments were designed to investigate the shear history effect using the following generalized scheme: an initial shear step was imposed on the solution, which was varied from experiment to experiment; shear-SALS was then used to monitor the microstructural response of the solution to a subsequent shear protocol (which was the same in all experiments). The initial shear step represents the possible upstream shear conditions present in spinning, and the subsequent shear process represents the flow through the final spinneret channels. Such experiments are insightful for fiber spinning, because they decouple the effects of shear prior to the spinneret and during the actual extrusion in the spinneret.

The second set of experiments was designed to investigate the role of shear history on the phase-separated micromorphology of the polymer. As in the first set of experiments, a two-step process was used: an initial shear step was applied to the solution, which was varied with each experiment; the solutions were then extruded into a quench bath under conditions that were identical in all experiments. Since hollow fiber spinning is inherently a very complex process with many adjustable parameters, it was decided that these phase separation studies would be conducted in a simpler setup (using syringe extrusions) rather than an actual spinneret. This simplified approach provides a more fundamental understanding of the complex behavior associated with membrane dopes,

and the outcomes can subsequently be used as inspiration for improvements in spinning process parameters.

The results outlined below show that shear does in fact induce demixing, at least in the dope solution that was explored. In addition, it was found that subtle variations in shear history can affect the resulting microstructure of the demixed material, which can in turn affect macrovoid formation.

2.2 Materials and Methods

2.2.1 Dope Preparation

The polymer used was Ultem® 1000 polyetherimide (SABIC Innovative Plastics, Pittsfield, MA), which is a popular polymer for hollow fiber membrane spinning due to its inherent selectivity for gas permeation [9, 10]. The solvent was n-methyl-2-pyrrolidone (NMP, 99%, Sigma Aldrich, St. Louis, MO) and the non-solvent used in this study was ethanol (anhydrous, 99%, VWR, Radnor, PA), both of which were used as received.

Solutions were prepared by combining the required amount of Ultem® powder and NMP. The mixture was then placed on a slow roller until the polymer dissolved and the solution became optically transparent. At that point, typically after 24 hours, ethanol was added so that the final concentration (by weight) was 30% Ultem®, 8% ethanol, and 62% NMP. The addition of ethanol to the concentrated polymer solution causes local phase separation in regions with high ethanol concentration. Therefore, after adding ethanol, the samples were placed back on the slow roller until the phase-separated material dissolved

and the sample was again optically transparent (typically 24 hours after the addition of ethanol). Samples were then used within 24 hours.

2.2.2 Shear History Control

In order to investigate the effect of shear history on dope microstructure, extra precautions had to be taken to ensure that samples had well defined shear histories. To achieve this, a linear actuator (Firgelli L12-S, Firgelli Technologies, Inc., Victoria BC, Canada) was used to control the syringe speed both during filling and discharging stages. A function generator (Agilent 33220A, Agilent Technologies, Santa Clara, CA) provided the voltage signals needed to control the motion of the actuator. This set-up resulted in an accessible linear speed range of 1.2-4.1 mm/s for the syringe plunger.

It should be noted that there are effectively two different wall shear rates associated with fluid flow through a syringe—one in the barrel (the main body of the syringe) and one within the narrower tip. The shear rates reported in this document represent those calculated for the syringe barrel, since that is where the majority of the total deformation occurs (for the syringes used, the total shear deformation experienced in the barrel is approximately 2.5 times the deformation in the tip). Because these polymer solutions essentially behave as Newtonian fluids in the shear rate regime explored during syringe loading, the wall shear rate can be estimated using the equation below, which gives the wall (maximum) shear rate for a Newtonian fluid in a circular tube, where Q is the volumetric flow rate, and R the radius of the tube [107]:

$$\dot{\gamma}_w = \frac{4Q}{\pi R^3} \tag{2.1}$$

The shear rate can alternatively be expressed in terms of the linear velocity of the syringe plunger, *v*:

$$\dot{\gamma}_w = \frac{4v}{R} \tag{2.2}$$

2.2.3 Shear-SALS Experiments

To probe the microstructure of the polymer solutions during shear, a small-angle light scattering (SALS) setup was installed on a stress-controlled rotational rheometer. The light scattering accessories and rheometer (MCR300) were purchased from Anton-Paar (Graz, Austria). A schematic of the setup is shown in Figure 2.1. It consists of a rotating upper plate made of quartz (diameter 43 mm) and a stationary glass lower plate. A laser beam (λ = 658 nm) passes through the plates, sample, and focusing optics before being projected onto a screen. A CCD camera (LU135M, 1392x1040 pixels, Lumenera Corporation, Ottawa, Canada) was used to collect images of the projected scattering patterns via dedicated software (Lucam Recorder, Astrofactum, Munich, Germany) with a time-lapse capture rate of 0.5 frames per second. This SALS setup can probe scattering angles between 2.5° and 12°, which corresponds to a scattering vector range of 0.4-2 μm^{-1}.

The shear rate varies across the radius of a rotating parallel plate geometry; it is zero at the center and maximum at the edge. The shear rates reported for all shear-SALS experiments in this study represent the values at the location where the laser passes through the sample, which is approximately 5 mm from the outer edge of the rotating upper plate. SALS experiments were conducted at a measuring gap of 0.6 mm. This height was chosen based on several experimental considerations, including a trade-off

between the desire to minimize the required sample volume, and the need to use a gap large enough so that pressure variations across the radius of the plate would not cause formation of vapor pockets that would interfere with scattering measurements (the pressure drop across the radius of a parallel plate measuring geometry scales as h^{-2}, where h is the measuring gap).

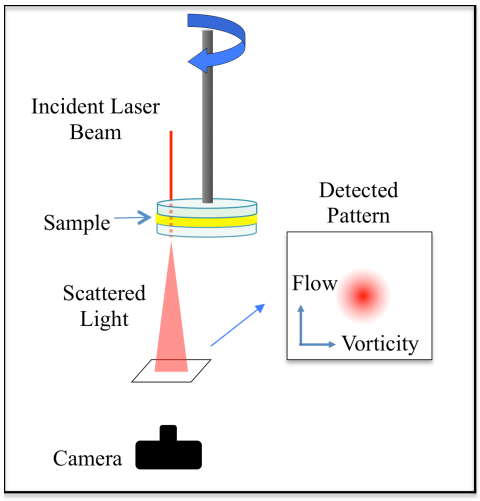

Figure 2.1 Shear-SALS setup.

The experiments conducted in this setup, referred to hereafter as step-shear experiments, were designed to investigate how the shear history of a membrane dope (for example, flow conditions in the tubing between the pumps and spinneret) might affect its microstructure as it flows through the progressively smaller channels within a spinneret. In our experiments, variations in shear history were achieved by changing the rate at which samples were syringe-loaded into the rheometer; subsequent flow through the spinneret device was mimicked through a series of intervals at increasing shear rate in the rheometer.

Specifically, these step-shear experiments were conducted as follows: the linear actuator (supplied with the necessary voltage to achieve the desired linear speed and flow rate) was used to fill a syringe (Kendall Monoject 1-ml slip-tip syringe) to the necessary volume (0.87 ml). The sample was then discharged from the syringe onto the bottom measuring plate using the same linear speed that was used for filling. The top plate was slowly lowered to the measuring position and a series of six two-minute shear intervals was applied. The shear rates used are given in Table 2.1. The scattering pattern was recorded during this entire experiment. After shear stopped, additional images were taken to analyze the resulting microstructure in its relaxed, post-shear state.

Table 2.1 Shear rate profile for step-shear experiments

Time [min]	0-2	2-4	4-6	6-8	8-10	10-12
Shear rate [s^{-1}]	0.08	0.8	4	8	16	24

2.2.4 Extrusion Experiments

In addition to the step-shear experiments, which were designed to monitor the microstructure of the liquid dope during shear, extrusion experiments were carried out with the objective of determining the effect of shear history on the micro-morphology of an extruded fiber after phase-separation in a non-solvent bath. In these experiments, shear history variations are again represented by changes in syringe loading rate. Extrusion through the spinneret is simulated here by extrusion through a needle attached to the syringe, into a non-solvent bath. The details of the extrusion experiments are as follows: first, a syringe (Kendall Monoject 1-ml Luer Lock tuberculin syringe, without needle)

was filled at a specified speed, which was varied with each experiment, as described for the step-shear experiments. After the syringe was filled, an 18G ½" needle was attached to the syringe and the solution was extruded directly into a 500 ml water bath at a fixed syringe plunger speed of 1.3 mm/s (the highest speed attainable with our actuator under these conditions, due to the large pressure drop created by the needle). The shear rate in the syringe needle at this extrusion speed is sufficiently high that a correction must be made for the non-Newtonian nature of the solution in order to calculate the wall shear rate associated with the extrusions. The corrected wall shear rate for a power law fluid through a circular tube is given by the equation below [107], where $\dot{\gamma}_{w,app.}$ is the apparent wall shear rate (calculated using Equation 2.1 above), and *n* is the power law index of the fluid, which is 0.44 for the solution used here (data not shown).

$$\dot{\gamma}_{w,corr.} = \frac{\dot{\gamma}_{w,app.}}{4}\left(3 + \frac{1}{n}\right) \tag{2.3}$$

For a needle ID of 0.838 mm and a syringe plunger speed of 1.3 mm/s, a needle wall shear rate of approximately 500 s^{-1} is obtained. It should be noted that the plunger speed of 1.3 mm/s refers to the average linear velocity of the fluid in the syringe, which corresponds to a much larger velocity in the needle. After extrusion, the fibers were left in the water bath for one hour to complete the solvent removal and solidification, and then taken out and allowed to dry.

The cross sections of each fiber were analyzed at three locations along the fiber using scanning electron microscopy (SEM). To prepare the fibers for imaging, each was soaked in hexane for approximately one minute, placed in liquid nitrogen for another minute, and then snapped quickly using tweezers so that the cross sections could be observed. Fibers were sputter-coated with a gold coating of approximately 10 nm (Q150T, Quorum

Technologies, West Sussex, UK) and imaged using SEM (JSM-6400, JEOL Ltd., Tokyo, Japan). The number of visible macrovoids was counted for each fiber. Because the entire cross section of the fiber was not visible in most cases, the number of visible macrovoids was normalized based on the visible fraction of the total fiber circumference to obtain the macrovoid count on a per-fiber basis.

2.3 Results and Discussion

First, the results of the step-shear SALS studies will be discussed. Figure 2.2 presents a summary of the scattering patterns observed during these experiments. In this matrix, the rows represent experiments at different syringe loading shear rates, while the columns represent the various shear intervals in the rheometer. Each image in this figure displays the time-averaged scattering pattern over the entire two-minute shear interval (except for the images in the last column, which were obtained at rest after completion of the experiment). With one exception (the 2.0 s^{-1} case, bottom row, which will be discussed later), the scattering patterns in the first column are nearly identical to the pattern that is observed without a sample loaded in the rheometer; the lack of scattering at 0.08 s^{-1} indicates that these samples were nearly homogeneous with undetectable concentration fluctuations. In the second interval (0.8 s^{-1}), some samples remained at a relatively low intensity, while other ones began to show large, time-dependent intensity spikes that can be attributed to localized regions of inhomogeneous, demixed material passing under the laser; in the time-averaged images depicted in this matrix, these fluctuations appear as a slight overall increase in intensity. Figure 2.3 shows the average pattern intensity vs. time for each of these experiments. During the next three intervals, the samples underwent

further demixing, as indicated by the increase in the overall pattern intensity. Since scattering patterns are a Fourier-transform representation of the real-space structure, a reciprocal relationship exists between the features observed in the scattering pattern and the actual microstructure—that is, the observed elongation of the pattern in the *vorticity* (horizontal) direction can be interpreted as an elongation of the microstructure in the *flow* direction under the influence of the applied shear. By the last interval, full shear-induced demixing had occurred and the image intensity reached a steady value in all cases. After shear was stopped, the patterns returned to an isotropic shape as the microstructure relaxed, but the high intensity remained indicating that the shear-induced demixing did not reverse itself upon cessation of flow.

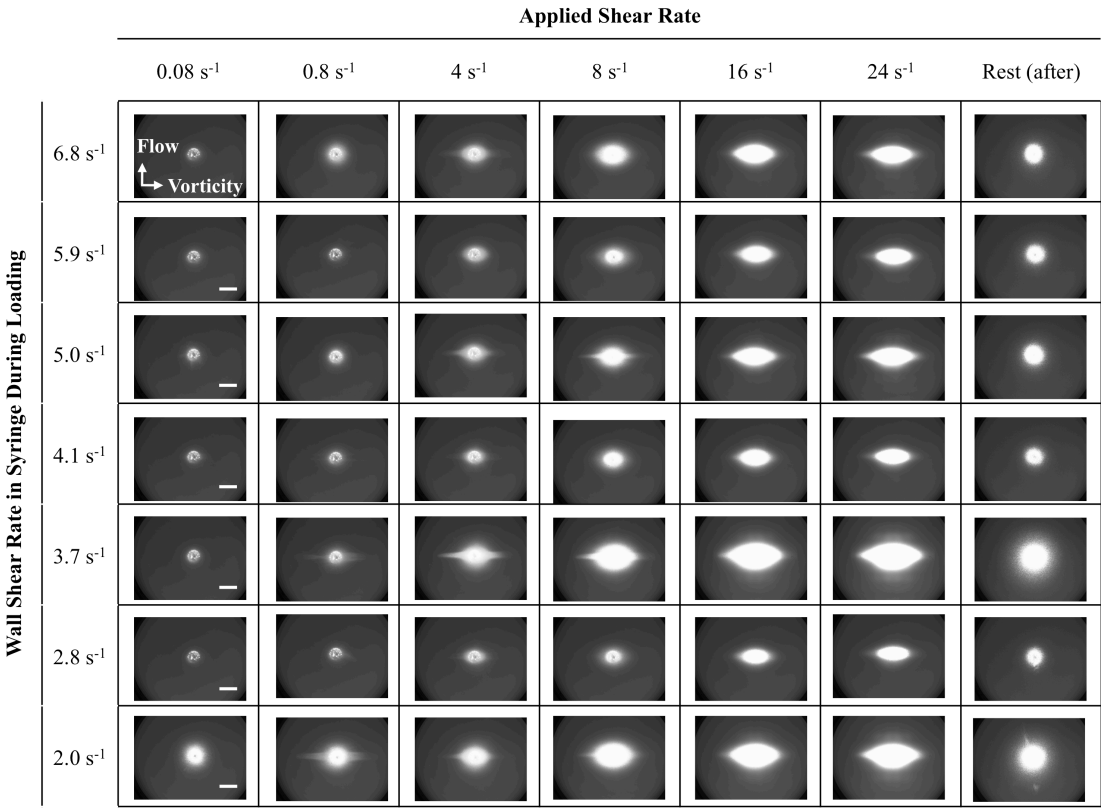

Figure 2.2 SALS patterns recorded during step-shear experiments for seven different syringe-loading rates. The first six columns are time-averaged patterns for the entire two-

minute shear interval. The last column contains images obtained after shear was stopped. The scale bar indicates a scattering vector of 1 μm^{-1}.

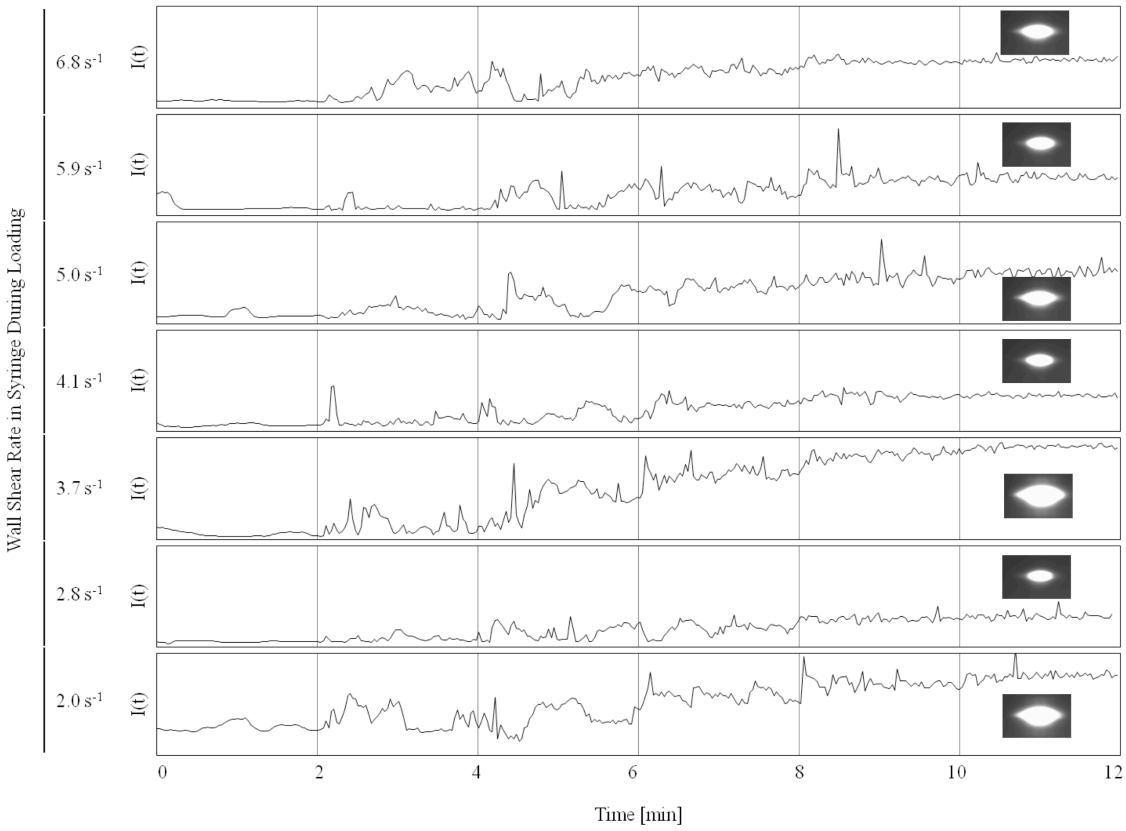

Figure 2.3 Intensity vs. time profiles for the step-shear experiments shown in Figure 2.2. For each experiment, the inset shows the average pattern for minutes 10-12.

Although shear-induced demixing was eventually observed for all the syringe loading speeds that were explored, the fact that the final pattern varied significantly depending on syringe loading rate confirms that shear history does play a role. For some syringe rates (specifically 2.0 s^{-1} and 3.7 s^{-1}), the images reached a much higher overall intensity, with the pattern extending to larger scattering angles. This suggests a phase-separated microstructure with smaller droplets. For the other five cases, the resulting pattern was noticeably smaller, indicating larger droplets. The upper data set in Figure 2.4 quantifies

this observed behavior: the average intensity of the resulting pattern after cessation of shear is plotted as a function of syringe shear rate. Alternatively, the pattern intensity during the 24 s^{-1} interval could have been plotted, since Figure 2.3 clearly shows that the demixing process had reached completion by that interval. However, interpretation of the scattering pattern is simpler without the added complication of anisotropy due to droplet stretching under shear. The intensities in Figure 2.4 are normalized by the average intensity with no sample loaded to account for slight variations in experimental settings and highlight the effect of shear history.

The hypothesis concerning the shear history dependence can be explained as follows: for some loading rates, shear within the syringe causes localized demixing, resulting in samples that are 'nucleated' with small demixed regions that act as seeds for larger, detectable demixing in subsequent shear steps. The presence of these pre-demixed regions caused widespread demixing in the subsequent shear steps to occur earlier, at lower shear rates than in other samples. Also, they resulted in a larger number of smaller microstructural features (i.e., smaller droplets that give rise to a larger scattering pattern) as demixing progressed. Conversely, samples that remained homogeneous after loading, began to demix later in the shear series, and the absence of pre-nucleated regions resulted in a coarser structure with larger phase-separated droplets. It should be noted that the term 'nucleate' is used here not in the traditional thermodynamic sense (as in phase separation via nucleation and growth vs. spinodal decomposition). Rather, it is intended to refer to the fact that some syringe speeds cause early demixing, thereby giving the bulk solution an earlier start in the subsequent shear-induced demixing process.

As mentioned near the beginning of this section, the sample loaded using a syringe shear rate of 2.0 s^{-1} differed from the others in that the pattern already had an increased intensity at the start of the step-shear experiment, which was maintained for the entire duration of the first interval (see Figure 2.3). To interpret this observation, it must be pointed out that moisture from the surrounding air can cause phase separation in Ultem®-NMP solutions. Samples loaded at a lower syringe shear rate were exposed to the air for a longer time during loading. Therefore, it is possible that in the 2.0 s^{-1} case, the slightly longer exposure to air during the loading process caused some local phase separation at the air-solution interface, which then resulted in accelerated flow-induced demixing in the step-shear experiment. However, it should be noted that this does not contradict the hypothesis that the presence of demixed regions at the beginning of a step-shear experiment results in earlier demixing and a larger final pattern; rather, it means that in the 2.0 s^{-1} case, it cannot safely be concluded whether the initially demixed regions were a result of demixing at the syringe walls (as is the case in the 3.7 s^{-1} experiment) or simply a result of air exposure.

Based on the fact that moisture can cause phase separation, one might suspect that none of the demixing observed in the step-shear experiments is shear-induced, but rather a slow diffusion of moisture from the air into the sample (since, as shown in Figure 2.1, the sample is exposed to air at the perimeter of the parallel plates). In order to eliminate this possibility, a control experiment was performed in which a sample was loaded and sheared at 0.8 s^{-1} for 20 minutes. No demixing was observed (data not shown) during the entire experiment, indicating that the changes in scattering pattern observed during the

step-shear experiments were in fact shear-induced and not a result of exposure to the atmosphere at the sample edges.

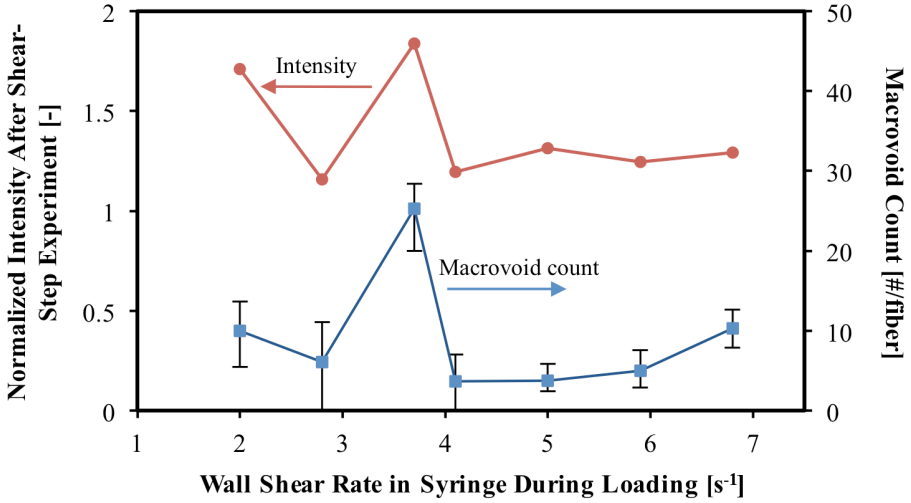

Figure 2.4 The upper data set shows the normalized SALS pattern intensity resulting from step-shear experiments conducted using seven different syringe speeds. The lower data show the macrovoid count from the corresponding extrusion experiments.

While the shear history dependence described above might be of fundamental interest, it is of little practical importance without any knowledge of the accompanying microstructural effects for spun fibers. Therefore, it was crucial to explore these same shear histories in the context of fiber extrusion experiments. The lower data set in Figure 2.4 shows the results of the fiber analysis from these extrusions; fibers were snapped and imaged with SEM to count macrovoids. Error bars represent the maximum and minimum observed macrovoid count after analyzing fiber cross sections at three locations along each extruded fiber. When compared with the intensity measurements from the step-shear measurements, the results are quite striking. As these data illustrate, the fiber extruded after being subjected to an initial loading shear rate of 3.7 s^{-1} contained

significantly more macrovoids than the other fibers. The dramatic difference in macrovoid formation between the fibers extruded after syringe shear rates of 3.7 and 4.1 s^{-1} can be seen in Figure 2.5. Since 3.7 s^{-1} was also identified as a 'nucleating' shear rate in the shear-SALS experiments, this suggests that shear-induced demixing can cause, or at least contribute to, macrovoid formation.

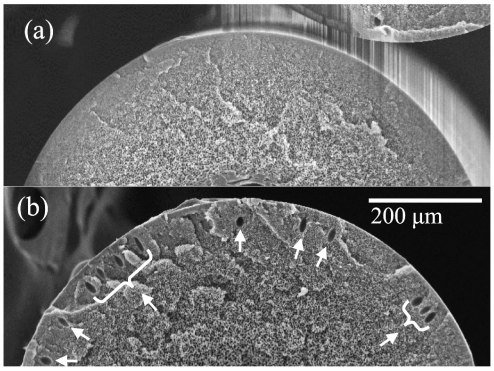

Figure 2.5 SEM images illustrating the effect of shear history on macrovoid formation; the fibers were extruded after filling syringes with shear rates of (a) 4.1 s^{-1} and (b) 3.7 s^{-1}.

A closer examination of the length scales probed in these two sets of experiments can provide a better understanding of the link between shear-induced demixing and macrovoid formation. The SALS patterns that were observed after demixing had occurred in the shear-step experiments indicated microstructural length scales on the order of 10 μm, which is the same length scale over which macrovoids are observed. Hence, it seems logical that the two phenomena would be related. This is also consistent with the view of many membrane researchers who believe macrovoid formation to be a result of inhomogeneous phase separation. These results strongly suggest that shear-induced demixing could be a source of the inhomogeneities, and hence of the macrovoids.

In order to further support the conclusion that some shear rates promote demixing while others do not, a set of experiments was designed to test whether the effect of 'nucleating' a sample during loading could be removed by shearing it at a shear rate identified as a 'mixing' or 'one-phase' shear rate after loading was completed. Figure 2.6 shows the intensity vs. time profiles for this set of experiments. The first case represents a sample that was loaded using a shear rate known to cause syringe demixing (3.7 s^{-1}) and then measured immediately using the same step-shear series described in Table 2.1. As expected, this sample displayed a large, intense scattering pattern that is characteristic of a sample that was already partially demixed at the start of the experiment. In the other experiment, a sample was loaded into the measuring cell using the same nucleating syringe rate, but then sheared for 20 minutes at 0.8 s^{-1} prior to the step-shear experiment. This pre-shear rate of 0.8 s^{-1} was chosen because it did not induce demixing during the original step-shear experiments shown in Figures 2.2 and 2.3. In comparison to the sample that was exposed to step-shear immediately, the pattern that developed in the pre-sheared sample was more characteristic of a sample that had *not* been nucleated. That is, compared to the sample without pre-shear, it had fewer intensity spikes during the 0.8 and 4 s^{-1} intervals, and the average intensity of the pattern at the end of the experiment was reduced significantly. This suggests that the 'mixing' interval removed, or at least diminished, the early demixing that occurred in the syringe.

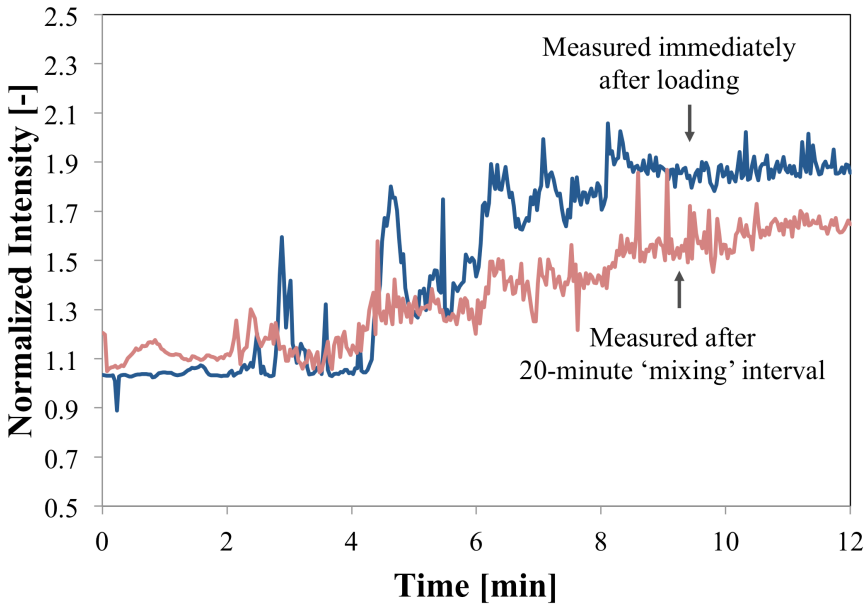

Figure 2.6 Image intensity as a function of time for two step-shear experiments. One was loaded using a 'nucleating' syringe rate and immediately thereafter was subjected to the shear-step profile described in Table 2.1 (blue line). The other (red line) was loaded at the same nucleating shear rate, sheared at a 'mixing' shear rate of 0.8 s^{-1} for 20 minutes and *then* subjected to the same step-shear profile. The beginning of the step-shear portion of the experiment corresponds to $t = 0$ s.

The fact that demixing and macrovoid formation were found to depend so strongly on subtle changes in shear history is especially noteworthy when compared with a typical laboratory spinning operation. For example, if ¼-inch tubing is used at the syringe pump outlet, typical lab-scale dope flow rates of 100-300 ml/hr result in shear rates of approximately 1-4 s^{-1} in the tubing. In the experiments presented here, the demixing behavior observed in SALS experiments and macrovoid formation in extruded fibers were both found to depend heavily on shear history in this range of shear rates. The striking implication is that seemingly unimportant aspects of the spinning process—such as supply tubing sizes—might be promoting macrovoid formation. These results further show that if this dope were being used to spin fibers, a shear rate of 3.7 s^{-1} in the early stages of the spinning process would promote early demixing and result in a more

defective final product, whereas a slight increase or decrease in shear rate would suppress premature demixing and hence, macrovoid formation.

The significance of 3.7 s^{-1} in these experimental results is not entirely understood. One might expect to observe this anomalous behavior near a shear rate of τ_c^{-1}, where τ_c is the characteristic relaxation time of the polymer and τ_c^{-1} the shear rate at which shear thinning begins. Although the onset of shear thinning in these solutions occurs around 10 s^{-1}, it is conceivable that shear stresses could begin to affect local concentration fluctuations even at shear rates below this. The most likely explanation lies in the relative magnitudes of the competing forces affecting concentration fluctuations; that is, the tendency of shear stresses to amplify them, and the osmotic and convective forces that seek to restore homogeneity.

A discussion of macrovoids in hollow fiber spinning would be incomplete without mentioning the importance of elongational stresses, which have been shown to be extremely effective in reducing defects [22]. Although no elongational stresses were employed in the extrusion experiments presented here, the current results are still useful for several reasons. First, they provide insight into *why* macrovoids form, which has been a topic of debate for some time. Secondly, even though elongational stresses have been shown to reduce defects, the underlying mechanism for this improvement is not well understood; these results provide some insight regarding this phenomenon. Consider the following scenario: assume that shear has caused a dope solution to become demixed near the channel walls within the spinneret, creating a second phase consisting of micron-sized droplets. Without elongational stresses, these droplets would certainly cause phase separation in the quench bath to proceed inhomogeneously, resulting in macrovoid

defects. Alternatively, if the fiber is aggressively stretched in the air gap, the droplets will become elongated along with the rest of the fiber, significantly reducing their dimension along the radial dimension of the fiber, i.e., the relevant direction along which the phase separation front travels. One can imagine that if the size of the droplet phase is reduced sufficiently, it will no longer disrupt the homogeneity of the phase separation process, resulting in a reduction or elimination of defects.

Of course, these results are not intended to suggest that the exact shear history dependence outlined here should be used as a guideline for spinning, as this dependence undoubtedly depends on dope composition, temperature, and other parameters. Rather, they are simply intended to highlight the fact that in some cases, the presence of seemingly inconsequential shear processes could be negatively affecting fiber microstructure. Furthermore, in systems where traditional macrovoid suppression techniques have proven unsuccessful, the effect of shear history should be considered. For example, one could change the upstream flow conditions by changing the diameter of the tubing through which the dope is pumped to test whether this reduces defect formation.

It is important to note that no significant variations in sample viscosity were observed for the various shear experiments reported here, either during the step-shear experiments conducted in the SALS setup, or in corresponding measurements conducted using a traditional concentric-cylinder measuring geometry. This is not entirely surprising, since the phase-separated system would be expected to possess emulsion-like behavior. In such a system, the bulk viscosity as measured by the rheometer is close to that of the continuous phase if any of the following conditions apply: low-viscosity droplets, a small

volume fraction of droplets, or a low surface tension between the phases; all of these are possible in this system [8].

2.4 Conclusions

SALS has been used to confirm that shear-induced demixing does in fact occur in solutions of Ultem®, NMP, and ethanol, which is not surprising considering the inherent thermodynamic instability created by the relatively high ethanol concentration. Furthermore, by varying the rate at which samples were syringed before our SALS experiments, it is found that shear-induced demixing depends not only on the instantaneous applied shear rate, but also on subtle changes in shear history. Extrusion experiments were used to show that subtle variations in shear history can dramatically affect the formation of macrovoids in solidified fibers. This indicates that demixing is closely connected to macrovoid formation, and that adjusting shear conditions in the initial stages of membrane spinning could help suppress macrovoids.

CHAPTER 3

SHEAR-INDUCED AGGREGATION AND VORTICITY ORIENTATION[2]

3.1 Introduction

In recent decades, rheologists have become increasingly interested in the microstructural effects that non-Newtonian suspending media can have on dispersed particulates [57, 60, 108, 109]. In addition to being of importance for our fundamental understanding of non-Newtonian fluid mechanics, many industrially relevant materials consist of particles suspended in complex fluids [12, 73-75, 110, 111]. These materials can be subjected to a wide range of flow conditions during processing and consumption, and their properties and performance depend heavily on internal microstructure. This provides a strong motivation for understanding the effects of flow on the underlying particle microstructure.

In previous studies, two particular types of shear-induced structure evolution have been observed, which were discussed Chapter 1. The first is the formation of long, many-particle strings or bundles that are oriented parallel to the flow direction. These shear-induced strings were first reported by Michele and co-workers [19], and have since been studied further by other researchers [59, 67-69, 112]. Although the exact criteria for string formation are not entirely understood, it seems to require that the suspending

---

[2] The contents of this chapter have been submitted for publication as: E. C. Peterson and V. Breedveld, *Shear-induced vorticity structures in dilute suspensions of silica particles in a concentrated polymer solution.*

medium be both elastic and shear thinning, as the behavior has been shown to be absent in Boger fluids [67, 69].

The second relevant type of microstructure in suspensions is a vorticity orientation, in which aggregates of particles exhibit an orientation perpendicular to shear in the shear-vorticity plane. DeGroot and co-workers observed this phenomenon, finding a two-lobed, butterfly type scattering pattern in the shear-vorticity plane for a sheared suspension of colloidal silica in a polydimethylsiloxane (PDMS) polymer melt [72]. They concluded that polymer bridging caused their particles to form flocs, which then oriented along the vorticity axis. Another example of vorticity orientation was described by Pasquino et al. [68], who studied the shear-induced structure of polystyrene (PS) spheres in a shear-thinning solution of hydroxypropylcellulose (HPC). In their experiments, which involved particles of diameter 1.2-2.8 μm, the smallest particles were found to form short, isolated strings (2-3 particles) that obtained a vorticity orientation at shear rates below the shear-thinning regime of the suspending fluid.

There have also been reports of vorticity-oriented structures in suspensions in which the continuous phase was a Newtonian fluid, but these cases generally involve a dispersed phase with its own complex characteristics, such as colloidal gels of attractive particles [113-115], suspensions of multi-walled nanotubes [116], and attractive emulsions [117]. However, we are primarily interested in hard-sphere suspensions, which would not exhibit any flow-induced anisotropy in the absence of viscoelasticity in the suspending fluid.

The aim of this chapter was to investigate the role of normal forces and shear thinning on the aggregation and orientation of colloidal silica spheres (diameter 0.5 μm) in a

mildly shear-thinning polymer solution by using small-angle light scattering under shear (shear-SALS). In order to better understand the role of shear thinning in the formation of shear-induced structure, we also investigated the evolution of the shear-induced structures under shear conditions within the Newtonian regime of the polymer solution and with a Boger fluid as the suspending fluid.

3.2 Materials and Methods

3.2.1 Sample Preparation

Most of the experiments in this report were carried out using suspensions containing spherical silica particles (500 nm diameter ±100 nm; Alfa Aesar) dispersed in solutions of 30 wt.% Ultem® polymer, 62 wt.% n-methylpyrrolidone (NMP; Sigma Aldrich), and 8 wt.% ethanol. Ultem® is a polyetherimide (molecular weight 54000 g/mol) and was provided by SABIC Innovative Plastics (Pittsfield, Massachusetts). This particular polymer is used to produce hollow fiber membranes, which are used for industrial gas separations [10]. The membranes often include dispersed inorganic particles, so there is a strong motivation to study particle behavior in Ultem® solutions. NMP is a good solvent for Ultem®, while ethanol is a non-solvent. The primary purpose for including ethanol was to lower the refractive index of the solution so that it is slightly closer to that of the dispersed silica particles. This reduces the turbidity of the suspension, and allows more light to reach the detector, so that anisotropic scattering features could be detected more easily. The presence of ethanol also reduces the solvent quality, thereby slightly increasing the viscosity and normal force characteristics of the solution relative to systems not containing ethanol. Although the results we report here were obtained using

the three-component solution (i.e., with ethanol), we performed many of the same experiments using samples without ethanol. For these experiments, similar trends regarding structure formation were observed, but the overall scattering intensity was reduced. In most cases, a particle concentration of 5.0 wt.% was used; however, in one case, a 0.50 wt.% suspension was measured to study the effect of particle concentration.

Samples were prepared by first adding the required amount of dry silica particles to NMP. To ensure that the particles were well dispersed, the mixture was homogenized using an ultrasonic homogenizer (Biologics Inc., 150VT with micro-tip) for 15 minutes. After that, approximately one-third of the required amount of Ultem® powder was added to stabilize the particles against aggregation. This mixture was placed on a slow-rolling mixer for 20 minutes, after which the remaining Ultem® powder and the necessary amount of ethanol were added. Samples were then placed back on the roller for two days to allow the polymer to completely dissolve.

We also studied particles suspended in a Boger fluid similar to one of the fluids used by Scirocco et al. [67]. This suspension contained 5.0 wt.% silica particles suspended in a solution of 0.100 wt% polyisobutene (Oppanol® B 100, M_v~1.1x10^6 g/mol, provided by BASF) in polybutene (Sigma Aldrich, M_n~920 g/mol). Oppanol® was first dissolved in tetrahydrofuran (THF) and then added to the polybutene. Particles were sonicated separately in THF, and then added to the Oppanol®/polybutene solution. Finally, the THF was evaporated using a heating bath and Schlenk line with continuous stirring.

3.2.2 Rheology & Shear-SALS Experiments

The viscosities and first normal stress differences for the suspending media were measured using a rotational rheometer (Anton Paar MCR 300) equipped with a cone-and-plate geometry (diameter 25 mm, cone angle 2°). Since water is a strong non-solvent for Ultem®, a nitrogen purge was applied during these experiments in order to prevent moisture in the air from causing phase separation at the sample edges.

The shear-SALS setup used in our experiments was purchased from Anton Paar, and is used in conjunction with the MCR 300 rotational rheometer. It employs a parallel plate measuring system in which the upper plate (diameter 43 mm) is made of quartz and the bottom plate is made of glass to facilitate light scattering. Light from a laser ($\lambda = 658$ nm) is passed through the sample and the scattered light is projected on a screen below. The scattering patterns were recorded using a CCD camera (LU135M, 1392x1040 pixels, Lumenera Corporation, Ottawa, Canada) and dedicated image acquisition software (Lucam Recorder, Astrofactum, Munich, Germany). The setup provides access to a limited range of scattering angles of $2.5° \leq \theta \leq 12°$, which corresponds to a scattering vector range of $0.4 \leq q \leq 2$ μm^{-1}. Because the shear rate in any parallel disk measuring system varies along the radial direction, in the rest of this paper we refer to the shear rate at the location where the laser passes through the sample, which is ca. 5 mm from the outer edge of the plate.

Before each experiment, a one-minute pre-shear interval at a shear rate of 0.3 s^{-1} was applied to remove any sample anisotropy caused by the loading process. Subsequently, the samples were subjected to a two-step shear protocol: a ‘structure formation’ interval, followed by a ‘recovery’ interval. Interval 1, the structure formation interval, consisted of

1800 units of strain at variable shear rate (and therefore, for various lengths of time). Interval 2, the recovery interval, consisted of 10 minutes of shear at a fixed shear rate of 0.3 s^{-1} (180 strain units). Interval 2 was used to monitor the low-shear evolution of microstructural features that were created during Interval 1.

3.2.3 SALS Pattern Analysis

Semi-quantitative analysis of microstructural features contained in structure-forming systems like the ones studied here can be carried out by using an alignment factor, A_f, defined as follows by Walker et al. [118]:

$$A_f(q) = \frac{\int_0^{2\pi} I(q,\varphi)\cos(2\varphi)d\varphi}{\int_0^{2\pi} I(q,\varphi)d\varphi} \tag{3.1}$$

In this equation, I is the scattered intensity, q is the scattering vector, and φ is the azimuthal angle. The flow direction is defined as $\varphi = 0$, making the alignment factor negative for flow-aligned structures and positive for vorticity-oriented structures. Note that a flow-aligned structure results in a scattering pattern with enhanced intensity in the vorticity direction, and vice versa. For our image analysis, we calculated A_f for each image at 60 values of q that were evenly spaced over the entire range; we then calculated an average value, $A_{f,ave.}$, for each image. In some specific cases, however, the q-dependence provided additional useful insights.

3.3 Results and Discussion

3.3.1 Viscosity and First Normal Stress Difference

Figure 3.1 shows the flow curves for the Ultem® solution and Boger fluid used in our experiments. At shear rates above 10 s^{-1}, the Ultem® solution displayed measureable

values of N_1, the first normal stress difference. For the Boger fluid, N_1 is larger and becomes detectable at a lower shear rate compared to the Ultem® solution.

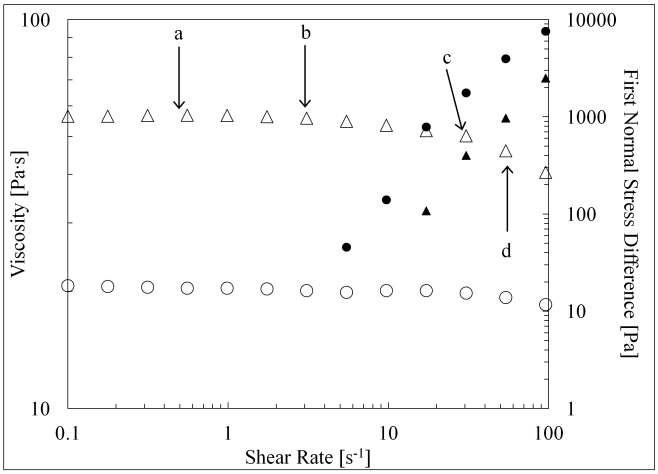

Figure 3.1 Viscosity (open symbols; left vertical axis) and N_1 (closed symbols; right axis) for the Ultem® solution (triangles) and Boger fluid (circles). The arrows labeled a, b, c, and d indicate the four shear rates that were used during Interval 1 for the experiments discussed in Section 3.3.2.1.

3.3.2 Shear-SALS

3.3.2.1 Effect of Structure Formation Shear Rate

The first set of shear-SALS experiments was intended to analyze the microstructure that developed for silica-Ultem® suspensions at four different structure formation (Interval 1) shear rates, as well as the evolution of that structure during a subsequent low-shear recovery interval (Interval 2). For these experiments, we used a 5.0 wt.% suspension of silica dispersed in the Ultem®/NMP/ethanol solution described above. An Interval 1 shear rate of 0.5 s^{-1} was used to see whether particles would form shear-induced structures under strictly Newtonian conditions. In three other experiments, shear rates of 3, 30, and 60 s^{-1} were used during Interval 1 to measure the microstructure at

shear rates approaching or within the shear-thinning regime. In all cases, the structure formation interval consisted of 1800 strain units, and the shear rate during the recovery interval was fixed at 0.3 s^{-1} (applied for 10 minutes or 180 strain units).

Plots of the average alignment factor, $A_{f,ave.}$, as a function of time for each of these experiments are presented in Figure 3.2. First, we will discuss the results observed for the experiment in which the Interval 1 shear rate was 0.5 s^{-1} (see Figure 3.2(a)). In this case, $A_{f,ave.}$ began at a negative value, indicating some degree of flow-oriented structure in the system. The alignment factor then increased until a plateau value of approximately -0.004 was reached. This initial behavior is likely due to the fact that some aggregation was present at the start of the experiment; during the loading process or the pre-shear interval, these aggregates became oriented in the flow direction before being slowly broken apart by shear forces. When the recovery interval began (at t = 60 min), $A_{f,ave.}$ dipped slightly before reaching a final value near -0.005.

In the second experiment, the Interval 1 shear rate was 3 s^{-1} (Figure 3.2(b)). The alignment factor in this case also began at a negative value—again indicating that some pre-existing particle aggregates were initially oriented in the shear direction. $A_{f,ave.}$ then increased to a positive value (approximately 0.004). (Note that the periodic dips in $A_{f,ave.}$ seen in this interval correspond exactly to the rotational period associated with this shear rate, and were likely caused by a small bubble or dust particle periodically passing under the laser beam.) At the start of Interval 2 (at t = 10 min), $A_{f,ave.}$ sharply decreased to a minimum value near -0.02 before increasing again. Two features in this experiment distinguish it from the previously discussed 0.5 s^{-1} case: the slightly positive value of $A_{f,ave.}$ during Interval 1, and the distinct "dip" in $A_{f,ave.}$ during Interval 2. The positive

$A_{f,ave.}$ values represent a slightly vorticity-oriented structure; the subsequent dip represents a transition to a flow-oriented structure, followed by a gradual transition back toward isotropy. A discussion of this result will be provided after the 30 s^{-1} and 60 s^{-1} profiles are examined.

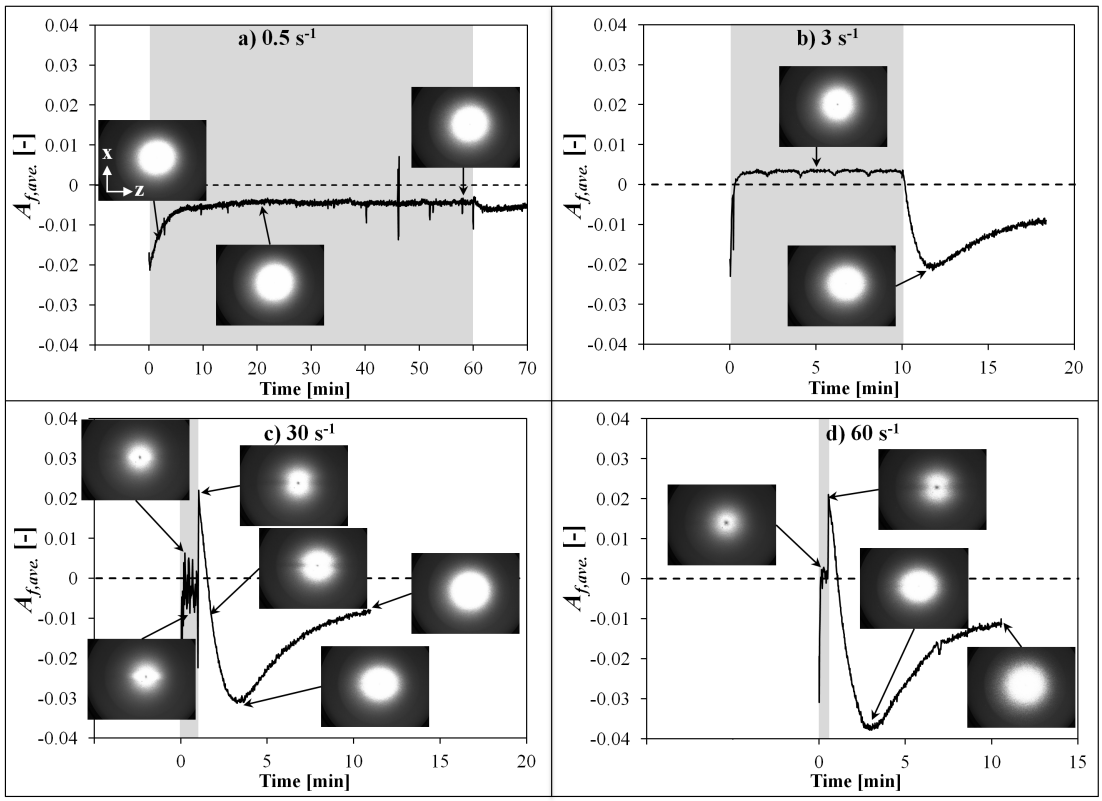

Figure 3.2 Evolution of alignment factor $A_{f,ave.}$ for four different Interval 1 shear rates. In the SALS image insets, the vertical direction represents the flow (x) direction, and the horizontal direction is the vorticity (z) direction. The shaded regions represent Interval 1.

The third case used an Interval 1 shear rate of 30 s^{-1}. As the flow curve indicates (see Figure 3.1), the solution exhibits measurable normal forces at this shear rate and is beginning to display some shear thinning. Consequently, we see these non-Newtonian effects becoming apparent in the measured $A_{f,ave.}$ profile, which is shown in Figure 3.2(c).

Interval 1 began with a negative $A_{f,ave.}$ value, as in the previously discussed cases. Then, it began to exhibit noisy fluctuations around zero as a streak-like feature appeared along the *z*-direction of the scattering pattern. We have observed this pattern previously in solutions of Ultem®, NMP, and ethanol without suspended particles [119]. It is a result of shear-enhanced polymer concentration fluctuations in the suspending fluid; these fluctuations will be discussed in more detail in Section 3.3.2.3. For now, we will focus on structure formation in the *particle* phase, and will therefore ignore the fluctuating values of $A_{f,ave.}$ during Interval 1 of this experiment. As expected based on prior studies, the streak-like feature associated with anisotropy in the polymer phase disappeared at the beginning of the second, low-shear interval, so that the evolution of the particle structure can be observed without interference during Interval 2.

At the beginning of Interval 2 of this experiment (at t = 1 min), the scattering pattern exhibited a distinct, two-lobe butterfly pattern, with a positive value of $A_{f,ave.}$, indicating that the shear conditions during the structure formation interval left the particles in an aggregated, vorticity-oriented state. The maximum value of $A_{f,ave.}$ observed in this experiment was approximately 0.02 (significantly higher than the maximum observed $A_{f,ave.}$ for the 3 s^{-1} case). As the recovery interval progressed, the 'wings' of the butterfly pattern gradually collapsed into an ellipsoidal shape. This transition from positive to negative values of the alignment factor represents the rotation of the initially vorticity-oriented particle aggregates towards an orientation along the flow direction. After reaching a minimum value around -0.03, $A_{f,ave.}$ then began increasing again. The increase toward $A_{f,ave.}$ = 0 indicates a transition to a more isotropic structure. There are two ways that oriented aggregates could return to isotropy: the aggregates could become randomly

oriented, or they could be broken apart into their primary components. Since the high viscosity of the polymer solution should not allow aggregates to become randomly oriented via Brownian diffusion (a hypothesis that will be confirmed in Section 3.3.2.2), we can interpret this return to isotropy to mean that aggregates are being broken apart.

The last experiment in this series (Figure 3.2(d)) used a structure formation shear rate of 60 s^{-1} to determine the microstructural consequences of further enhancing the non-Newtonian characteristics of the continuous phase. In this case, we found similar behavior to that of the 30 s^{-1} experiment, except that no streak along the vorticity direction was observed during Interval 1. Based on this, we can conclude that either there was no enhancement of concentration fluctuations in the polymer solution phase, or that the length scales associated with the fluctuations were outside the range explored by our scattering equipment. Instead, the pattern during the structure formation interval yielded a slightly positive alignment factor, once loading effects had been erased. Like the 30 s^{-1} case, a butterfly pattern appeared immediately at the beginning of Interval 2 (at t = 0.5 min). The average alignment factor for the butterfly pattern observed in this case was only slightly higher than that observed in the 30 s^{-1} experiment. However, there are some noteworthy differences between the two patterns. First, as we can see from the insets in Figures 3.2(c) and 3.2(d), the butterfly pattern in the 60 s^{-1} case was slightly smaller, with a reduced overall intensity. We can see this more clearly in a more detailed comparison of intensity as a function of q for the two images, shown in Figure 3.3 for two different azimuthal angles φ. The shift to smaller scattering vectors at higher shear rate can be interpreted as representing *larger* real-space features—that is, the aggregates or clusters that formed in the 60 s^{-1} experiment were likely larger than those formed at 30 s^{-1}. Note

that the intensities observed in the 30 s^{-1} pattern at low angles were sufficiently large to saturate the detector (resulting in a plateau at small q), while the 60 s^{-1} pattern did not exhibit this saturation.

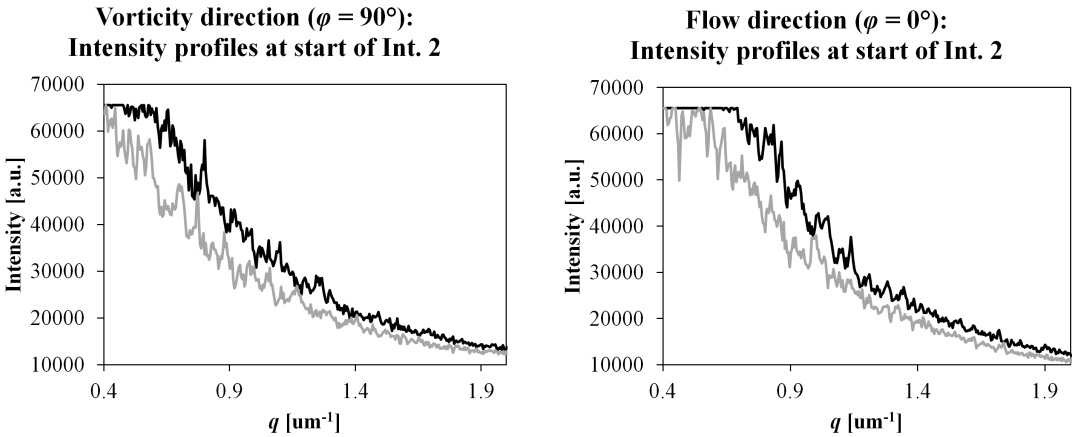

Figure 3.3 Intensity vs. q for the butterfly patterns observed at the beginning of Interval 2, for the 30 and 60 s^{-1} experiments. The black lines represent the profiles for the 30 s^{-1} experiment, while the gray lines are from the 60 s^{-1} experiment. The butterfly pattern observed in the 30 s^{-1} case was larger, resulting in larger intensities over the entire q range.

Let us now revisit the dip in $A_{f,ave.}$ that was observed during the recovery interval of the 3 s^{-1} experiment. Although there was no distinct butterfly pattern observed, as was the case for the 30 and 60 s^{-1} experiments, the recovery behavior is very similar for all three of these experiments. This indicates that even at 3 s^{-1}, some vorticity structure was formed, which then exhibited the same characteristic recovery behavior: rotation towards the flow orientation, followed by a transition back to an isotropic distribution. Although 3 s^{-1} seems to be within the Newtonian regime for this solution according to the flow curve, the local shear rates experienced by the fluid between neighboring particles is known to be greater than the nominally applied bulk shear rate. Consequently, particles

may begin to experience non-Newtonian effects at nominal shear rates lower than one might expect by simply examining the flow curve.

The results described thus far can be summarized as follows: for very low Interval 1 shear rates, no detectable microstructure is formed; Interval 1 shear rates approaching or within the shear-thinning regime result in vorticity-oriented aggregates that, during the recovery interval, first rotate to a flow orientation before getting redistributed by shear. To summarize and highlight the differences in microstructure that are generated by the various Interval 1 conditions, the recovery (Interval 2) behavior for all four cases has been assembled in a single graph in Figure 3.4(a). For the 0.5 s^{-1} case, $A_{f,ave.}$ remains essentially flat, as no non-Newtonian characteristics were present to induce any structure. For the other three cases, we see two trends. First, higher Interval 1 shear rates caused the minimum value of $A_{f,ave.}$ to be *more negative*. Secondly, higher Interval 1 shear rates caused the minima in $A_{f,ave.}$ to occur later, relative to the start of the recovery interval. This can be explained by fact that enhanced normal forces caused larger vorticity-oriented structures, which then take longer to rotate to their intermediate flow orientation. Figure 3.4(b) shows a sketch of the structural features observed during the recovery interval: first, a vorticity orientation, followed by a flow orientation and isotropic structure.

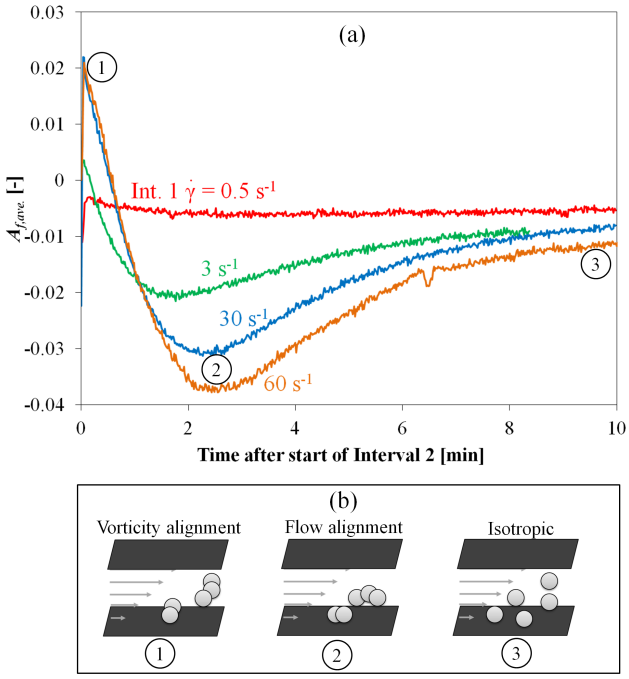

Figure 3.4 (a) Comparison of $A_{f,ave.}$ during the recovery interval for four different Interval 1 shear rates. In all cases, the recovery shear rate was 0.3 s^{-1}; (b) sketch illustrating the transition from vorticity to flow orientation, followed by an isotropic structure.

Since reports of vorticity structures are relatively rare, we feel that it is informative to make a few specific comparisons between these results and some past observations, so that a more generalized understanding of this behavior can be achieved. First, we would like to briefly comment on particle size effects. In the studies by Pasquino et al., vorticity orientation was observed only for the smallest particles investigated, while larger particles exhibited only flow-oriented structures. Our observation of vorticity-oriented aggregates is in qualitative agreement with this, in that our particles (0.5 μm) are smaller than the smallest particles they studied (1.2 μm). The vorticity structures observed by DeGroot and co-workers involved particles that were even smaller (50 nm). These observations suggest that, in general, vorticity orientations are preferred for small

particles, while flow-oriented strings are preferred for large particles; this transition seems to occur around a particle diameter of 1 μm. The 1.2 μm particles in the Pasquino study exhibited *both* orientations depending on the shear rate, suggesting that for particles close to this transition size, there is an additional transition with regards to shear rate. That is, vorticity orientations are preferred at low shear rates, and flow orientations are preferred at higher shear rates.

We would also like to briefly discuss our findings regarding the shear rates required for the formation of vorticity structures. Pasquino et al. found vorticity orientation in their suspensions at shear rates below the onset of shear thinning, while shear thinning caused the vorticity-oriented aggregates to flip to a flow-orientation, followed by migration toward the shearing surface where they grew into larger, flow-oriented structures. In our case, the lowest shear rate explored was well below the shear-thinning regime of the continuous phase, and did not produce any vorticity-oriented structures. Larger shear rates that were approaching or within the shear-thinning regime did result in vorticity structures. Based on these observations, it is likely that the vorticity orientation observed by Pasquino et al. at the lowest shear rate explored was actually due to non-Newtonian effects, despite the fact that the shear rate was seemingly below the onset of shear thinning.

A brief discussion of gap size effects is also necessary. The gap size we used (600 μm) was relatively large compared to the particle size. Because we were mainly concerned with structure formation in the bulk, we did not perform experiments at smaller gap sizes. Therefore, the fact that we did not observe the scattering signatures of flow-oriented string formation at the walls should not be interpreted to mean that this

phenomenon was not present, since these surface phenomena are typically only detected at relatively small gap sizes.

It is worth pointing out that our experiments did not include direct imaging via light microscopy; imaging these suspensions is difficult due to the small particle size and the similar refractive indices of silica and NMP. However, by comparing our observed scattering patterns to previously published studies that include both light scattering and microscopy data, we can gain valuable insight regarding the structures that form in our own suspensions. For example, the patterns that were only slightly elongated along the flow direction (like the one shown in Figure 3.2(b) for Interval 1) are similar to those observed by Pasquino et al. , which were the result of a microstructure containing short, isolated, vorticity-oriented strings. The butterfly patterns shown in Figures 3.2(c) and 3.2(d), on the other hand, are similar to the patterns observed by DeGroot and co-workers. The optical images associated with those patterns revealed a microstructure with more pronounced aggregation and a more widespread vorticity orientation. The fact that a more strongly aggregated and aligned structure would form at larger shear rates is not surprising, and is consistent with the fact that we see a more dramatic recovery behavior for these cases in Interval 2.

3.3.2.2 Effect of Recovery Shear Conditions

To better understand the low-shear recovery behavior described in Section 3.3.2.1, a second series of experiments was conducted in which we varied the shear conditions used in Interval 2. For these experiments, a fixed Interval 1 shear rate of 30 s^{-1} was used. The results of these experiments are summarized in Figure 3.5, with the previously discussed

result (see Figure 3.2(c)) shown for comparison. In one experiment, the Interval 2 shear rate was changed to 0.6 s^{-1}, twice the rate used in the original case. As expected, this results in a faster transition to a flow-oriented structure and subsequent return to isotropy. Specifically, the minimum in $A_{f,ave.}$ occurred approximately 122 seconds after the start of Interval 2 for an Interval 2 shear rate of 0.3 s^{-1}, and 63 seconds into Interval 2 when a shear rate of 0.6 s^{-1} was used. This confirms, as one would expect, that the low-shear redistribution of the vorticity-oriented aggregates is largely strain-controlled. To further illustrate this, the inset of Figure 3.5 shows each result plotted as a function of strain, rather than time.

Another experiment introduced a shear reversal for Interval 2. That is, instead of applying a shear rate of 0.3 s^{-1} in the same direction as used for Interval 1, we applied shear in the opposite direction. This resulted in a temporary enhancement of $A_{f,ave.}$ at the beginning of Interval 2. The alignment factor increased for a short period before reaching a maximum, then decreased and exhibited similar behavior to the original experiment. In the inset of Figure 3.5, we can see that this result mirrors the result of the original recovery, albeit with a slight shift to the right (that is, to later times). This illustrates, as one would expect, that shear in the opposite direction eventually has the same effect of rearranging the particles to an isotropic distribution. The delay associated with this shear reversal case corresponds to approximately 45 seconds, or a strain of 13.5. This initial time delay is due to the fact that the flow reversal interrupts the particle-particle interactions that occurred in the original flow direction, and the particle interactions must be reestablished in the opposite direction. A strain of order 10 seems reasonable for the delay associated with reversal of direction [120]. The origin of the maximum in $A_{f,ave.}$ at

the beginning of Interval 2 is not entirely understood; our best hypothesis is that polymer recoil effects associated with the shear reversal could temporarily enhance the vorticity orientation of the aggregates.

In a third experiment, we imposed a 3-minute rest period before applying the Interval 2 shear rate of 0.3 s^{-1}, in order to confirm that Brownian diffusion was not the source of particle rearrangement. During this test, $A_{f,ave.}$ remained constant during the entire rest period. When shear was applied after the rest period, the structure evolution was nearly identical to the case without rest period; when plotted versus strain, this case is nearly indistinguishable from the original result. This result confirms that particles do not lose their shear-induced vorticity-oriented microstructure through diffusion, which is consistent with predictions of diffusion timescales in such a highly viscous suspending fluid (the time required for a particle to diffuse a distance equal to its own radius in this fluid is approximately 1.2 hours). This is an important deviation from the observations by DeGroot et al. In their work, vorticity-oriented aggregates quickly returned to isotropy when shear was stopped, which they hypothesized was due to elastic energy stored in particle flocs. We do not observe such behavior in our suspensions, indicating that our particle aggregates do not possess such elasticity. This is likely due to the fact that the particles studied by DeGroot were much smaller in size (50 nm). Particles of this size are much more likely to form aggregates with long-range connectivity, which can then result in elasticity.

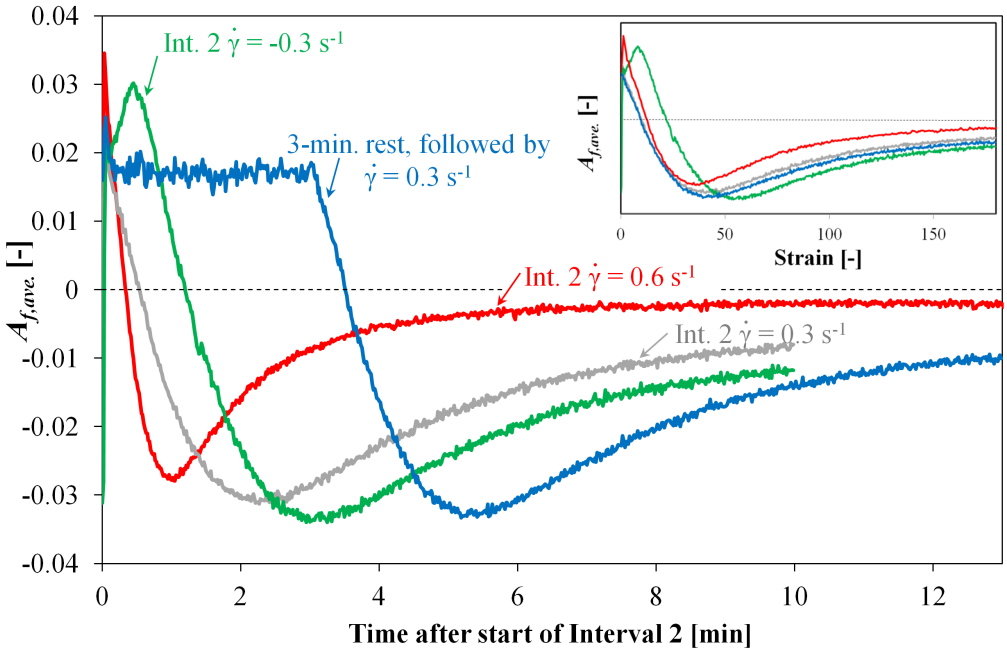

Figure 3.5 $A_{f,ave.}$ as a function of time for experiments in which Interval 2 conditions were varied. The inset shows $A_{f,ave.}$ as a function of total deformation.

3.3.2.3 Shear-Enhanced Concentration Fluctuations & Their Effect on Particle Structure

We would now like to discuss the shear-enhanced concentration fluctuations mentioned in Section 3.3.2.1. In that section, we explained that shear-enhanced concentration fluctuations occurred in the polymer phase of the suspension at a shear rate of 30 s^{-1}, causing the alignment factor to exhibit noisy oscillations between negative and positive values during Interval 1 of that experiment. As we explained previously, the positive values of $A_{f,ave.}$ were attributed to the underlying vorticity-oriented particle structure. The negative values are associated with the shear-enhanced concentration fluctuations in the polymer solution. The reason that the fluctuations cause a negative value of $A_{f,ave.}$ is that the inhomogeneous regions within the polymer solution become elongated in the flow direction due to shear forces. The two left-most insets of

Figure 3.2(c) show examples of the patterns that were observed during Interval 1 of that experiment—one in which the average value of A_f was negative, and one in which it was positive. Despite the fact that the two images have $A_{f,ave.}$ values with opposite signs, they actually exhibit quite similar lemon-like shapes; the first one has slightly more pronounced intensity across the horizontal direction, causing the average value of A_f to be negative. To illustrate this more clearly, we have calculated A_f as a function of q for these two images, and the result of that analysis is shown in Figure 3.6. In both cases, we can see that A_f is negative for small q values and positive for large q. The negative values of A_f at small q are due to the aforementioned shear-enhanced concentration fluctuations in the continuous phase; the positive values of A_f observed at large q are due to particle clusters oriented along the vorticity axis. The contribution from the polymer phase tends to be noisier, causing fluctuations in the average alignment factor. When the shear rate is reduced at the beginning of the recovery interval, shear forces are no longer strong enough to enhance the fluctuations along the flow direction, so the anisotropy associated with this feature disappears.

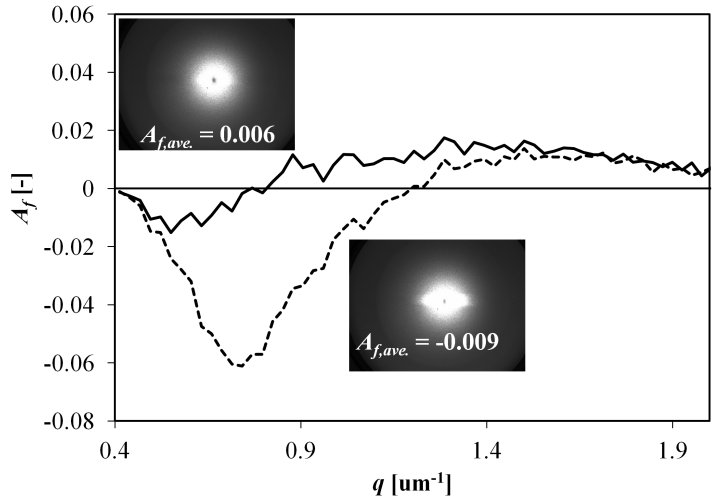

Figure 3.6 Alignment factor as a function of scattering vector for two representative patterns obtained during Interval 1 of the experiment shown in Figure 3.2(c) (Interval 1 shear rate = 30 s^{-1}); these images demonstrate the effect of shear-enhanced concentration fluctuations in the continuous phase on the average alignment factor, which accounts for the noise observed in the first minute of the experiment.

Interestingly, these fluctuations in the continuous phase did not always occur at a shear rate of 30 s^{-1}. In a separate repetition of exactly the same experiment (5 wt.% suspension; Interval 1 shear rate of 30 s^{-1}), there was no indication of demixing in the polymer solution phase, and $A_{f,ave.}$ remained positive during Interval 1 (similar to the Interval 1 behavior observed at a shear rate of 60 s^{-1}). The observation of these two distinct Interval 1 behaviors allows us to conclude whether the concentration fluctuations have any effect on the particle structure that forms. Figure 3.7 shows a direct comparison of the first two minutes of both 30 s^{-1} experiments. Note that essentially the same vorticity orientation and reorientation behavior are found at the beginning of Interval 2, despite the deviations in scattering anisotropy during Interval 1. This result confirms that shear-enhanced concentration fluctuations in the polymer solution have little effect on the shear-induced structure of the particles. Although we do not entirely understand the

mechanisms that govern shear-enhanced concentration fluctuations in these systems, we have shown in previous studies that subtle changes in shear history during syringe loading can affect this phenomenon [119]. Since we did not control the syringe speed used to load the samples for the suspension experiments, they may have experienced slightly different shear histories, which likely accounts for the variation in their Interval 1 behavior.

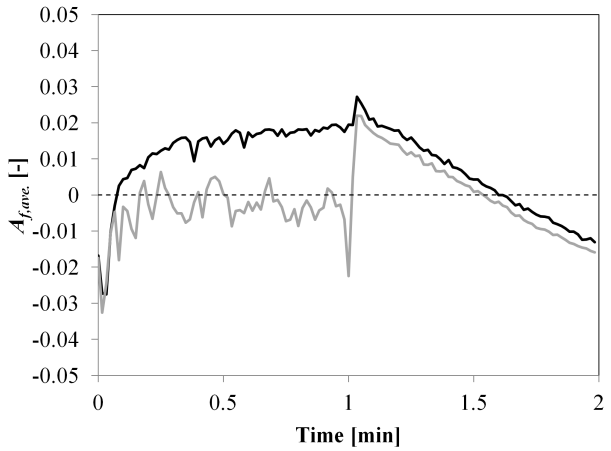

Figure 3.7 $A_{f,ave.}$ evolution for two experiments with identical samples and shear conditions (5 wt.% silica; Interval 1 shear rate of 30 s^{-1} and Interval 2 shear rate of 0.3 s^{-1}); the difference between the two experiments is that in one case, shear-enhanced concentration fluctuations caused $A_{f,ave.}$ to be negative (gray line) in Interval 1, while in the other case (black line), without the fluctuations, $A_{f,ave.}$ was positive.

3.3.2.4 Viscosity and Intensity Effects

Thus far, we have mostly examined the evolution of the average alignment factor from the scattering patterns, but a more detailed analysis can provide further insight. For example, by looking at the pattern intensities for specific azimuthal angles, we can gain additional information regarding the evolution of the microstructure during the recovery interval. Also, the shear-SALS setup provides simultaneous viscosity data, which allows

us to understand how the microstructure affects the measured stress in the system. Figure 3.8 shows the average intensities along the flow and vorticity directions (labeled I_{flow} and $I_{vort.}$, for $\varphi = 0°$ and 90°, respectively) during Interval 2 for two experiments that were discussed previously (see Figure 3.5), as well as the viscosity data during these experiments. In both experiments, the Interval 1 shear rate was 30 s^{-1}, while the Interval 2 shear rate was either 0.3 or 0.6 s^{-1}. I_{flow} and $I_{vort.}$ represent the intensity at the given φ value averaged over the entire q range. Several key observations can be made from these graphs. First, in both experiments, the measured viscosity and intensities gradually increase with time. This slow viscosity increase did not occur for control experiments on Ultem® solutions without dispersed particles (data not presented), supporting the hypothesis that it is related to particle microstructure. Furthermore, the growth of intensities and viscosity in the suspensions is faster for the 0.6 s^{-1} case, as compared to 0.3 s^{-1}; this indicates, as stated previously, that the recovery process is strain-controlled. Also, it is noteworthy that the growth of $I_{vort.}$ is significantly faster than for I_{flow}.

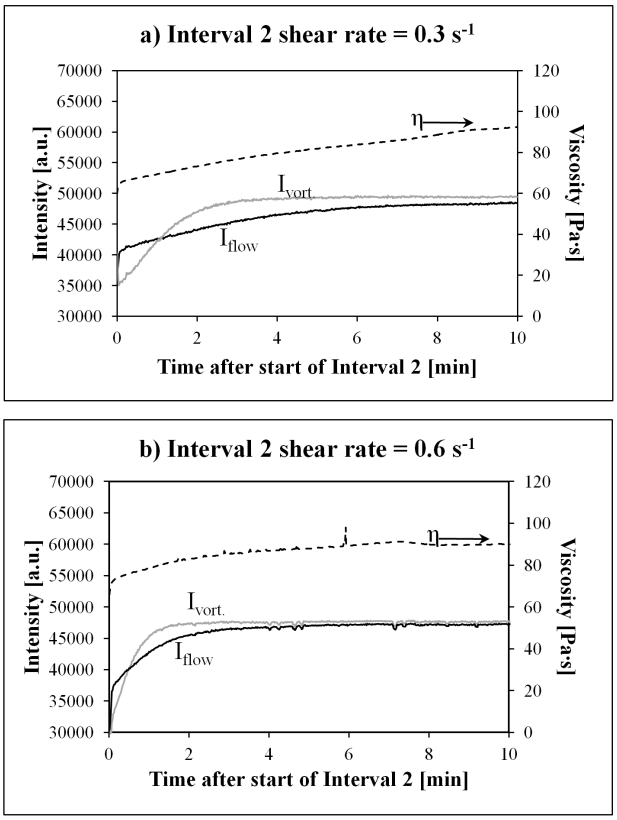

Figure 3.8 Measured viscosity and intensities during the recovery interval after an Interval 1 shear rate of 30 s^{-1}. In (a), the recovery shear rate was 0.3 s^{-1} and in (b), it was 0.6 s^{-1}.

The intensity values along the flow and vorticity directions can be interpreted as a representation of the density fluctuations along those axes in real space. As aggregates rotate from their vorticity orientation at the start of Interval 2, to a flow orientation, this restores the previously diminished fluctuations along the vorticity direction, resulting in an increase in $I_{vort.}$. Meanwhile, shear forces are simultaneously breaking apart the aggregates, thereby restoring fluctuations—and therefore the intensity—along the flow direction. The fact that $I_{vort.}$ grows more quickly than I_{flow} indicates that the orientation change happens more quickly than the breakup of aggregates.

Another interesting result is the fact that in both cases, the viscosity growth closely tracks I_{flow}, while the faster transition in $I_{vort.}$ is essentially uncorrelated with the measured viscosity. This indicates that the viscosity of the suspension is more strongly dependent on the degree of aggregation than on the orientation of aggregates. It should be noted that at long times, these polymer samples become phase separated near the plate edges due to moisture from the surrounding air, which can then cause erroneous viscosity measurements. In Figure 3.8, the measured viscosity shows a subtle but detectable change in curvature approximately 7 minutes after the start of Interval 2; this is likely due to phase separation at the sample edges. The intensity measurements are not affected by the early stages of phase separation, because the light scattering measurements occur ca. 5 mm from the plate edge.

Another pair of experiments that further illustrates the relationship between measured viscosity and scattered intensity is presented in Figure 3.9. Here we have also displayed the data obtained during the pre-shear interval, since it is particularly enlightening. The shear rates applied for these two experiments are shown at the top of each figure. First let us look at Figure 3.9(a). Here, the viscosity experienced some slow growth during the pre-shear interval, followed by a sharp decrease at the start of Interval 1 due to the shear-thinning nature of the polymer solution. Then the measured viscosity exhibited oscillations that decreased in amplitude over the duration of Interval 1. These oscillations are an artifact associated with sample loading effects; in the plate-plate measuring geometry for shear-SALS, the plate is contained within a cup, so that edge effects can occur between the plate edges and the cup wall in case of imperfect loading; the effect typically manifests itself through stress oscillation as the two wetted surfaces pass each

other periodically, and the viscosity oscillations can therefore be ignored. More importantly, though, when the shear rate was returned to 0.3 s^{-1} for the recovery interval, the viscosity reduced to a value lower than the starting viscosity of the pre-shear interval and then slowly increased. Comparison of the viscosity data to the time-resolved values of $I_{vort.}$ and I_{flow} again reveals a close correlation between the evolution of viscosity and the measured intensities. Like the viscosity, the intensities dropped to values lower than their starting values at the start of Interval 2. The viscosity again closely tracks I_{flow}, particularly for t = 2-3 minutes, during recovery from the high shear rate. While intensity in the vorticity direction also increased during this final interval, this occurred on a different time scale than the growth of I_{flow} and the viscosity.

For the experiment shown in Figure 3.9(b), Interval 1 consisted of one minute of rest, instead of the 30 s^{-1} in Figure 3.9(a). We can see that during the recovery interval, the viscosity and intensities picked up exactly where they left after the pre-shear interval. Unlike the experiment shown in Figure 3.9(a), there was no microstructural reorganization and therefore no changes in viscosity or intensities occurred.

We should note that although the viscosity oscillations observed in Figure 3.9(a) are an artifact due to overfilling, the relative change in viscosity between the first and third intervals is not an artifact. To prove this, the viscosity measurements were repeated in a concentric cylinder geometry, which is not compatible with light scattering, but is less sensitive to overfilling. The same trends were observed in these control experiments (data not shown): for the 30 s^{-1} case, the viscosity at the beginning of the recovery interval was lower than it was at the end of the pre-shear interval; for the rest case, the viscosity restarted where it left off at the end of the pre-shear interval.

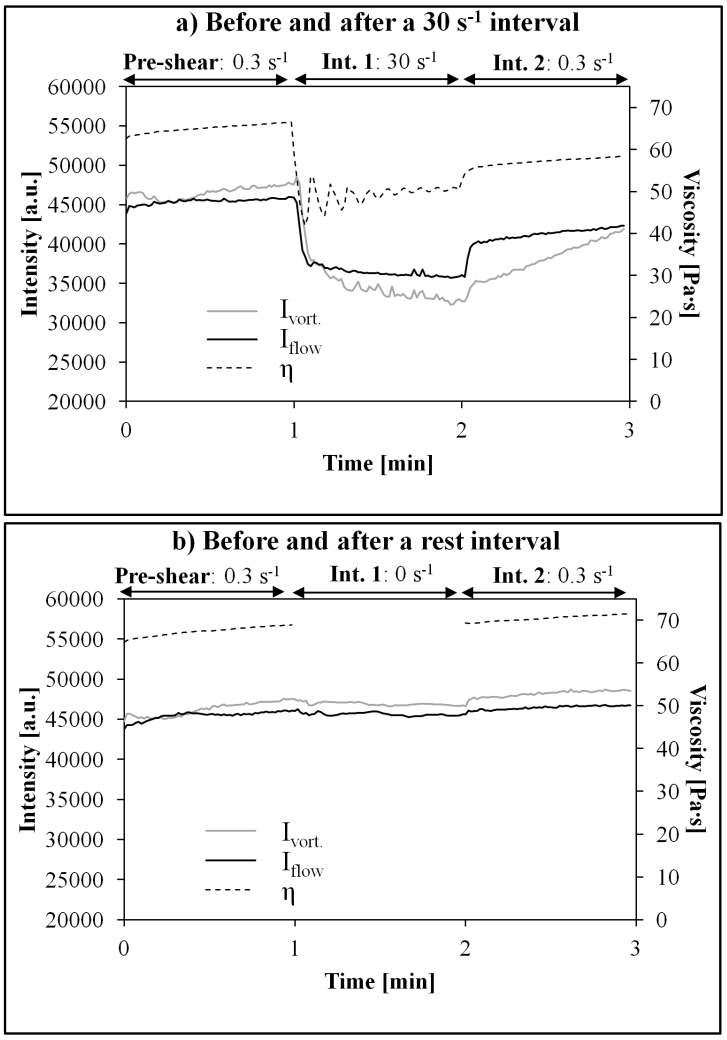

Figure 3.9 Viscosity and intensities measured at a low shear rate before and after one minute of (a) shear at 30 s^{-1} and (b) rest.

3.3.2.5. Effect of Particle Concentration

To investigate the effect of particle concentration, we analyzed a sample with only 0.5 wt.% particles. For this experiment, we used an Interval 1 shear rate of 30 s^{-1} and an Interval 2 shear rate of 0.3 s^{-1}, because these conditions yielded prominent changes in microstructure (Figure 3.2(c)). The results of this experiment are depicted in Figure 3.10, together with the previously discussed results for a 5 wt.% suspension. For the 0.5 wt.%

sample, polymer solution effects clearly dominate the light scattering signal and shear-enhanced concentration fluctuations in the continuous phase cause the alignment factor to be negative and noisy during Interval 1. Additionally, we do not see any significant butterfly pattern at the start of the recovery interval. The insets of Figure 3.10 show two representative images from this experiment, which can be compared with the images from the corresponding 5 wt.% experiment in the insets of Figure 3.2(c). Note that the reduced particle concentration results in a pattern with much less intensity.

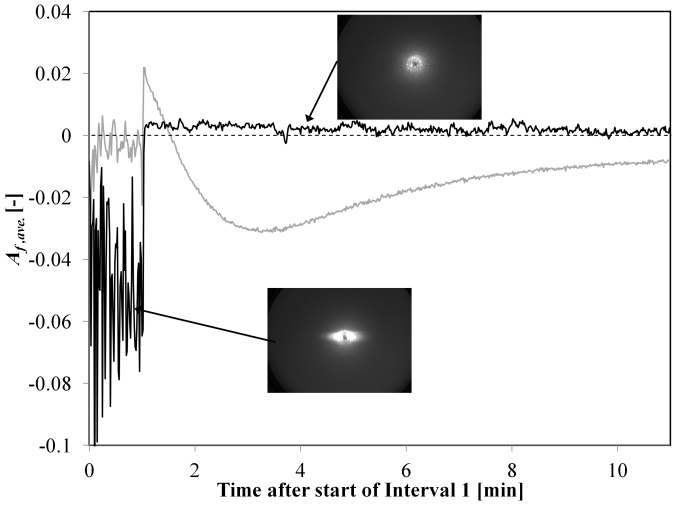

Figure 3.10 $A_{f,ave}$ measured for two different silica concentrations. The gray line represents a sample containing 5 wt.% silica, and the black line 0.5 wt.%; the Interval 1 shear rate was 30 s^{-1} and the Interval 2 shear rate was 0.3 s^{-1}.

The results of this experiment are consistent with our interpretation of structure formation, since the formation of vorticity-oriented structures is dependent not only on non-Newtonian characteristics in the continuous phase, but also on particle-particle interactions, which will happen at a much reduced frequency at low particles concentrations, thus limiting the formation of any structures.

3.3.2.6. Structure Formation in a Boger Fluid Suspension

In order to determine whether the formation of structures in these solutions is driven by normal forces alone, or by a combination of normal forces and shear thinning, we repeated the experiment using a Boger fluid as the continuous phase. As shown in Figure 3.1, this fluid exhibits larger normal stresses than the Ultem® solution; it also exhibits a relatively constant viscosity, although there is admittedly a slight degree of shear thinning at higher shear rates. Based on these rheological differences, we can safely state that if normal forces alone are the source of the shear-induced structure, then the structure formed in the Boger fluid should be enhanced relative to the Ultem® solution. To test this hypothesis, we measured a Boger fluid suspension for an Interval 1 shear rate of 30 s^{-1} and an Interval 2 shear rate of 0.3 s^{-1}, and compared this to the Ultem® case.

The results indicate that *less* structure was formed in the Boger fluid suspension. The average alignment factor for the recovery interval of this experiment is shown in Figure 3.11. Despite having similar overall scattering intensities, the calculated values of $A_{f,ave.}$ were significantly less in magnitude for the Boger fluid than for Ultem®, which is in agreement with the visibly less anisotropic patterns shown in the insets of Figure 3.11. While the Ultem® suspension exhibited a distinct butterfly pattern, this feature was noticeably absent from the Boger fluid experiment. The fact that the fluid with larger normal forces and less shear thinning exhibited less structure formation confirms that shear thinning is actually a necessary condition for structure formation.

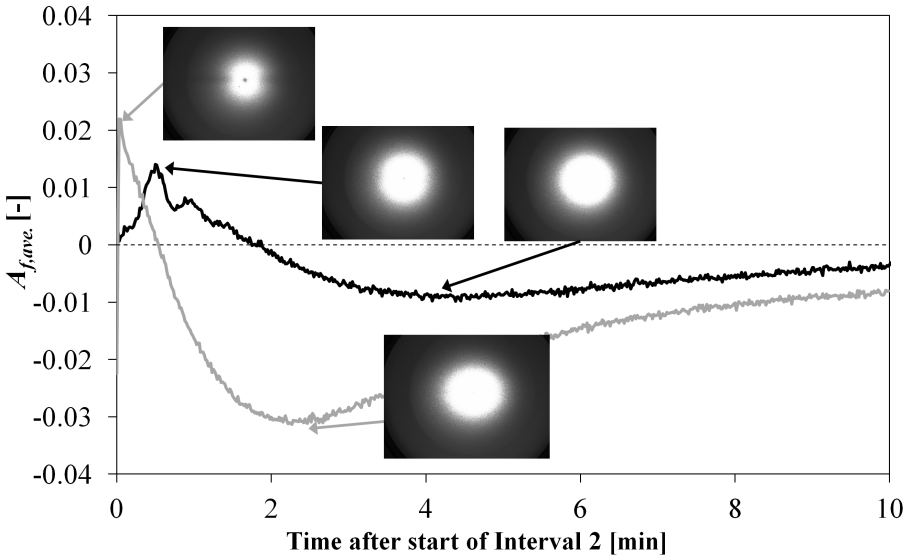

Figure 3.11 $A_{f,ave.}$ during Interval 2 for a Boger fluid suspension (black line), with the previously discussed Ultem® result shown for comparison.

We believe that the mechanism for the shear-induced structure observed in the silica-Ultem® suspensions can be explained as follows: shear thinning is responsible for particle aggregation, and then normal forces cause the resulting aggregates to orient in the vorticity direction. That is, as particles pass each other in shear flow, the region between them experiences a larger shear rate, causing a localized reduction in viscosity. This reduced resistance between them results in a tendency to move toward each other. Normal forces then act on the aggregate, orienting it in a direction perpendicular to shear. This framework leaves two possible explanations for the slight anisotropy observed in the Boger fluid suspension. The first is that some aggregates were already present in the suspension, and the large normal forces associated with the Boger fluid oriented those pre-formed aggregates, resulting in some detected vorticity orientation. Alternatively, the slight degree of shear thinning in this fluid could be the source of some mild aggregation

(in comparison to the Ultem® solution) into structures that would be aligned along the vorticity axis by the strong normal forces.

3.4. Conclusions

Using shear-SALS, we investigated the shear-induced formation of vorticity-oriented particle aggregates suspended in a shear-thinning polymer solution, a phenomenon that has been observed previously but was not well understood. The vorticity structure exhibits some interesting features that distinguish it from past observations of vorticity structures in similar materials. For example, the vorticity structures we observed remain intact after shear is stopped. Also, we only observed the structures at shear rates near or above the shear-thinning transition. For the lowest shear rate investigated, which was well within the Newtonian regime of the polymer solution, no vorticity orientation occurred. For shear rates in the shear-thinning regime, higher shear rates resulted in more pronounced structures, even for equivalent amounts of total strain. This indicates that the formation of vorticity-oriented aggregates is not purely strain-controlled, but that the structure becomes more pronounced (i.e., more aggregated and oriented) as the suspending solution becomes increasingly non-Newtonian.

We found that the vorticity structures formed at high shear rates do not remain intact under low shear conditions. We investigated the process by which the structures dissipate at low shear rates, and found that particle aggregates first rotate to a flow-orientation before being redistributed to an isotropic arrangement by shear forces. We used our shear-SALS results to compare the relative dynamics of these two steps, and found that the orientation transition happens more quickly than the breakup of

aggregates. As one would expect, this low-shear recovery process is strain-controlled. We also found that the suspension exhibits transient viscosity effects that are closely correlated with the measured intensity along the flow direction, indicating that the suspension viscosity depends more strongly on the degree of aggregation than on the orientation of aggregates. Finally, we conducted experiments using a Boger fluid that exhibits much stronger normal forces than the polymer solution in the study. The Boger fluid resulted in much less pronounced vorticity orientation, proving that normal forces alone are not responsible for the formation of vorticity structures. Rather, we propose that shear thinning is necessary to promote aggregation, while normal forces are responsible for the orientation of these aggregates. Both aggregation and orientation were found to be reversible processes.

CHAPTER 4

VISCOELASTICITY-INDUCED PARTICLE MIGRATION[3]

4.1 Introduction

In mixed matrix fiber spinning, high concentrations of molecular sieve particles are desired in the outermost skin layer, where separation takes place. Sieves that are not located in this selective layer do not enhance the selectivity of the fiber [9, 10, 90]. Since the skin layer accounts for only a small fraction of the total sheath layer, it is important to understand the distribution of particulates in this region. The ultimate objective is to control and optimize this distribution. Viscoelastic media can alter the distribution of particles in flowing suspensions through an effect called shear-induced particle migration. This phenomenon causes particles to travel across streamlines to preferred locations along the flow profile, resulting in a non-uniform distribution.

Figure 4.1 illustrates two possible effects that particle migration can have during spinning. If particles migrate toward the center of the channel, the concentration is lowered near the wall, the region that will ultimately become the selective skin layer of the fiber, which is undesirable. Alternatively, if they migrate toward the walls, the concentration of particles will be increased at the interface between the core and sheath layers, and, more importantly, in the outer layer of the fiber where the skin forms during phase separation.

---

[3] The contents of this chapter have been submitted for publication as: E. C. Peterson and V. Breedveld, *Viscoelasticity-induced particle migration in Poiseuille flow.*

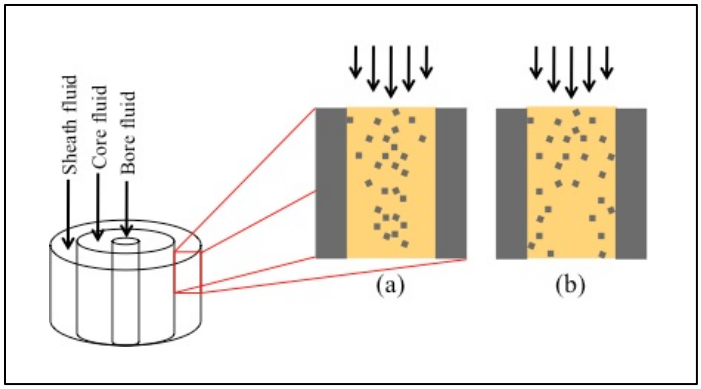

Figure 4.1 The two potential results of sieve migration in the annular spinneret channel: (a) migration towards the centerline and (b) migration toward the walls.

The rheology literature contains many examples of viscoelasticity-induced particle migration [68, 73, 97, 106]. Both types of migration (toward and away from the walls) have been observed for particles dispersed in polymer solutions, and there is no consensus about the underlying mechanism. As a result, there is no clear a priori prediction whether migration is likely to occur in membrane dopes and, if so, in which direction. If migration in either direction is found to be significant in membrane dopes under flow conditions that are relevant for spinning, two potential approaches could be taken to either minimize or maximize the effect, depending on whether the migration is favorable or unfavorable. The first is to tune the rheological characteristics of the fluid that are responsible for the migration. The other is to modify the spinneret equipment to control both the shear rate and total strain of the dope. For example, if the sieves tend to migrate away from the channel walls, then shortening the spinneret channel should minimize sieve depletion in the skin region. Alternatively, if sieves migrate toward the wall, then lengthening the channel would give the sieves more time (i.e., a larger total strain) to undergo this migration, thus enhancing the concentration of sieves in the fiber skin.

The purpose of this study was to investigate cross-stream migration in polymer solutions similar to the dope solutions used for mixed matrix spinning, and to determine the potential implications for membrane processing. Like the studies described in Chapter 3, spherical silica particles were used as model particles instead of actual molecular sieves, which would have less controlled size and shape. Rather than studying migration using an actual spinneret, we used transparent glass capillaries. This allowed the particle distribution profile to be analyzed via confocal microscopy at various locations along the length of the capillary, so that the evolution of the particle distribution profiles could be studied. Fluids with varying rheological properties were used in order to characterize the effect of shear thinning and normal forces on migration.

4.2 Materials and Methods

4.2.1 Suspension Preparation

Four different suspending fluids were used in this study, while in all cases the dispersed phase consisted of monodisperse fluorescent silica spheres of diameter 2.9 μm (CV<5%, Corpuscular, Inc., Cold Spring, NY). These particles are supplied by the manufacturer as an aqueous suspension, so a solvent-exchange process was used to transfer them into either n-methyl-2-pyrrolidone (NMP) or tetrahyrdofuran (THF) before preparing the suspensions, depending on the suspending fluid being used.

The first suspending fluid had the following composition (by weight): 11% Ultem® (polyetherimide, M_w 54000 g/mol, SABIC Innovative Plastics), 6% Luvitec® K90HM (polyvinylpyrrolidone, M_w 1.8x10^6 g/mol, BASF), and 83% NMP (Sigma Aldrich). The suspension containing this fluid will be referred to as the "Ultem®-Luvitec®"

suspension. Another Ultem®-based fluid consisted of 23.5% Ultem® and 76.5% NMP; this composition was chosen to match the viscosity of the Ultem®-Luvitec® fluid. Finally, a few studies were conducted using a third Ultem®-based fluid that was designed to mimic the composition of a typical membrane spinning dope; it consisted of 30% Ultem® and 70% NMP. These two systems will be referred to as the Ultem® 23.5% and Ultem® 30% suspensions.

To prepare the three Ultem®-based suspensions, the following procedure was used: a centrifuge tube containing particles dispersed in NMP was placed in an ultrasonic water bath (Model FS-20H, Fisher Scientific) for 45 minutes in order to disperse the particles and break up any aggregates. Meanwhile, the required amount of polymer powder was dissolved in NMP. Finally, the particles were added to the polymer solution, to achieve a final particle concentration of 0.6 wt.%, with the suspending fluid compositions described above. The suspensions were allowed to mix on a slow roller for two days to allow the polymer to fully dissolve. Suspensions were also stored on the roller to prevent particle settling.

The fourth suspension contained particles dispersed in a Boger fluid, which consisted of a low concentration of extremely high molecular weight polyisobutene (PIB) dissolved in polybutene liquid (PB), with a small amount of solvent to reduce the solution viscosity. Specifically, the composition of the suspending fluid was (by weight): 0.1% Oppanol® B150 (PIB, M_w 2.6x10^6 g/mol, BASF), 6.0% THF (Sigma Aldrich), and 93.9% polybutene (M_n 920 g/mol, Sigma Aldrich). To prepare this fluid, the high molecular weight PIB was first dissolved in THF. Particles, suspended in THF, were sonicated as described in the previous paragraph. Then, the necessary amounts of PIB-THF solution

and silica-THF suspension were added to the PB liquid. Once these components were mixed thoroughly, some THF had to be evaporated in order to reach a final concentration of 6.0% THF in the continuous phase. This was achieved using a Schlenk line to supply vacuum while heating and stirring the sample until the desired sample weight was reached.

4.2.2 Experimental Setup

Flow experiments were performed using rectangular glass capillaries that had cross-sectional dimensions of 1 mm x 0.1 mm, and a length of 100 mm (VitroCom, Mountain Lakes, NJ). In a few cases, shorter capillaries (50 or 75 mm) were used to prevent rupture at high flow rates. To attach the capillaries to a syringe, a section of the capillary (about 10 mm) was glued inside the barb portion of a female Luer-lock-to-barb connector. Figure 4.2 shows a sketch of the capillary dimensions and a definition of the coordinate system.

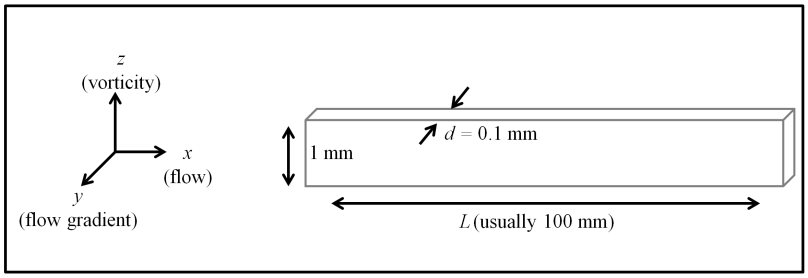

Figure 4.2 Coordinate definitions and capillary dimensions (not to scale).

Once the capillary was attached to a filled syringe, fluid flow was controlled using a syringe pump (KDS210, KD Scientific, Holliston, MA). For each experiment, fluid flowed through the capillaries for a total time approximately equal to $6 \cdot t_{res.}$, where $t_{res.}$ is

the average residence time of the fluid in the capillary. This was to ensure that startup effects (e.g., effects associated with the meniscus passing through the capillary) would not affect the final particle distribution. Although gravitational effects should be negligible over the times explored in these experiments due to small particle size and high fluid viscosity, the capillaries were positioned so that the direction of interest, y, was perpendicular to gravity (the orientation shown in Figure 4.2) to avoid any gravitational effects along this direction during the flow experiments.

Due to the large aspect ratio of the channel cross section (10:1), the velocity profile and shear rates can be estimated using slit flow calculations. For Newtonian flow through a slit of gap size d, the velocity profile, v_x, can be described using Equation 4.1 [121].

$$v_x(y) = \frac{3}{2} < v_x > \left[1 - \left(\frac{y}{d/2}\right)^2\right] \tag{4.1}$$

In this equation, y is defined as in Figure 4.2, with $y = 0$ corresponding to the centerline of the capillary. The average velocity, $<v_x>$, can be calculated using the known volumetric flow rate and the cross-sectional area of the channel.

Differentiation of v_x with respect to y, followed by a substitution of $y = d/2$ yields the following expression for the maximum shear rate in the slit, which occurs at the wall:

$$\dot{\gamma}_{max} = \frac{6<v_x>}{d} \tag{4.2}$$

These calculations assume an infinite channel width and Newtonian fluid properties, and therefore do not provide exact wall shear rates for the materials and conditions used in this study. The fact that the capillaries have a finite width results in some small deviation from the slit flow estimates. Also, the shear-thinning nature of the fluids causes an increase in the true maximum shear rates relative to those calculated for a Newtonian fluid. However, numerical calculations with COMSOL that explicitly account for the

shear rate dependence of the viscosity and the finite width of the channel, confirmed that the Newtonian slit flow estimate of Eq. 4.2 is accurate to within 10% of the true wall shear rates for all fluids and conditions used in this study. Therefore, for simplicity, the rest of this chapter will refer to the shear rates calculated based on ideal slit flow of a Newtonian fluid. Table 4.1 shows the flow rates and corresponding maximum (wall) shear rates for this study.

Table 4.1 The volumetric flow rates used and the corresponding Newtonian wall shear rates.

Flow rate [μl/min]	Wall shear rate [s^{-1}]
0.3	3.0
1.0	10
3.0	30
10.0	100
50.0	500
75.0	750
100.0	1000

A confocal microscope (Zeiss LSM 510 VIS) with a 40x oil objective was used to analyze the particle distribution within the capillaries after cessation of flow. Capillaries were optically sectioned along the *y* direction using a field of view of 318 μm x 318 μm. Upper and lower limits of the *y*-scan were chosen by detecting the particles that were closest to, and furthest from the objective (i.e., particles with the minimum and maximum *y* coordinate) and then setting the limits for the confocal scan approximately 10 μm outside these extreme locations to ensure that no particles would be excluded erroneously. Frames were then captured every 1 μm along the *y* direction within this pre-defined range of *y* values. The 100-mm long capillaries were analyzed at four locations: 30, 50, 70, and 90 mm from the entrance, corresponding to *L/d* values of 300, 500, 700,

and 900, where L is the distance along the channel in the x direction, and d is again the channel height. At each location, three scans were performed at slightly different axial positions, and the three resulting profiles were averaged. When 50-mm capillaries were used, the same methodology was used to obtain particle distribution profiles at 30 mm and 45 mm from the channel entrance.

Since the refractive index of the suspending fluids is not identical to that of the immersion oil, a vertical objective displacement of 1 μm does not necessarily correspond to a 1-μm shift of the focal plane within the sample. As a result, the y-scans produced by the instrument suggest, at first glance, that particles are located in a region larger than the actual size of the capillary. To account and correct for this artifact, measurements were performed to determine the "apparent capillary size" for each fluid. First, the inner walls of a capillary were coated with fluorescent particles. The capillary was then filled with the fluid of interest, and imaged in the confocal microscope. The locations of the particles at the walls were then used to determine the apparent channel height.

4.2.3 Image Analysis

Each image stack obtained from the confocal microscope was transformed into a particle distribution profile by summing the intensities of all pixels within each image, and plotting the total intensity as a function of y. These profiles were then analyzed quantitatively to capture three key features that were observed during our studies. The first feature was an overall reduction in the fraction of the channel cross section that was occupied by particles; we refer to that effect as "profile focusing". To quantify this phenomenon, the uppermost and lowermost frames with particles (i.e., non-zero intensity

values) were identified, and the apparent distance between them was calculated. This distance was then divided by the previously determined apparent capillary height for that particular fluid, to obtain the total fraction of the cross-sectional area occupied by particles, $A_{occ.}$.

The profile focusing analysis provides information on the distance between the uppermost and lowermost particles along the *y*-direction, but it does not provide any information about how uniformly particles are distributed. To quantify the 'shape' of the profiles, two additional parameters were defined. For these calculations, the profiles were first centered and normalized by y_{max}, the total apparent height occupied by particles, which was determined previously. Using this normalization, $y' = y/y_{max} = 0$ and 1 now represent the first and last frames with non-zero intensities, respectively. In some cases, an excess of particles was observed in the center of the channel, resulting in a strong peak at the center of the intensity profile. To quantify this characteristic, the average intensity in the range $0.45 < y' < 0.55$ (the center 10% of the profile) was calculated: $I_{ave,center}$. Then the average intensities were determined for two other regions (intermediate between the center and edges) were calculated: $0.225 < y' < 0.325$ and $0.675 < y' < 0.775$. These parameters are identified as $I_{ave,1}$ and $I_{ave,2}$. Based on these intensities, a ratio p_{center} was defined, as shown in Equation 4.3 below. This ratio is greater than 1 if there is an excess of particles in the center of the channel, and equal to 1 if the particle concentration in the center is the same as in the surrounding intermediate regions.

$$p_{center} = \frac{2(I_{ave,center})}{I_{ave,1}+I_{ave,2}} \tag{4.3}$$

The final feature of interest that was observed under certain conditions was the appearance of strong concentration peaks at the edges of the profile, often accompanied

by depleted regions directly adjacent to the peaks. Initially, an attempt was made to quantify these edge peaks in a similar way as the center peak—that is, by determining the average intensity in the outer 10% of the profile and comparing this value to the average intensity in the intermediate regions. This approach worked fairly well for cases in which the peaks were large. However, in cases where the peak-like appearance resulted from the depleted zone nearby, instead of from the absolute magnitude of the peaks, this approach did not provide a discriminating parameter. In order to better capture the edge peak feature, an algorithm was therefore developed that scans the profile from the edge *inward* until a maximum is detected, followed by a search for the subsequent minimum. The difference in intensity between the maximum and the minimum was then calculated and divided by the average intensity in the region between the edge and the minimum, to obtain an edge peak ratio, p_{edge}. Figure 4.3 illustrates this approach for a representative example of an intensity profile exhibiting edge peaks.

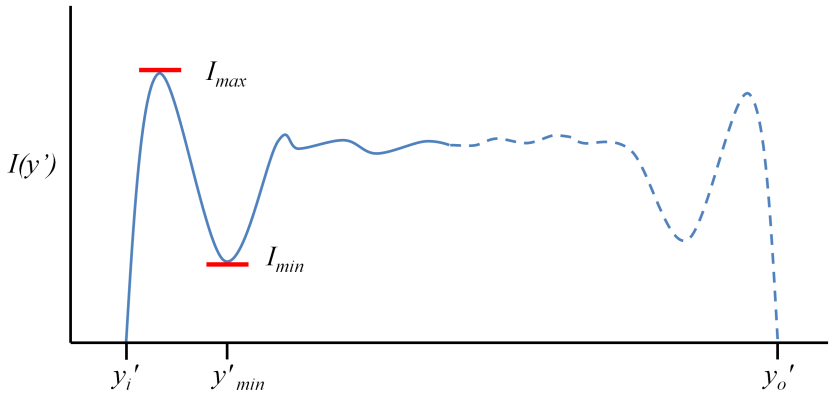

Figure 4.3 Example of an intensity profile exhibiting "edge peaks".

Equation 4.4 defines how p_{edge} was calculated. The overall peak ratio for each profile was calculated as the average of the two p_{edge} values for both edges of the profile.

$$p_{edge,i} = \frac{I_{max} - I_{min}}{I_{ave,y'_i<y'<y'_{min}}} \tag{4.4}$$

4.3 Results

4.3.1 Suspending Fluid Rheology

Shown below in Figure 4.4 are the flow curves for the four fluids used in this study, along with the values of N_1, the first normal stress difference (measured using an Anton Paar MCR 300 stress-controlled rheometer with cone-and-plate geometry, cone diameter 25 mm, angle 2°). Three of the fluids are similar in viscosity, but vary in their degrees of shear thinning and magnitude of normal forces. Due to the presence of the high molecular weight polymer, the Ultem®-Luvitec® fluid begins shear thinning at a lower shear rate than any of the other fluids. The effect of the high molecular weight polymer on N_1 can also be seen: the Ultem®-Luvitec® material exhibits much larger normal forces than the 23.5% Ultem® solution, and the normal forces become measurable at a lower shear rate. The Boger fluid exhibits the largest normal forces of all four fluids, but minimal shear thinning. The 23.5% Ultem® fluid possesses very slight shear thinning, and exhibits the smallest N_1 values of all the fluids investigated. The 30% Ultem® solution has a much higher viscosity and larger N_1 than the 23.5% solution, due to the larger polymer concentration. Significant shear thinning occurs, but the onset of shear thinning occurs at a higher shear rate than the Ultem®-Luvitec® fluid. This is due to the fact that shear thinning generally begins at a shear rate of approximately τ^{-1}, where τ is the relaxation

time of the polymer. Luvitec® has a longer relaxation time than Ultem®, due to its large molecular weight, causing shear thinning to occur earlier in that fluid.

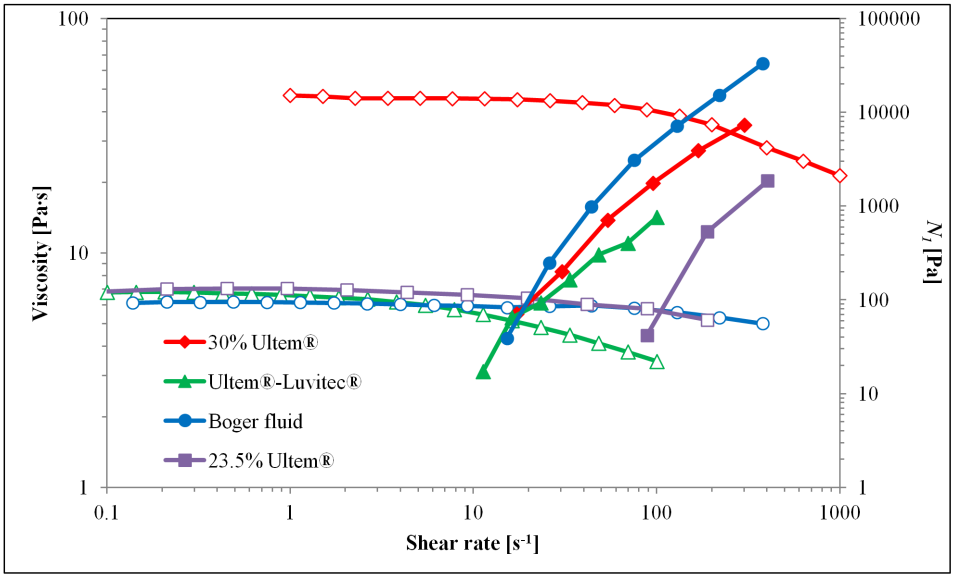

Figure 4.4 Flow curves for the four fluids used in this study. Open symbols are the viscosity (left axis) and closed symbols are N_1 (right axis).

4.3.2 Migration Results

4.3.2.1 Ultem®-Luvitec® Suspension

First, let us examine the overall features of the particle concentration profiles that were observed in the flow experiments, beginning with the Ultem®-Luvitec® suspension. Shown below in Figure 4.5 are the profiles as a function of channel position and wall shear rate. In each profile, the horizontal axis represents the relative y location in the capillary, with the dotted lines marking the location of the capillary walls. The vertical axis represents the total intensity, and therefore the relative particle concentration at that location, in arbitrary but consistent units. Each row in the figure contains the data for one particular shear rate, while the columns represent the four L/d positions that were

analyzed for each capillary (L/d = 300, 500, 700, and 900). For the largest flow rate in the series (1000 s^{-1}, the bottom row of Figure 4.5), a 100-mm long capillary could not be used, as it would fracture at such a large flow rate due to the accompanying pressure differences. Therefore, a 50-mm capillary was used, and the analysis was performed at L/d = 300 and 450.

Looking at the 3 s^{-1} data (first row), we see that the profile was mostly uniform, and that the particle distribution did not change significantly along the length of the channel. There was, however, a slight decrease in intensity with increasing values of y in each profile due to the fact that light absorbance by particles nearest to the source makes less light available to particles further away [122]. The calculations described in Section 4.2.3 were designed to prevent this issue from affecting the quantitative numerical analysis by taking advantage of the nearly linear shape of the profiles.

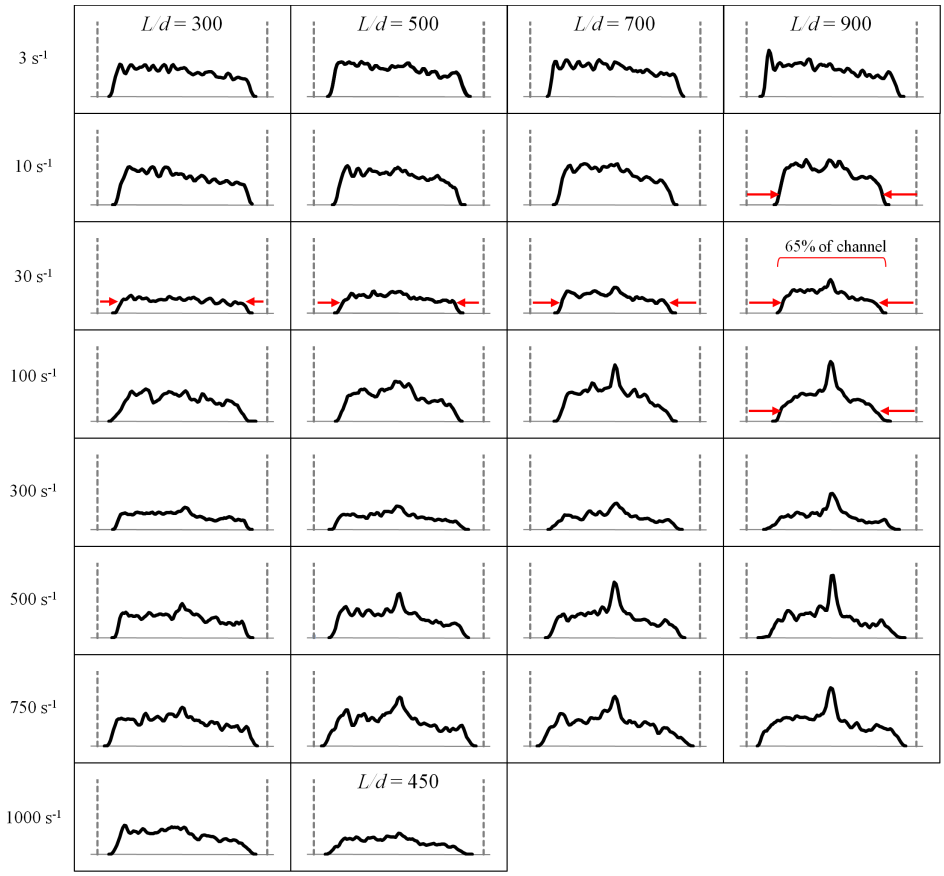

Figure 4.5 Intensity profiles for the Ultem®-Luvitec® suspension.

At intermediate shear rates, 10-100 s^{-1}, particle migration effects become apparent. In this range, particles occupied a smaller fraction of the channel than they did at the lowest shear rate, and this focusing effect progressed along the length of the channel. The red arrows in the figure highlight this feature. Profile focusing was most pronounced at a shear rate of 30 s^{-1}, when particles eventually occupied less than 65% of the channel. At 30 and 100 s^{-1}, the focusing was even strong enough for particles to accumulate at the centerline, resulting in a peak in the profile. At shear rates of 100 s^{-1} and above, the center peaks were still present, but the profile focusing was less pronounced than for 30 s^{-1}. Despite the fact that the profile focusing effect diminished at higher shear rates, the

center peaks became more distinct, and could be detected earlier in the capillaries. Figure 4.6 shows two confocal images that illustrate the difference between a relatively uniform distribution, and one with an excess of particles in the center. The images were taken from the 3 and 500 s^{-1} experiments at L/d = 900; the corresponding intensity profiles are also shown again for reference. The dashed lines represent the approximate location of the channel walls. It should also be noted that these images represent the entire volume sampled by a single confocal scan, projected onto the x-y plane; the appearance of some apparent aggregation and a particle concentration seemingly greater than 0.6 wt.% are a result of this projection.

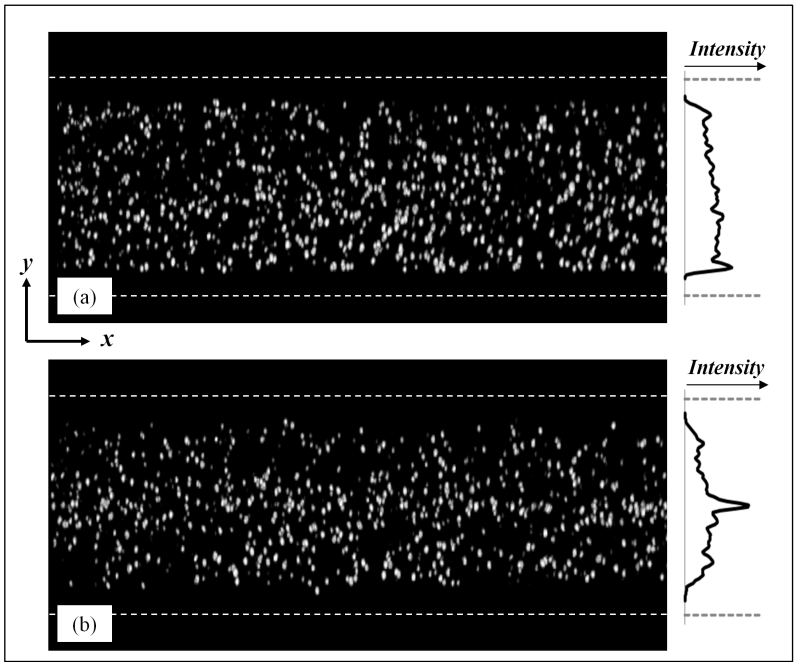

Figure 4.6 Confocal images and the corresponding intensity profiles showing (a) the uniform particle distribution obtained at 3 s^{-1} and (b) the particle distribution from the 500 s^{-1} experiment, in which particles accumulated in the center. Both images were obtained at L/d = 900.

The analysis methods described in Section 4.2.3 capture these trends quite clearly. Shown below in Figure 4.7 is the profile focusing analysis for the data presented in Figure 4.5. Shear rate is shown on the horizontal axis, and $A_{occ.}$ on the vertical axis. The figure clearly shows the trends that were described above qualitatively. At the lowest flow rates, particles occupied a relatively large fraction of the channel. As the flow rate increased, particles migrated progressively toward the center of the channel, diminishing the overall portion of the channel occupied by particles. This effect was most pronounced at the end of the capillary and at 30 s^{-1}, and became less significant again at higher flow rates.

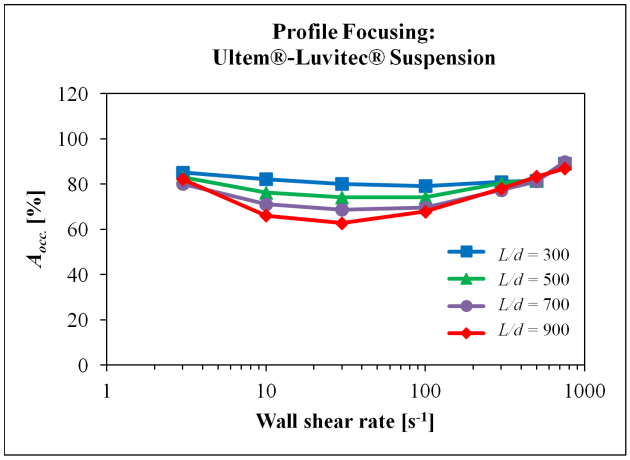

Figure 4.7 Profile focusing for the Ultem®-Luvitec® suspension.

Figure 4.8 shows the center peak analysis for the profiles. This figure depicts p_{center}, as described by Equation 4.3, as a function of shear rate. This graph shows that as the flow rate increased, the particle concentration at the center also increased, resulting in a larger p_{center}. This effect was most pronounced at a flow rate of 300 s^{-1}, and decreased slightly at higher flow rates.

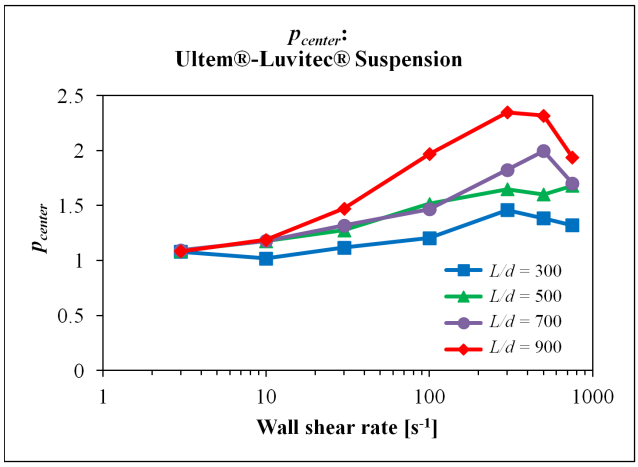

Figure 4.8 Center peak analysis for the Ultem®-Luvitec® suspension.

Figure 4.9 shows the calculated edge peak values, p_{edge}, for these data. Below 100 s^{-1}, p_{edge} remained around a value of 0.5 along the entire length of the capillary, indicating that the profile edges did not exhibit any significant enhancement in particle concentration. At shear rates above 30 s^{-1}, p_{edge} increased slightly, indicating that the particle concentration at the profile edges gradually increased.

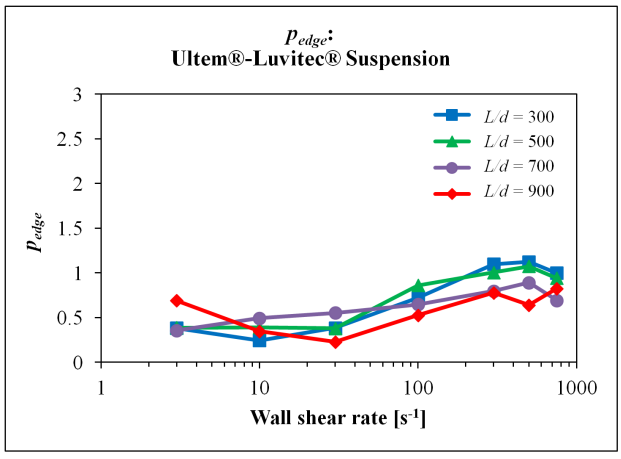

Figure 4.9 Edge peak analysis for the Ultem®-Luvitec® suspension.

4.3.2.2 Ultem® 23.5% Suspension

Next, the results observed for the Ultem® 23.5% suspension will be examined. The intensity profiles are presented in Figure 4.10. For this suspending fluid, the four lowest shear rates resulted in profiles that were nearly homogeneous; there was a slight change in the total fraction of the channel occupied by particles, although the focusing effect was decidedly less pronounced than it was for the Ultem®-Luvitec® suspension (see Figures 4.5 and 4.7). At shear rates of 300 s^{-1} and higher, distinct peaks can be seen at the profile edges, which correspond to accumulation of particles at the walls. Figure 4.11 shows confocal images obtained for a shear rate of 500 s^{-1} at L/d = 900, along with the result for 1000 s^{-1} at L/d = 300, which showed even stronger accumulation at the walls. Also shown in Figure 4.11 are images of the particles located at the channel wall, which formed very distinct strings oriented along the flow direction.

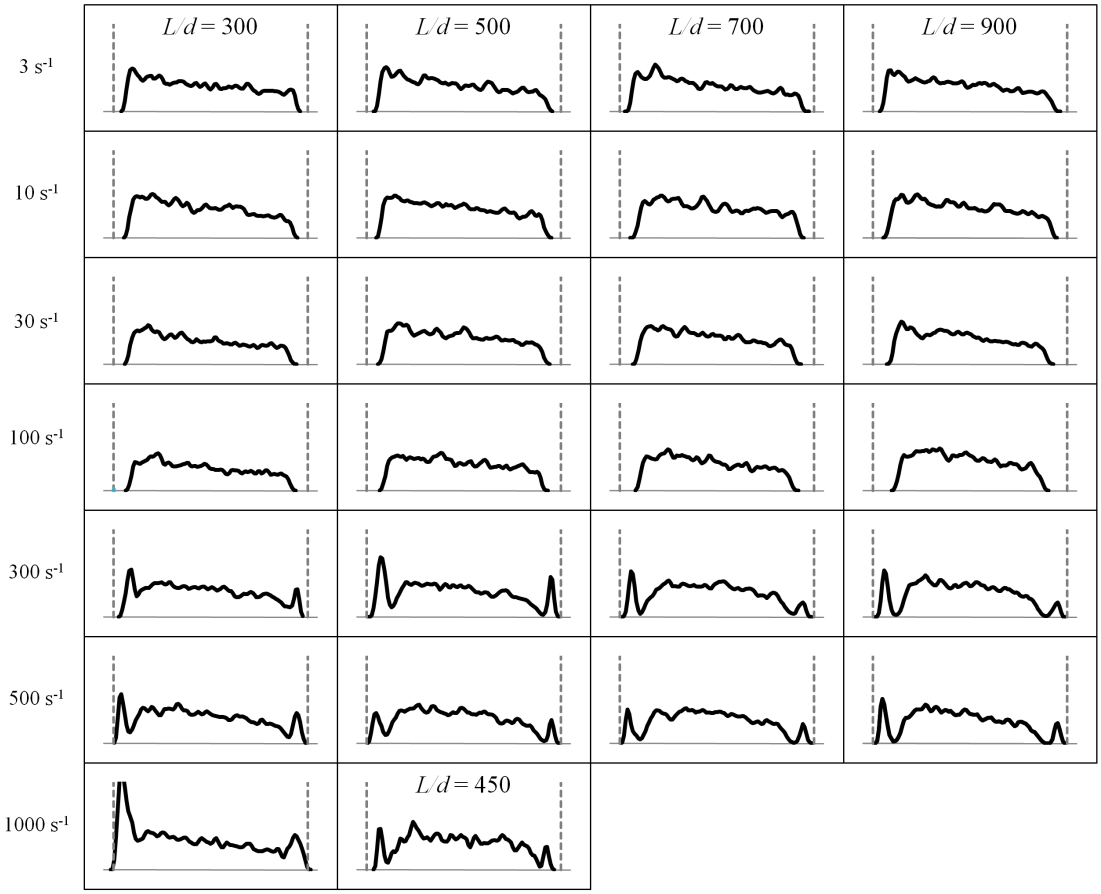

Figure 4.10 Intensity profiles for the 23.5% Ultem® suspension.

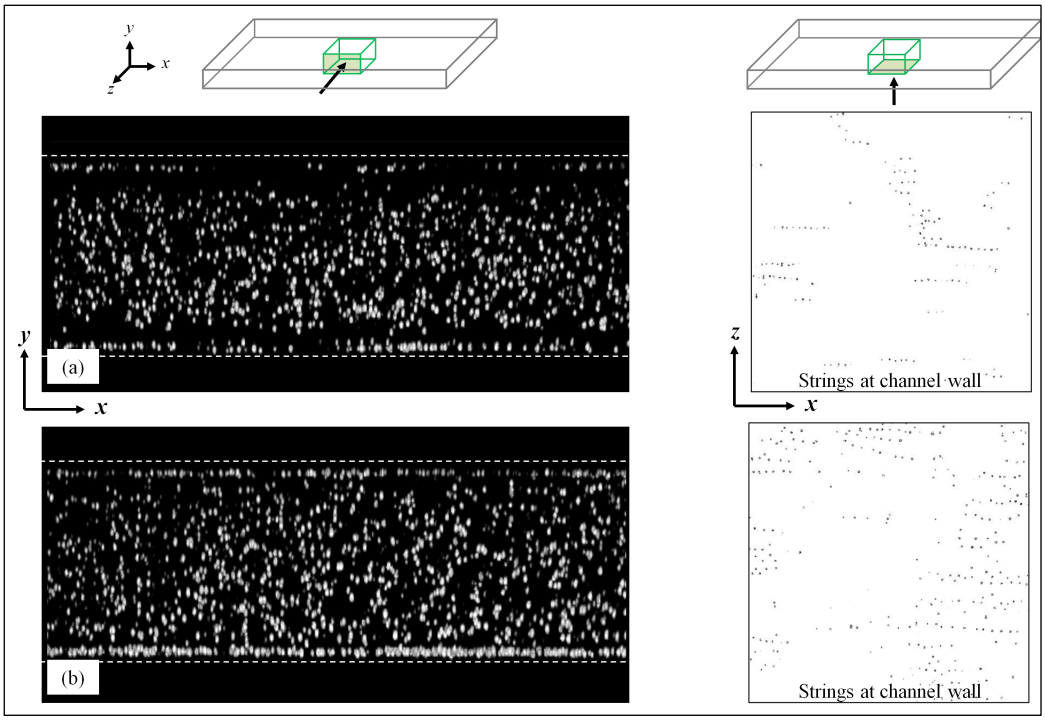

Figure 4.11 Confocal images showing the particle distribution observed in the 23.5% Ultem® suspension at shear rates of (a) 500 s^{-1} and (b) 1000 s^{-1}. Images on the right (which have been inverted for clarity) show the particle strings observed at the walls.

In Figure 4.12, the results are presented for profile focusing analysis for this system. At the lower shear rates explored—100 s^{-1} and below—a slight profile focusing was observed. Above 100 s^{-1}, this effect was reversed, and larger fractions of the channel cross section were found to contain particles.

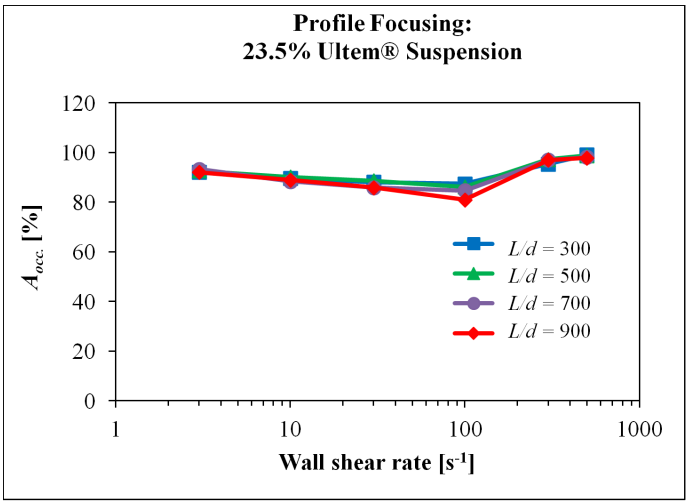

Figure 4.12 Profile focusing analysis for the Ultem® 23.5% suspension.

In the next two figures, 4.13 and 4.14, p_{center} and p_{edge} are presented for this suspension. Figure 4.13 shows the p_{center} values, which are all very close to unity, in agreement with the fact that no center peaks can be observed in this system. The edge peaks, however, appear very distinctly in Figure 4.14. The values remain less than 0.5 throughout the entire capillary for all shear rates less than or equal to 100 s^{-1}. At higher shear rates, p_{edge} increased sharply, indicating accumulation of particles at the profile edges.

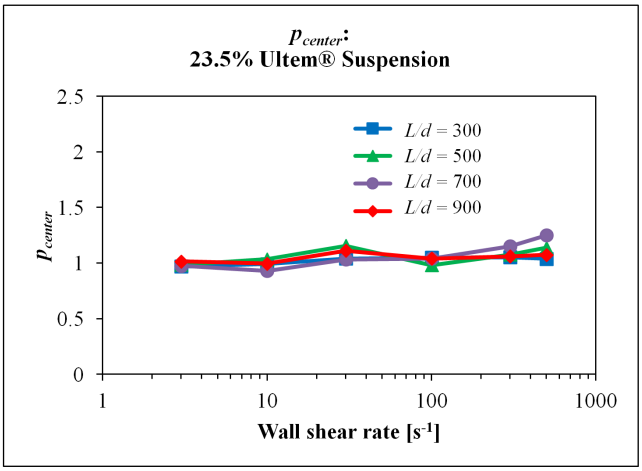

Figure 4.13 Center peak analysis for the Ultem® 23.5% suspension.

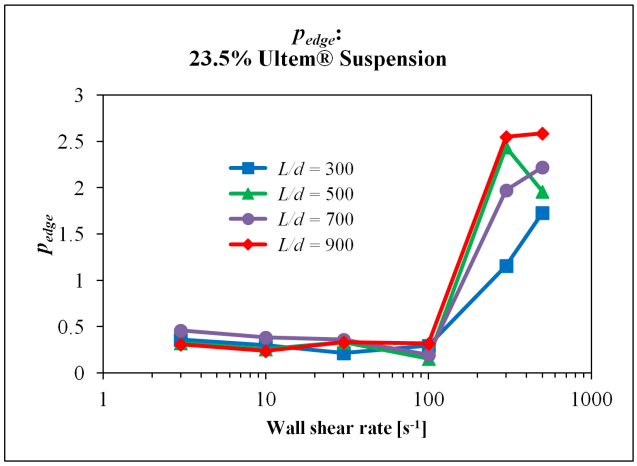

Figure 4.14 Edge peak analysis for the Ultem® 23.5% suspension.

4.3.2.3 Boger Fluid Suspension

Finally, the Boger fluid results will be discussed. The profiles from these experiments are shown in Figure 4.15, and are quite difficult to interpret. Even at the lowest flow rate, the profile appears inhomogeneous. There are small peaks at the channel walls, in addition to high-intensity regions *between* the center and walls. The subsequent flow rates exhibit similarly puzzling features, with peaks sometimes forming at the walls.

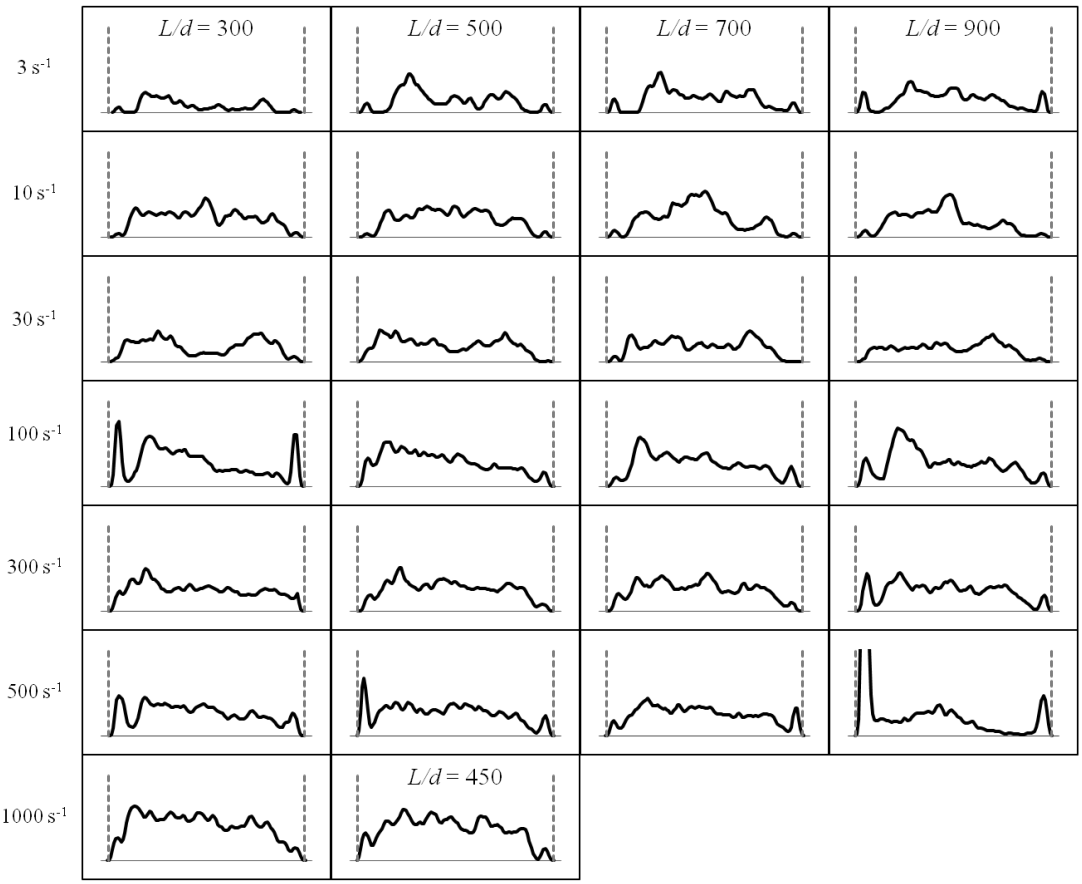

Figure 4.15 Intensity profiles for the Boger fluid suspension.

Despite the fact that these data seem to lack any clear trends, one feature is clearly absent from these results: profile focusing. As highlighted by Figure 4.16(a), particles can be found across the entire channel at all flow rates and locations that were explored. To underline the varying degrees of focusing that were observed for these suspending fluids, in Figure 4.16(b) the profile focusing curves are shown for all three fluids at L/d = 900.

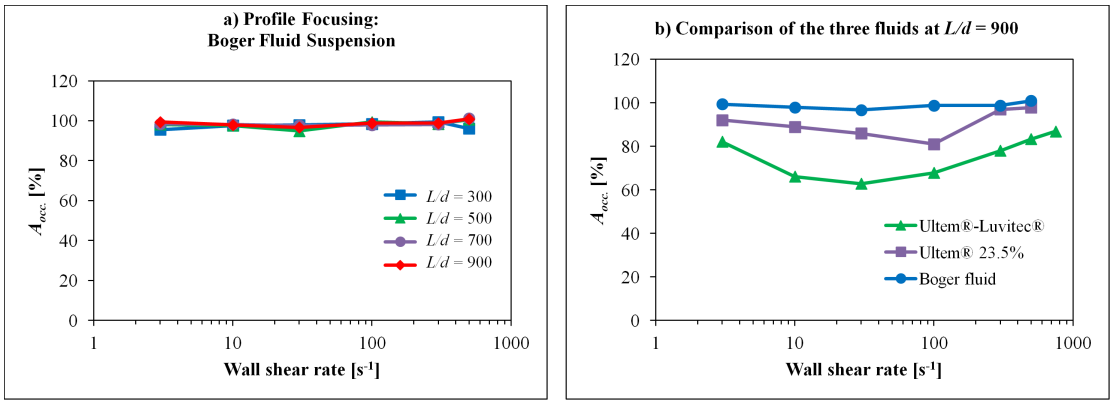

Figure 4.16 Profile focusing analysis for (a) the Boger fluid suspension and (b) the Boger fluid, Ultem®-Luvitec®, and Ultem® 23.5% suspensions at L/d = 900.

For the sake of completeness, Figures 4.17 and 4.18 contain the results of the center and edge peak analyses. These figures illustrate the lack of any trend in terms of either feature—center or edge peaks. A possible explanation for these puzzling results will be discussed in Section 4.4.3.

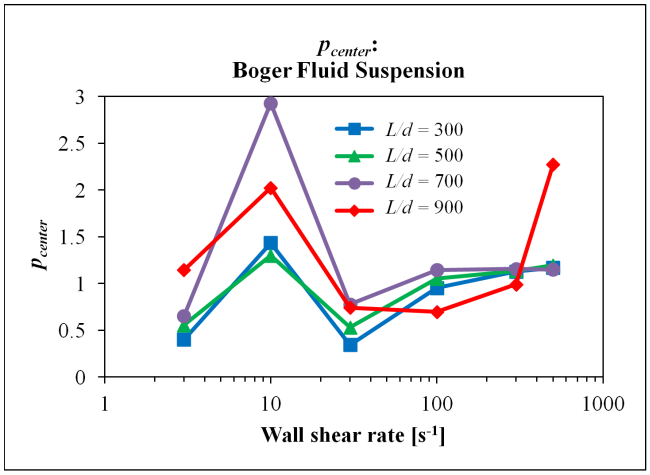

Figure 4.17 Center peak analysis for the Boger fluid suspension.

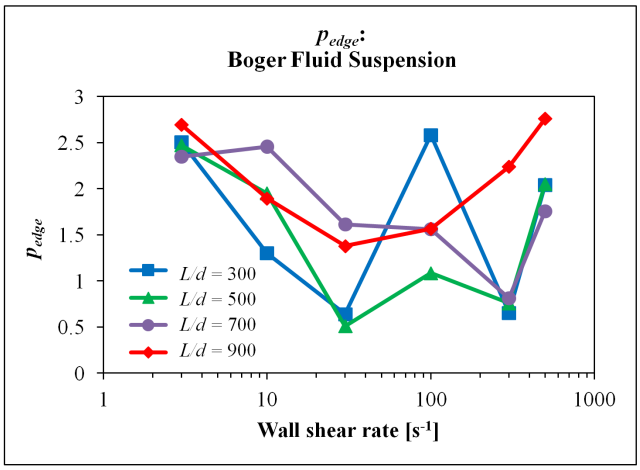

Figure 4.18 Edge peak analysis for the Boger fluid suspension.

4.4 Discussion

Now that the general behavior each of these three suspending fluids has been discussed, a more detailed analysis of these observations is appropriate. By comparing the trends in these suspensions with the rheological properties of the suspending fluids, we can gain some insight regarding the underlying driving forces for the various phenomena that are observed. The first conclusion to be made relates to profile focusing. Although the Boger fluid data are quite puzzling in every other regard, the lack of profile focusing demonstrates quite clearly that normal forces do not drive this behavior. If normal forces alone were the source of profile focusing, the Boger fluid suspensions should have exhibited this feature more strongly than either of the two other fluids, since the Boger fluid has the largest N_1 of all the fluids investigated. Therefore, profile focusing must be driven by shear thinning. This hypothesis is consistent with the observations from the two Ultem®-based fluids discussed so far, in that the Ultem®-Luvitec® fluid is the more strongly shear-thinning of the two, and exhibits more pronounced focusing.

Having determined that profile focusing can be attributed to shear thinning, it naturally follows that the formation of center peaks (i.e., particle accumulation at the centerline) is likely also caused by shear thinning. The basis for this conclusion is that both of these features—profile focusing and particle accumulation at the channel centerline—involve migration of particles toward the channel center, so it seems probable that they are caused by the same underlying driving force.

The next logical conclusion is that migration toward the channel walls is driven by a different rheological property than the one causing inward migration. Therefore, migration toward the walls is likely attributed not to shear thinning, but to normal forces. The first piece of evidence supporting this hypothesis is the fact that the Boger fluid data, though admittedly noisy and scattered, seem to suggest that migration toward the walls is the preferred behavior of particles in this fluid. Many of the Boger fluid profiles exhibit peaks at the channel walls; on the other hand, these profiles do not exhibit the dramatic center peaks found in the Ultem®-Luvitec® results, nor do they exhibit any profile focusing. Since the Boger fluid possesses very large normal forces, and virtually no shear thinning, this supports the hypothesis that normal forces are the source of migration toward the walls.

Another important clue in support of this conclusion is found in the Ultem® 23.5% results. As shown in the flow curve (see Figure 4.4), N_1 becomes detectable for this fluid around a shear rate of 100 s^{-1}, which is roughly in agreement with the fact that edge peaks begin forming at shear rates above 100 s^{-1} (see Figure 4.14). It is also around 100 s^{-1} that the slight profile-focusing trend observed at low shear rates begins to reverse (Figure

4.12), suggesting that around 100 s^{-1} the appearance of normal forces begins to counteract shear thinning, which was driving particles to the center at lower flow rates.

Although the dominant feature in the Ultem®-Luvitec® suspension is migration toward the center due to shear thinning, we can also discern some subtler effects of normal forces in these data. The Ultem®-Luvitec® fluid begins to exhibit detectable normal forces around 10 s^{-1}. In this same range, the effect of profile focusing diminishes and particles begin occupying larger fractions of the channel (Figure 4.7). This is also the range of shear rates in which the p_{edge} curve displays a slight increase (Figure 4.9). According to our hypothesis, both of these effects are caused by normal forces, which seek to move particles toward the walls, effectively competing with the inward migration caused by shear thinning.

4.4.1 Ultem® 30% Suspension

To further test these hypotheses, and to investigate migration in a solution closer in composition to an actual fiber spinning dope, we also tested a suspension using a more concentrated 30 wt.% Ultem® solution as the continuous phase (see Figure 4.4). Based on the observations described above, this fluid would be expected to behave similarly to the Ultem® 23.5% suspension, in the sense that both fluids exhibit limited shear thinning before the onset of normal forces. However, because N_1 appears a decade earlier for the 30% solution than the 23.5%, we would expect that migration to the walls should also occur at lower shear rates. We would also expect some slight profile focusing at low shear rates, as was observed for the 23.5% suspension, with the effect becoming slightly

more pronounced with increasing shear rates, and then diminishing again; the effect is projected to be strongest at a lower shear rate than for the 23.5% solution.

The Ultem® 30% suspension was prepared and measured using shear rates of 10, 30, and 100 s^{-1}. Due to the high viscosity and associated pressure drops, the 100 s^{-1} experiment was conducted in a 75-mm capillary. Since results could not be obtained for L/d = 900 at all conditions, we will compare the Ultem® 30% findings to the previous results for L/d = 700. The first comparison is presented in Figure 4.19(a), which shows the profile focusing analysis for the 23.5% and 30% Ultem® fluids. As predicted, the Ultem® 30% suspension does exhibit focusing behavior similar to the Ultem® 23.5% suspension. Also in agreement with our hypothesis is the fact that the focusing exhibits an upturn at a lower shear rate than the Ultem® 23.5% suspension.

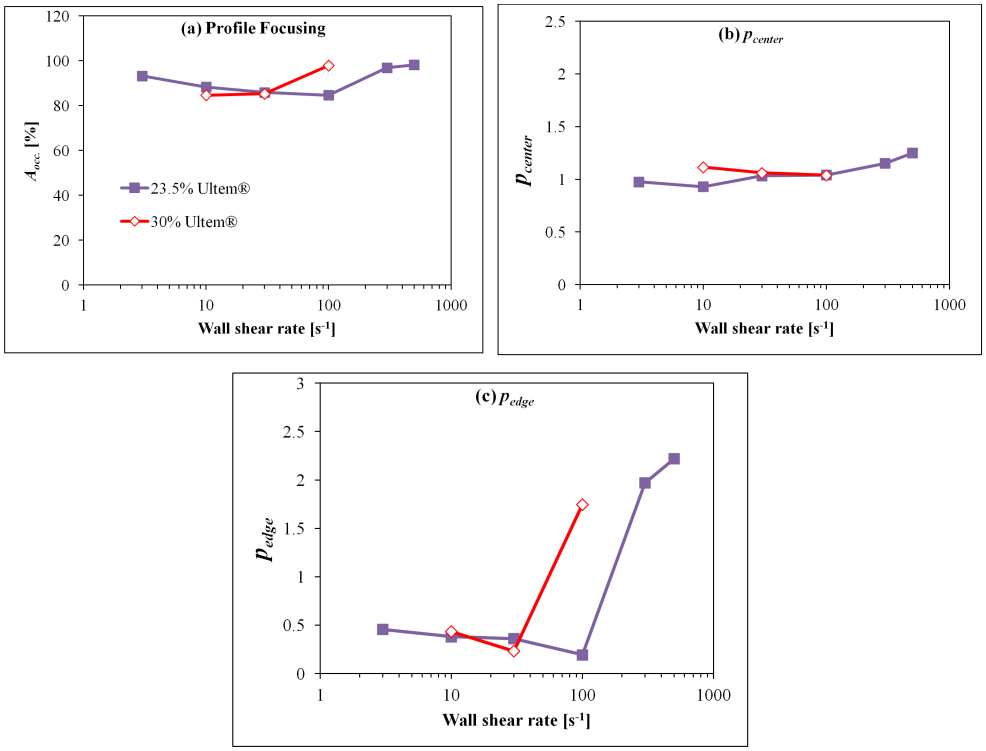

Figure 4.19 Comparison of the 23.5% and 30% Ultem® suspensions in terms of (a) profile focusing, (b) p_{center}, and (c) p_{edge}.

Figure 4.19(b) shows p_{center} for the two Ultem® fluids. As predicted, the Ultem® 30% suspension behaves similarly to the Ultem® 23.5% system in this regard, exhibiting no significant accumulation of particles in the channel center. The predictions are also correct regarding migration to the walls. As shown in Figure 4.19(c), the 30% suspension exhibits migration to the channel walls at lower shear rates than the 23.5% suspension due to the earlier onset of normal forces in the continuous phase.

It is interesting to note that the wall migration effect seems to depend on an absolute value of N_1, rather than on the relative magnitude of normal and shear forces. That is, wall migration is observed at similar absolute values of N_1 for the 23.5% and 30% Ultem® suspensions, even though shear forces are much higher for the 30% solution due to the larger viscosity (by almost an order of magnitude). One might have predicted that the larger viscosity of the 30% solution would impede the lateral motion of the particles, but these results suggest that normal stresses act nearly independently of shear stress.

At this point, we should compare these conclusions to results from previous studies involving shear-induced migration. Our findings are in agreement with the results published by Tehrani, who also found that migration to the center was attributed to shear thinning [73]. Our observations differ slightly with regards to the effect of normal forces, though. Tehrani found that normal forces induced only very slight migration to the walls, and sometimes no migration occurred at all. This discrepancy is likely due to the choice of materials used in that study, compared to the ones used here. To achieve large normal forces, Tehrani used cross-linked polymer solutions. The networks formed due to cross-linking can result in very different rheological properties compared to fluids whose normal forces are created by individual polymer chains. Cross-linked fluids can exhibit

gel-like and solid-like characteristics, whereas un-cross-linked polymer solutions exhibit elasticity, but behave primarily as liquids. Some of the fluids in the study by Tehrani did, in fact, exhibit solid-like properties. Likely due to the cross-linking, these solutions displayed strong wall slip and a plug-like velocity profile. The resulting lack of a shear gradient across much of the channel could be the reason that their fluids did not exhibit significant migration, despite the large normal forces.

Our findings can also be compared to those of D'Avino and co-workers, who found a bistability scenario for particles flowing in a microfluidic channel using both experiments and simulations [106]. In some ways, the results are in agreement. For example, we both find that migration in both directions can occur in shear-thinning polymer solutions. Our conclusions about the specific role of shear thinning, though, are quite different. D'Avino et al. concluded that stronger shear thinning promoted migration toward the channel walls. However, they did not attempt to decouple the role of normal forces from shear thinning, and they did not report measurements of N_1 for the solutions in their experiments. Therefore, the migration they attribute to shear thinning could instead be an effect of the larger normal forces that often accompany strong shear thinning. Another important distinction between our experiments and their work is the ratio between particle size and channel dimensions. Their study focused on relatively confined conditions—particle radii approximately one-tenth the channel radius. In our case, the particles were much smaller compared to the channel height (particle diameter approximately 3% of the channel size). One consequence of stronger confinement is that shear conditions in channel flow vary *more* from one side of the particle to another,

creating stronger imbalances. For these reasons, strict comparisons between their findings and the ones presented in this chapter should perhaps be avoided.

4.4.2 String Formation

Although shear-induced structures such as the strings shown in Figure 4.11 were not the focus of this study, they merit a brief discussion. Chapter 3 of this thesis investigated shear-induced structure formation in suspensions of silica in Ultem®-NMP-ethanol solutions. In those studies, which involved 500-nm particles, a vorticity orientation of short particle strings was found. The migration experiments described in this chapter used larger particles—roughly 3 μm in diameter—and flow-oriented strings were observed. The conditions are admittedly different (e.g., slightly different fluid compositions, volume fractions, and flow conditions), so direct comparisons between the two sets of experiments are not merited. Nevertheless, this observation is generally in agreement with the findings of Pasquino et al., who found that vorticity oriented structures formed only for small particles, while larger particles tended to form flow-oriented strings [68]. Also, no string formation is observed for the Boger fluid studied here, even for the cases in which particles migrated to the walls. This is in agreement with previous studies that suggest that the formation of flow-oriented strings requires a shear-thinning fluid [67], and in agreement with the findings in Chapter 3 of this thesis, where it is shown that shear thinning is required for structure formation.

4.4.3 A Note Regarding the Boger Fluid Observations

We do not completely understand the behavior that is seen in the Boger fluid experiments, particularly the high noise level. However, highly elastic fluids (such as Boger fluids and other polymer solutions) are known to exhibit flow instabilities, such as shear banding [42, 123, 124]. Shear banding is an effect that occurs in fluids with long relaxation times. When shear or stress is applied to such fluids, they can undergo structural rearrangements that result in regions of different viscosities, which in turns leads to ill-defined velocity profiles [125]. The fluid separates into "bands" that flow with different velocities. Using a camera to record the flow of a particle-free Boger fluid through the capillaries used in these experiments, we did observe a peculiar velocity profile. Figure 4.20 shows the path lines obtained from a sequence of images during this recording. The streaks (which are caused by dust particles and/or small air bubbles in the fluid) near the advancing front of the meniscus are not at all parallel to the flow direction, illustrating the non-unidirectional nature of the flow.

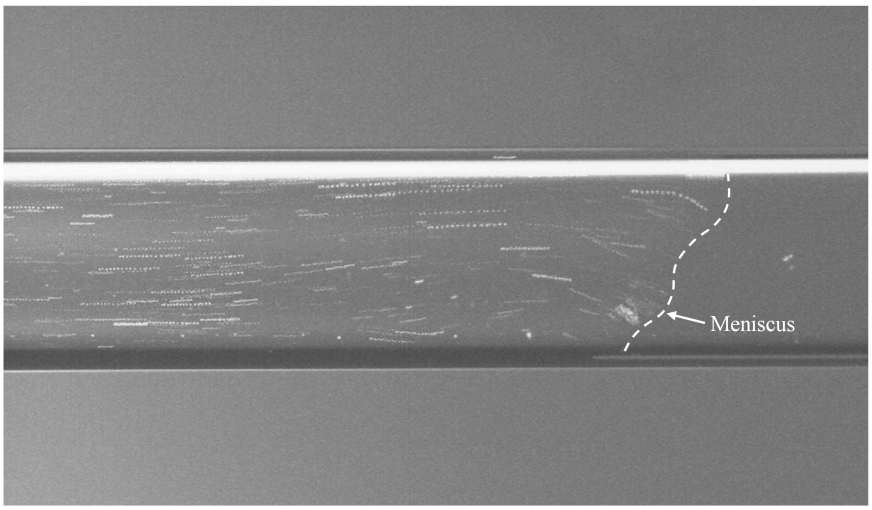

Figure 4.20 Pathline analysis of a Boger fluid flowing through a capillary; the bent streamlines at the advancing front of the fluid illustrate the secondary recirculation flows in this region.

Even though we do not fully understand this behavior, it suggests that shear banding, or some type of fracture or instability, occurs in this material. As a consequence, the scattered results observed for the Boger fluid suspension could be due to the lack of a well-defined velocity profile—and thus, shear profile—within the capillary.

4.4.4 Implications for Mixed Matrix Fiber Spinning

These results have several implications for mixed matrix fiber spinning, and other industrial processes involving particles dispersed in non-Newtonian media. First, let us discuss the effect of migration to the center. If the Ultem®-Luvitec® fluid used in this study were being used for fiber spinning, for example, it is unlikely that the skin layer would contain any molecular sieves whatsoever. Since inward migration occurs even at low shear rates, shear in upstream channels would likely cause migration away from the walls, leaving particle-free regions at the edges. At the large shear rates found at the

spinneret exit, it is possible that normal forces could dominate over shear-thinning effects, causing some migration toward the walls. However, this may not be sufficient (either in the magnitude of the resulting normal forces, or in the total strain) to counteract the depletion that occurred upstream.

A note about molecular weight is warranted. The characteristics that cause inward migration in the Ultem®-Luvitec® fluid are due to the high molecular weight of the Luvitec®, which is much greater than the molecular weights that are typically involved in fiber spinning. However, many promising new membranes are being formulated using customized polymers that are tailored specifically for a particular separation. These polymers are often produced in-house, with relatively poor control of the molecular weight distribution. The resulting flow properties of these homemade polymers can vary significantly due to polydispersity. To ensure that undesired migration effects will not occur, polymers should undergo careful rheological characterization before being used for mixed matrix spinning; materials exhibiting pronounced, early-onset shear thinning, such as that exhibited by the Ultem®-Luvitec® fluid, should be avoided.

The effect of migration to the walls should also be discussed. This is, at first glance, the desirable scenario for fiber spinning. However, it is not entirely clear from the results discussed thus far whether the particles that migrate to the wall are stuck there permanently. If they are, then migration toward the walls would actually be an undesirable scenario, since particles would accumulate on the inner spinneret surfaces, rather than exiting the spinneret in the skin layer of the fiber.

An attempt was made to address this issue using extrusion experiments combined with phase separation. In the test, the Ultem® 23.5% suspension was extruded using a

shear rate of 500 s^{-1}, to see whether larger particle concentrations could be observed near the perimeter of the solidified fiber. Another extrusion using a shear rate of 3 s^{-1} was used as a control experiment. The cross sections and outer surfaces of the fibers were then examined using a confocal microscope. Figure 4.21 shows the results of these experiments. The large difference in shear rate caused the extruded fibers to have different morphologies. The 500 s^{-1} fiber exhibited die swell, causing it to be thicker than the 3 s^{-1} fiber, which essentially retained the shape and dimensions of the channel. These different morphologies make it challenging to compare the particle distributions in the fiber cross sections. Images of the outer surfaces of the fibers, however, provide more useful information. The outer surface of the 500 s^{-1} extrusion exhibited very distinct strings of particles. The strings that were discussed in Section 4.3.2.2 and shown in Figure 4.11 were only ever observed at the walls of the channels. Therefore, their presence at the surface of the extruded fiber proves that the particles do not get permanently stuck at the channel walls. No strings were observed on the surface of the 3 s^{-1} fiber.

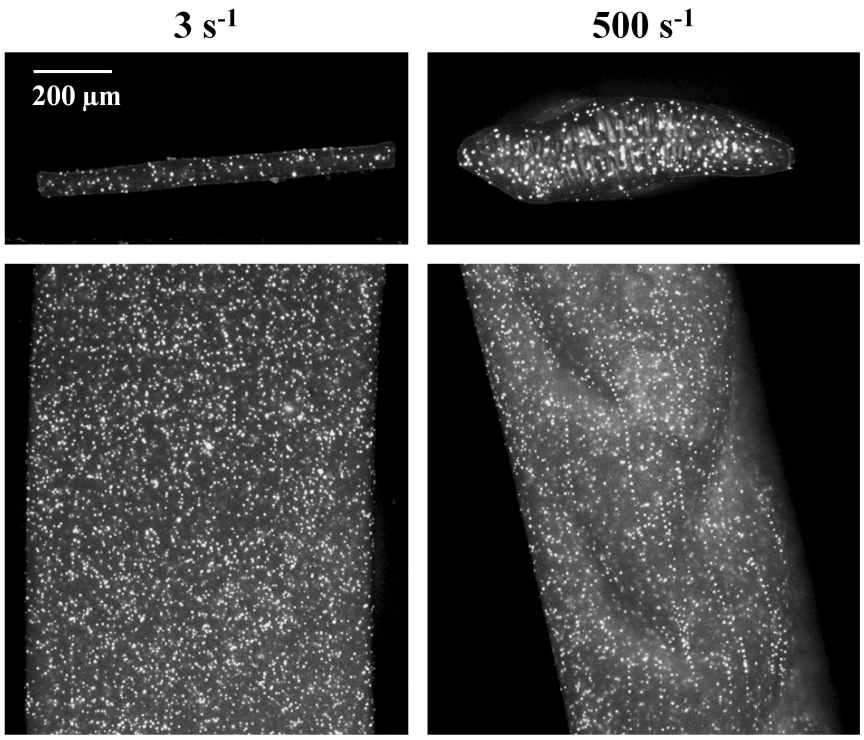

Figure 4.21 Confocal images showing fibers extruded and phase separated using shear rates of 3 and 500 s^{-1}; the upper images show the fiber cross sections, while the lower images show the outer surfaces of the fibers.

4.5 Conclusions

In summary, cross-stream particle migration was investigated using silica particles dispersed in fluids with varying degrees of shear thinning and normal force characteristics. Experiments consisted of pressure-driven flow of the suspensions through rectangular capillaries across a wide range of shear rates. The resulting particle distributions along the shear gradient direction were quantified using confocal microscopy. The results show that shear can cause non-uniform particle distributions to develop. Non-uniformities were quantified in terms of several different features that were observed. In some cases, particles migrated away from the walls, resulting in a net reduction in the fraction of the total cross-sectional area of the channel that was occupied

by particles. This effect, termed profile focusing, occurred to some degree in all the fluids investigated except for the Boger fluid, and could therefore be attributed to shear thinning. Suspending fluids with stronger shear thinning gave rise to more pronounced profile focusing. Another indicator of inward migration was a distinct increase in particle concentration at the channel centerline, an effect that was also attributed to shear thinning.

In some cases, the opposite effect was observed. That is, migration to the channel walls occurred, which could be attributed to normal forces. In all the fluids studied in this investigation, except the Boger fluid, the effects of *both* shear thinning and normal forces can be seen simultaneously. However, shear-thinning effects dominate in the Ultem®-Luvitec® fluid, which displays an early onset of shear thinning relative to the appearance of normal forces. In the 23.5% and 30% Ultem® suspensions, normal force effects dominate due to the relatively late onset of shear thinning in comparison to the appearance of normal forces. Based on the fact that two solutions of very different viscosities induced wall migration at roughly the same value of N_1, we can conclude that the onset of wall migration corresponds more closely to an absolute magnitude of N_1 rather than the ratio of normal to shear stresses. These results help to clarify some aspects of shear-induced migration that were not previously well understood.

CHAPTER 5

CONCLUSIONS AND RECOMMENDATIONS

In this thesis, several shear-related phenomena involving concentrated polymer solutions were explored, both with and without suspended colloidal particles. The findings have implications for hollow fiber membrane spinning, and for many other applications involving polymer solutions and suspensions of particles in viscoelastic media. The key conclusions are listed below.

- Shear can cause liquid-liquid demixing in polymeric membrane dopes.
- Shear-induced demixing in dope solutions depends not only on the instantaneous shear conditions, but also on the shear history of the solution.
- Solvent-rich droplets formed via shear-induced demixing promote macrovoid formation during solvent-induced phase separation.
- Sub-micron particles in concentrated polymer solutions can form aggregated, vorticity-oriented structures when shear rates in the shear-thinning regime are applied.
- Formation of the aggregated vorticity structures requires two fluid characteristics: shear thinning, which facilitates aggregation, and normal forces, which orient the aggregates.
- The aggregated, oriented structures are reversible; samples containing such structures return to isotropy under low-shear conditions via a two-step process in which aggregates first reorient into the flow direction and are then broken apart by shear.

- Particles suspended in polymer solutions can exhibit migration either toward the walls or toward the centerline in pressure-driven flow through a capillary.
- The rheological characteristics of the suspending fluid determine whether migration will occur toward the walls or the center; shear thinning promotes migration to the center, while normal forces cause migration to the walls.
- Particles that migrate toward the walls do not get immobilized at the wall; rather, they continue to flow with the surrounding fluid, ultimately exiting the channel.

These conclusions will be discussed in more detail in the following sections, along with recommendations for future research that could build upon these findings.

5.1 Polymer Effects: Shear History & Shear-Induced Demixing

Chapter 2 described experiments showing that shear can cause liquid-liquid demixing in concentrated polymeric solutions such as those used to spin hollow fiber membranes. Specifically, the study explored how shear history affects this demixing process, and whether demixing has any effect on macrovoid formation.

This research included two series of experiments. The first series focused on *in situ* measurements of the shear-induced demixing process. In these experiments, the initial shear step applied to a solution was varied and then light scattering (shear-SALS) was used to monitor the demixing behavior during a subsequent shear process. This two-part scheme was designed to mimic the flow conditions during fiber spinning, which include low-shear rates in upstream channels, followed by high shear rates at the spinneret exit. Understanding the effects of shear history is useful, since the conditions upstream can easily be modified with simple equipment adjustments such as tubing diameter changes,

while those at the spinneret exit are typically constrained by the geometry of the spinneret and the desired flow rate. The results showed that very subtle changes in shear history can affect the demixing observed during the subsequent high-shear process, both in terms of the shear rate at which demixing will occur, and in the characteristic length scales of the resulting demixed microstructure.

A second series of experiments was performed with the goal of determining whether shear history and shear-induced demixing influence macrovoid formation. These experiments employed a two-part scheme similar to the one described above; the initial shear step was varied, followed by a combined extrusion/phase separation step that was identical in all experiments. The resulting fibers were then analyzed using SEM to determine the number of macrovoids they contained. Shear history did, in fact, affect the number of macrovoids that was observed in the fibers. A comparison of the results obtained from the shear-SALS and extrusion experiments revealed a strong link between shear-induced demixing and macrovoid formation. This suggests that macrovoids form due to the presence of solvent-rich regions that are created during shear-induced demixing, a mechanism that has not previously been considered.

These results have some significant implications for fiber spinning. The fact that demixing and macrovoid formation were found to depend so strongly on shear history is both encouraging and somewhat alarming. The shear rates used for the initial shear step in these experiments are very similar to those commonly found in the upstream channels of a laboratory spinning operation. This suggests that macrovoids can potentially be suppressed using simple modifications to upstream flow channels (tubing, etc.) rather than adjusting key parameters such as the spinneret geometry or dope flow rate.

However, the results should also serve as a note of caution regarding equipment design—that is, when scaling up a laboratory process or constructing additional production lines to increase capacity, the importance of upstream equipment should not be overlooked.

These findings also raise some interesting questions that should be addressed in future research. For example, it is not clear from these results why demixing and macrovoid formation are preferred at some shear rates rather than others. One recommendation that could help answer this question is to investigate demixing using solutions of different concentration and solvent quality or polymers of different molecular weight. This could provide a better characterization of the conditions that are necessary to induce demixing, and potentially allow for more universal spinning guidelines.

Another recommendation regarding this topic is to test whether these results, which were obtained using syringe extrusions, also apply in an actual spinning setup. A relatively simple test to perform would be to spin fibers using a flow rate and upstream tubing size such that the wall shear rate in the tubing is close to 3.7 s^{-1}. According to the results described in Chapter 2, these fibers would be expected to contain many macrovoids. Then, the tubing would be changed to a slightly smaller size, so that the same dope flow rate would result in a wall shear rate higher than 3.7 s^{-1}, perhaps 6.0 s^{-1}; these fibers would be expected to contain fewer macrovoids.

5.2 Particle Effects: Shear-Induced Aggregation & Orientation

In Chapter 3, shear-induced particle microstructure was investigated using shear-SALS to study suspensions of silica particles in concentrated Ultem® solutions. Shear rates in the shear-thinning regime of the polymer solution were found to cause the

formation of vorticity-oriented particle aggregates. Although this type of structure has been seen in the past, observations of vorticity structures are somewhat rare compared to the more commonly studied flow-oriented strings. The Ultem®-silica suspension proved to be a useful system for investigating some fundamental features of vorticity structures.

First, we characterized the conditions required to form the structures. Shear rates well below the shear-thinning transition did not result in any structure, even for large amounts of total strain. For shear rates in the shear-thinning regime, vorticity structures were observed. Furthermore, larger shear rates produced more pronounced structures, even for the same total deformation. This illustrates that the extent of structure formation depends on *how* non-Newtonian the suspending fluid is under a given set of shear conditions. That is, larger shear rates generally induce a greater degree of shear thinning and normal forces in the continuous phase, and therefore result in more distinctive structures. An experiment measuring the microstructural evolution of particles in a Boger fluid revealed that shear thinning is a crucial component in the formation of vorticity structures. Based on this finding, it was concluded that the mechanism for structure formation involves two separate rheological features: shear thinning causes particle aggregation, and normal forces are responsible for the orientation of the aggregates.

The vorticity structures exhibited an interesting recovery behavior when the shear rate was reduced to values in the Newtonian regime. The aggregates first rotated 90° toward a flow orientation, and were subsequently broken apart by shear forces. The relative dynamics of these two steps were analyzed, and it was found that the orientation change occurred quickly compared to the breakup of aggregates. The measured viscosity of the suspension was strongly correlated with the breakup of aggregates, while the orientation

change did not affect the viscosity. The samples remained intact if no shear was applied, which is an important distinction from some past observations.

Although this work was initially motivated by mixed matrix fiber spinning, the findings have more relevance in the larger rheology community, where a fundamental understanding of shear-induced structure in non-Newtonian media is desired. Still, there are a few comments to be made with regards to fiber spinning. First, it is possible that shear-induced aggregation could occur during fiber spinning, although we are not aware of any reports of this problem. Likely, the total strain associated with fiber spinning is small enough that aggregation is minimal. The orientation aspect of the research, however, could serve as inspiration for future studies involving the use of high aspect ratio sieves, which can provide additional selectivity benefits if they can be aligned during spinning. Recently developed high aspect ratio zeolites have sparked a renewed interest in this route [63], so a rheological investigation of these materials and the associated orientation effects would be worthwhile.

From a rheological perspective, these results enhance our understanding of an intriguing phenomenon. They also help us better understand some unexplained aspects of past observations of vorticity structures. First, the results show that the formation of vorticity structures requires shear thinning. This same conclusion has been made in previous reports regarding flow-oriented strings, but the requirements for vorticity orientation had not previously been investigated [67]. Also, some previous studies found that vorticity orientation occurred at shear rates below the onset of shear thinning [68]. Our results show, however, that this structure does not form at shear rates well below the onset of shear thinning. In fact, pre-formed structures were found to disappear when the

shear rate was lowered to a Newtonian rate. However, at shear rates that were only *slightly* below the shear-thinning regime, some vorticity orientation was observed. This indicates that local shear rates between particles, which by definition exceed the nominal shear rate, can induce non-Newtonian characteristics in the fluid, resulting in structure formation. Past reports of vorticity-oriented structures at seemingly Newtonian shear rates [68] can therefore likely be explained in the same way; that is, even though the bulk shear rate was in the Newtonian regime, particles experienced larger shear rates, causing vorticity structures.

An interesting question raised by this research relates to particle size. There seems to be a transition from vorticity orientation at small particle sizes, to flow-oriented structures for larger particles. This transition, according to our results and those of other researchers, seems to occur around 0.5-1 μm. It would be interesting to see whether experiments similar to those described in Chapter 3, but with slightly larger particles, would reveal flow-oriented structures. This would also provide an opportunity to explore another unanswered question regarding shear-induced particle structure, which is why flow-oriented structures sometimes occur in the bulk of the sample, while in other cases they form only at the shearing surfaces.

A final recommendation regarding this topic involves using rod-like particles to isolate the effects of aggregation and orientation. According to our hypothesis regarding vorticity-oriented structures, shear thinning caused the aggregation, while normal forces induced the orientation. If this is true, then a Boger fluid containing rod-like particles should show stronger orientation effects than, for example, an Ultem® solution.

5.3 Particle Effects: Shear-Induced Migration

Chapter 4 presented research surrounding a second particle-related topic: migration. This work investigated the effect of viscoelastic media on the distribution of dispersed particles in the presence of a shear rate gradient. This research is important both for fiber spinning, in which the distribution of molecular sieves in the sheath layer can affect separation performance, and for many other applications involving suspensions of particles in viscoelastic media.

To study migration, several suspensions were prepared using fluids with varying degrees of shear thinning and normal forces. The suspensions were then studied using flow through narrow rectangular capillaries over a wide range of shear rates. Confocal microscopy was used to quantify the resulting particle distributions within the capillaries. The results show that polymer solutions can induce migration both toward the walls and the center of the channel. By comparing the observed particle distributions and the rheological characteristics of the fluid, it was concluded that shear thinning promotes migration to the center, while normal forces tend to induce migration toward the channel walls.

The Ultem®-Luvitec® fluid exhibited the earliest onset of shear thinning (due to the high molecular weight of the Luvitec®); in this sample, inward migration dominated. At low shear rates, particles migrated away from the walls, reducing the total portion of the channel occupied by particles. At higher shear rates, migration to the center became so strong that distinct peaks in the concentration profile were observed at the channel centerline. The total occupied fraction of the channel, however, did not continue to decline over the entire range of shear rates. Rather, the appearance of normal forces

caused particles to move back toward the walls slightly, resulting in larger occupied portions of the channel cross section. This illustrates the fact that both driving forces can act simultaneously in a single material.

For the Ultem® solutions without the high molecular weight Luvitec® additive, migration to the walls was observed, concurrent with the appearance of measurable normal forces as determined by flow curve measurements. Two Ultem® solutions of differing polymer concentrations exhibited wall migration at similar values of N_1 despite large difference in viscosities, suggesting that migration depends more on an absolute magnitude of normal stresses, rather than the relative values of normal and shear stresses. This indicates that the increased viscosity of the higher concentration solution did not significantly hinder the lateral motion of the particles.

The Boger fluid exhibited some interesting distinctions from the other fluids that were investigated. First, it lacked any profile focusing whatsoever—particles could be found across the entire channel at all flow rates that were explored. Secondly, no trends could be observed regarding migration toward the center or walls. This was attributed to an ill-defined flow profile within the capillary, likely due to flow instabilities that can occur in highly elastic fluids.

These findings can be translated into several recommendations for mixed matrix membrane spinning. First, inward migration effects should be addressed. Migration to the channel center is extremely undesirable in spinning, and our results show that migration due to shear-thinning effects could cause extreme depletion in the skin layer. Therefore, it is recommended that polymer solutions being considered for use in mixed matrix spinning undergo careful rheological characterization to ensure that the solutions do not

exhibit shear thinning at shear rates significantly below the appearance of measurable normal stresses.

Next, wall migration will be discussed. Migration to the channel walls was observed in Ultem® solutions not containing any ultra-high molecular weight additives, suggesting that migration could potentially be used to increase the concentration of molecular sieves in the skin layer of composite fibers. This raises the question: why has this migration effect not already been observed in mixed matrix spinning? One possibility is that spinnerets, as currently designed, do not provide sufficient strain at the large shear rates required for wall migration. In this case, lengthening the final extrusion channel would achieve the desired effect. According to the results presented in Section 4.2.2.2, wall migration effects can be observed at L/d = 300, and they become increasingly pronounced at even larger deformations. Typically, the final channel of a spinneret has L/d on the order of 10, so achieving migration could require a fairly substantial lengthening of this channel. The sheath compartment of a spinneret typically possesses a very short exit channel, on the order of 0.05 inches. Lengthening this channel to 1-2 inches could provide significant enhancement of the skin layer sieve concentration. Because the design and production of a new spinneret would require a significant investment, an economic analysis should be conducted to determine whether the benefits of increasing the skin layer concentration via migration outweigh the cost of simply increasing the overall sieve concentration of the sheath dope.

The final recommendation of this thesis relates to the string structures observed at the channel walls in the Ultem® suspensions. There are several interesting aspects of these observations that warrant further investigation. First of all, the structures reported in

Chapter 4 contain much larger spacing between particles compared to past reports in the literature on flow-oriented strings. Performing further experiments using different particle sizes, for example, could help explain this phenomenon. Secondly, these structures are typically studied using simple shear geometries such as parallel plates, but have not been studied extensively in pressure-driven flow. The primary purpose for studying suspensions in these channels was to investigate particle migration, but the experimental setup and confocal imaging technique could also provide an interesting and useful route to explore shear-induced particle alignment.

REFERENCES

[1] Bernardo, P., E. Drioli, and G. Golemme, Membrane gas separation: A review/state of the art. *Industrial & Engineering Chemistry Research*, 2009. **48**(10): 4638-4663.

[2] Wallace, D.W., C. Staudt-Bickel, and W.J. Koros, Efficient development of effective hollow fiber membranes for gas separations from novel polymers. *Journal of Membrane Science*, 2006. **278**(1-2): 92-104.

[3] Koros, W.J. and R.P. Lively, Water and beyond: Expanding the spectrum of large−scale energy efficient separation processes. *AIChE Journal*, 2012. **58**(9): 2624-2633.

[4] Koros, W.J., Evolving beyond the thermal age of separation processes: Membranes can lead the way. *AIChE Journal*, 2004. **50**(10): 2326-2334.

[5] Clausi, D.T. and W.J. Koros, Formation of defect-free polyimide hollow fiber membranes for gas separations. *Journal of Membrane Science*, 2000. **167**(1): 79-89.

[6] Pinnau, I., J. Wind, and K.V. Peinemann, Ultrathin multicomponent poly(ether sulfone) membranes for gas separation made by dry/wet phase inversion. *Industrial & Engineering Chemistry Research*, 1990. **29**(10): 2028-2032.

[7] Loeb, S. and S. Sourirajan, *Sea water demineralization by means of an osmotic membrane*. 1962: ACS Publications.

[8] Larson, R.G., *The Structure and Rheology of Complex Fluids*. 1999, New York: Oxford University Press.

[9] Husain, S. and W.J. Koros, Mixed matrix hollow fiber membranes made with modified HSSZ-13 zeolite in polyetherimide polymer matrix for gas separation. *Journal of Membrane Science*, 2007. **288**(1-2): 195-207.

[10] Dai, Y., J. Johnson, O. Karvan, D.S. Sholl, and W. Koros, Ultem®/ZIF-8 mixed matrix hollow fiber membranes for CO2/N2 separations. *Journal of Membrane Science*, 2012. **401-402**: 76-82.

[11] Das, M., J.D. Perry, and W.J. Koros, Gas-transport-property performance of hybrid carbon molecular sieve-polymer materials. *Industrial & Engineering Chemistry Research*, 2010. **49**(19): 9310-9321.

[12] Moore, T.T., R. Mahajan, D.Q. Vu, and W.J. Koros, Hybrid membrane materials comprising organic polymers with rigid dispersed phases. *AIChE Journal*, 2004. **50**(2): 311-321.

[13] Ordonez, M., C. Josephine, K.J. Balkus Jr, J.P. Ferraris, and I.H. Musselman, Molecular sieving realized with ZIF-8/Matrimid mixed-matrix membranes. *Journal of Membrane Science*, 2010. **361**(1-2): 28-37.

[14] Zhang, Y.F., K.J. Balkus, I.H. Musselman, and J.P. Ferraris, Mixed-matrix membranes composed of Matrimid® and mesoporous ZSM-5 nanoparticles. *Journal of Membrane Science*, 2008. **325**(1): 28-39.

[15] Perez, E.V., K.J. Balkus, J.P. Ferraris, and I.H. Musselman, Mixed-matrix membranes containing MOF-5 for gas separations. *Journal of Membrane Science*, 2009. **328**(1): 165-173.

[16] Batchelor, G., The effect of Brownian motion on the bulk stress in a suspension of spherical particles. *Journal of Fluid Mechanics*, 1977. **83**(01): 97-117.

[17] Kosinski, L. and J. Caruthers, Rheological properties of poly (dimethylsiloxane) filled with fumed silica: II. Stress relaxation and stress growth. *Journal of Non-Newtonian Fluid Mechanics*, 1985. **17**(1): 69-89.

[18] Ziegelbaur, R. and J. Caruthers, Rheological properties of poly (dimethylsiloxane) filled with fumed silica: I. Hysteresis behaviour. *Journal of Non-Newtonian Fluid Mechanics*, 1985. **17**(1): 45-68.

[19] Michele, J., R. Patzold, and R. Donis, Alignment and aggregation effects in suspensions of spheres in non-Newtonian media. *Rheologica Acta*, 1977. **16**(3): 317-321.

[20] Lively, R.P., M.E. Dose, L. Xu, J.T. Vaughn, J. Johnson, J.A. Thompson, K. Zhang, M.E. Lydon, J.-S. Lee, L. Liu, Z. Hu, O. Karvan, M.J. Realff, and W.J. Koros, A high-flux polyimide hollow fiber membrane to minimize footprint and energy penalty in CO2 recovery from flue gas. *Journal of Membrane Science*, 2012. **423-424**: 302-313.

[21] McKelvey, S.A. and W.J. Koros, Phase separation, vitrification, and the manifestation of macrovoids in polymeric asymmetric membranes. *Journal of Membrane Science*, 1996. **112**(1): 29-39.

[22] Husain, S. and W.J. Koros, Macrovoids in hybrid organic/inorganic hollow fiber membranes. *Industrial & Engineering Chemistry Research*, 2009. **48**(5): 2372-2379.

[23] Wang, K.Y., D. Fei Li, T.S. Chung, and S. Bor Chen, The observation of elongation dependent macrovoid evolution in single-and dual-layer asymmetric hollow fiber membranes. *Chemical Engineering Science*, 2004. **59**(21): 4657-4660.

[24] Ekiner, O. and G. Vassilatos, Polyaramide hollow fibers for hydrogen/methane separation—spinning and properties. *Journal of Membrane Science*, 1990. **53**(3): 259-273.

[25] Frommer, M.A., R. Matz, and U. Rosenthal, Mechanism of formation of reverse osmosis membranes - precipitation of cellulose acetate membranes in aqueous solutions. *Industrial & Engineering Chemistry Product Research and Development*, 1971. **10**(2): 193-196.

[26] Strathmann, H., K. Kock, P. Amar, and R. Baker, The formation mechanism of asymmetric membranes. *Desalination*, 1975. **16**(2): 179-203.

[27] Saljoughi, E., M. Sadrzadeh, and T. Mohammadi, Effect of preparation variables on morphology and pure water permeation flux through asymmetric cellulose acetate membranes. *Journal of Membrane Science*, 2009. **326**(2): 627-634.

[28] Saljoughi, E., M. Amirilargani, and T. Mohammadi, Effect of poly (vinyl pyrrolidone) concentration and coagulation bath temperature on the morphology, permeability, and thermal stability of asymmetric cellulose acetate membranes. *Journal of Applied Polymer Science*, 2009. **111**(5): 2537-2544.

[29] Kesting, R., A. Fritzsche, M. Murphy, C. Cruse, A. Handermann, R. Malon, and M. Moore, The second-generation polysulfone gas-separation membrane. I. The use of Lewis acid:base complexes as transient templates to increase free volume. *Journal of Applied Polymer Science*, 1990. **40**(9-10): 1557-1574.

[30] Bloch, R. and M. Frommer, The mechanism for formation of "skinned" membranes I. Structure and properties of membranes cast from binary solutions. *Desalination*, 1970. **7**(2): 259-264.

[31] Cabasso, I., E. Klein, and J.K. Smith, Polysulfone hollow fibers. II. Morphology. *Journal of Applied Polymer Science*, 1977. **21**(1): 165-180.

[32] Boom, R., I. Wienk, T. Van den Boomgaard, and C. Smolders, Microstructures in phase inversion membranes. Part 2. The role of a polymeric additive. *Journal of Membrane Science*, 1992. **73**(2): 277-292.

[33] Chung, T.S., W.H. Lin, and R.H. Vora, The effect of shear rates on gas separation performance of 6FDA-durene polyimide hollow fibers. *Journal of Membrane Science*, 2000. **167**(1): 55-66.

[34] Chung, T.S., J.J. Qin, and J. Gu, Effect of shear rate within the spinneret on morphology, separation performance and mechanical properties of ultrafiltration polyethersulfone hollow fiber membranes. *Chemical Engineering Science*, 2000. **55**(6): 1077-1091.

[35] Chung, T.S., S.K. Teoh, W.W.Y. Lau, and M.P. Srinivasan, Effect of shear stress within the spinneret on hollow fiber membrane morphology and separation performance. *Industrial & Engineering Chemistry Research*, 1998. **37**(10): 3930-3938.

[36] Wang, K.Y., T. Matsuura, T.-S. Chung, and W.F. Guo, The effects of flow angle and shear rate within the spinneret on the separation performance of poly (ethersulfone) (PES) ultrafiltration hollow fiber membranes. *Journal of Membrane Science*, 2004. **240**(1): 67-79.

[37] Olanrewaju, K., *Personal communication*. January 2013.

[38] Helfand, E. and G.H. Fredrickson, Large fluctuations in polymer solutions under shear. *Physical Review Letters*, 1989. **62**(21): 2468-2471.

[39] Kramer-Lucas, H., H. Schenck, and B.A. Wolf, Influence of shear on the demixing of polymer-solutions. 1. Apparatus and experimental results. *Makromolekulare Chemie-Macromolecular Chemistry and Physics*, 1988. **189**(7): 1613-1625.

[40] Kramer-Lucas, H., H. Schenck, and B.A. Wolf, Influence of shear on the demixing of polymer-solutions. 2. Stored energy and theoretical calculations. *Makromolekulare Chemie-Macromolecular Chemistry and Physics*, 1988. **189**(7): 1627-1634.

[41] Wolf, B., Thermodynamic theory of flowing polymer solutions and its application to phase separation. *Macromolecules*, 1984. **17**(4): 615-618.

[42] Larson, R.G., Flow-induced mixing, demixing, and phase-transitions in polymeric fluids. *Rheologica Acta*, 1992. **31**(6): 497-520.

[43] Kume, T., T. Hashimoto, T. Takahashi, and G.B. Fuller, Rheo-optical studies of shear-induced structures in semidilute polystyrene solutions. *Macromolecules*, 1997. **30**(23): 7232-7236.

[44] Wu, X.L., D. Pine, and P. Dixon, Enhanced concentration fluctuations in polymer solutions under shear flow. *Physical Review Letters*, 1991. **66**(18): 2408-2411.

[45] Ver Strate, G. and W. Philippoff, Phase separation in flowing polymer solutions. *Journal of Polymer Science: Polymer Letters Edition*, 1974. **12**(5): 267-275.

[46] Milner, S.T., Dynamical theory of concentration fluctuations in polymer solutions under shear. *Physical Review E*, 1993. **48**(5): 3674-3691.

[47] Doi, M. and A. Onuki, Dynamic coupling between stress and composition in polymer solutions and blends. *Journal de Physique II*, 1992. **2**(8): 1631-1656.

[48] Saito, S. and T. Hashimoto, Critical conditions for structure formation in semidilute polymer solutions induced under continuous shear flow. *Journal of Chemical Physics*, 2001. **114**(23): 10531-10543.

[49] Rangel-Nafaile, C., A.B. Metzner, and K.F. Wissbrun, Analysis of stress-induced phase separations in polymer solutions. *Macromolecules*, 1984. **17**(6): 1187-1195.

[50] Saito, S., T. Hashimoto, I. Morfin, P. Lindner, F. Boue, and D. Pine, Phase separation in a polymer solution induced by steady and large amplitude oscillatory shear flow. *Macromolecules*, 2003. **36**(10): 3745-3748.

[51] Endoh, M.K., S. Saito, and T. Hashimoto, Shear-induced structures in semidilute polystyrene solution: Effect of solvent quality. *Macromolecules*, 2002. **35**(20): 7692-7699.

[52] Endoh, M.K., M. Takenaka, T. Inoue, H. Watanabe, and T. Hashimoto, Shear small-angle light scattering studies of shear-induced concentration fluctuations and steady state viscoelastic properties. *Journal of Chemical Physics*, 2008. **128**: 164911.

[53] Van Egmond, J., D. Werner, and G. Fuller, Time dependent small angle light scattering of shear induced concentration fluctuations in polymer solutions. *Journal of Chemical Physics*, 1992. **96**: 7742.

[54] Mueller, S., E.W. Llewellin, and H.M. Mader, The rheology of suspensions of solid particles. *Proceedings of the Royal Society. Series A, Mathematical Physical and Engineering Sciences*, 2010. **466**(2116): 1201-1228.

[55] Letwimolnun, W., B. Vergnes, G. Ausias, and P. Carreau, Stress overshoots of organoclay nanocomposites in transient shear flow. *Journal of Non-Newtonian Fluid Mechanics*, 2007. **141**(2-3): 167-179.

[56] Johnson, S.J. and G.G. Fuller, The dynamics of colloidal particles suspended in a second-order fluid. *Faraday Discussions of the Chemical Society*, 1987. **83**: 271-285.

[57] Vermant, J., Large-scale structures in sheared colloidal dispersions. *Current Opinion in Colloid & Interface Science*, 2001. **6**(5-6): 489-495.

[58] Pasquino, R., F. Snijkers, N. Grizzuti, and J. Vermant, Directed self-assembly of spheres into a two-dimensional colloidal crystal by viscoelastic stresses. *Langmuir*, 2010. **26**(5): 3016-3019.

[59] Lyon, M.K., D.W. Mead, R.E. Elliott, and L.G. Leal, Structure formation in moderately concentrated viscoelastic suspensions in simple shear flow. *Journal of Rheology*, 2001. **45**(4): 881-890.

[60] Mewis, J. and N. Wagner, Current trends in suspension rheology. *Journal of Non-Newtonian Fluid Mechanics*, 2009. **157**(3): 147-150.

[61] Phillips, R.J. and L. Talini, Chaining of weakly interacting particles suspended in viscoelastic fluids. *Journal of Non-Newtonian Fluid Mechanics*, 2007. **147**(3): 175-188.

[62] Hwang, W.R. and M.A. Hulsen, Structure formation of non−colloidal particles in viscoelastic fluids subjected to simple shear flow. *Macromolecular Materials and Engineering*, 2011. **296**(3−4): 321-330.

[63] Lively, R., R.R. Chance, W.J. Koros, H. Deckman, and B.T. Kelley, *Sorbent fiber compositions and methods of temperature swing adsorption*. 2013, US Patent 20,130,036,905.

[64] Jeong, H.-K., W. Krych, H. Ramanan, S. Nair, E. Marand, and M. Tsapatsis, Fabrication of polymer/selective-flake nanocomposite membranes and their use in gas separation. *Chemistry of Materials*, 2004. **16**(20): 3838-3845.

[65] Sheffel, J.A. and M. Tsapatsis, A model for the performance of microporous mixed matrix membranes with oriented selective flakes. *Journal of Membrane Science*, 2007. **295**(1): 50-70.

[66] Johnson, J.R., *Scalable techniques for the formation of polymer-nanoplatelet hybrid membranes and characterization thereof*. Ph.D. thesis. 2010.

[67] Scirocco, R., J. Vermant, and J. Mewis, Effect of the viscoelasticity of the suspending fluid on structure formation in suspensions. *Journal of Non-Newtonian Fluid Mechanics*, 2004. **117**(2-3): 183-192.

[68] Pasquino, R., F. Snijkers, N. Grizzuti, and J. Vermant, The effect of particle size and migration on the formation of flow-induced structures in viscoelastic suspensions. *Rheologica Acta*, 2010. **49**(10): 993-1001.

[69] Won, D. and C. Kim, Alignment and aggregation of spherical particles in viscoelastic fluid under shear flow. *Journal of Non-Newtonian Fluid Mechanics*, 2004. **117**(2-3): 141-146.

[70] Santos de Oliveira, I., A. van den Noort, J. Padding, W. den Otter, and W. Briels, Alignment of particles in sheared viscoelastic fluids. *The Journal of Chemical Physics*, 2011. **135**(10): 104902-104902-13.

[71] Santos de Oliveira, I., W. den Otter, and W. Briels, The origin of flow-induced alignment of spherical colloids in shear-thinning viscoelastic fluids. *The Journal of Chemical Physics*, 2012. **137**(20): 204908-9.

[72] DeGroot, J.V., C.W. Macosko, T. Kume, and T. Hashimoto, Flow-induced anisotropic SALS in silica-filled PDMS liquids. *Journal of Colloid and Interface Science*, 1994. **166**(2): 404-413.

[73] Tehrani, M., An experimental study of particle migration in pipe flow of viscoelastic fluids. *Journal of Rheology*, 1996. **40**: 1057.

[74] Fischer, P. and E.J. Windhab, Rheology of food materials. *Current Opinion in Colloid & Interface Science*, 2011. **16**(1): 36-40.

[75] Lewis, J.A., Colloidal processing of ceramics. *Journal of the American Ceramic Society*, 2000. **83**(10): 2341-2359.

[76] Segre, G. and A. Silberberg, Behaviour of macroscopic rigid spheres in Poiseuille Flow. 1. Determination of local concentration by statistical analysis of particle passages through crossed light beams. *Journal of Fluid Mechanics*, 1962. **14**(1): 115-135.

[77] Segre, G. and A. Silberberg, Behaviour of macroscopic rigid spheres in Poiseuille Flow. 2. Experimental results and interpretation. *Journal of Fluid Mechanics*, 1962. **14**(1): 136-157.

[78] Ho, B.P. and L.G. Leal, Inertial migration of rigid spheres in 2-dimensional unidirectional flows. *Journal of Fluid Mechanics*, 1974. **65**(2): 365-400.

[79] Karnis, A., H. Goldsmith, and S. Mason, The flow of suspensions through tubes: V. Inertial effects. *The Canadian Journal of Chemical Engineering*, 1966. **44**(4): 181-193.

[80] Matas, J.-P., J.F. Morris, and E. Guazzelli, Inertial migration of rigid spherical particles in Poiseuille flow. *Journal of Fluid Mechanics*, 2004. **515**(1): 171-195.

[81] Yang, B., J. Wang, D. Joseph, H.H. Hu, T.-W. Pan, and R. Glowinski, Migration of a sphere in tube flow. *Journal of Fluid Mechanics*, 2005. **540**: 109-131.

[82] Pan, T.-W. and R. Glowinski, Direct simulation of the motion of neutrally buoyant balls in a three-dimensional Poiseuille flow. *Comptes Rendus Mécanique*, 2005. **333**(12): 884-895.

[83] Shao, X., Z. Yu, and B. Sun, Inertial migration of spherical particles in circular Poiseuille flow at moderately high Reynolds numbers. *Physics of Fluids*, 2008. **20**(10): 103307.

[84] Choi, C.R. and C.N. Kim, Inertial migration and multiple equilibrium positions of a neutrally buoyant spherical particle in Poiseuille flow. *Korean Journal of Chemical Engineering*, 2010. **27**(4): 1076-1086.

[85] Leighton, D. and A. Acrivos, Shear-induced migration of particles in concentrated suspensions. *Journal of Fluid Mechanics*, 1987. **181**(1): 415-439.

[86] Frank, M., D. Anderson, E.R. Weeks, and J.F. Morris, Particle migration in pressure-driven flow of a Brownian suspension. *Journal of Fluid Mechanics*, 2003. **493**(1): 363-378.

[87] Koh, C.J., P. Hookham, and L. Leal, An experimental investigation of concentrated suspension flows in a rectangular channel. *Journal of Fluid Mechanics*, 1994. **266**: 1-32.

[88] Lyon, M. and L. Leal, An experimental study of the motion of concentrated suspensions in two-dimensional channel flow. Part 1. Monodisperse systems. *Journal of Fluid Mechanics*, 1998. **363**(1): 25-56.

[89] Nott, P.R. and J.F. Brady, Pressure-driven flow of suspensions: simulation and theory. *Journal of Fluid Mechanics*, 1994. **275**: 157-199.

[90] Jiang, L.Y., T.S. Chung, C. Cao, Z. Huang, and S. Kulprathipanja, Fundamental understanding of nano-sized zeolite distribution in the formation of the mixed matrix single- and dual-layer asymmetric hollow fiber membranes. *Journal of Membrane Science*, 2005. **252**(1-2): 89-100.

[91] Xiao, Y., K. Yu Wang, T.-S. Chung, and J. Tan, Evolution of nano-particle distribution during the fabrication of mixed matrix TiO2-polyimide hollow fiber membranes. *Chemical Engineering Science*, 2006. **61**(18): 6228-6233.

[92] Karnis, A. and S. Mason, Particle motions in sheared suspensions. XIX. Viscoelastic media. *Transactions of the Society of Rheology*, 1966. **10**(2): 571-592.

[93] Kim, C., Migration in concentrated suspension of spherical particles dispersed in polymer solution. *Korea-Australia Rheology Journal*, 2001. **13**(1): 19-27.

[94] Matas, J., J. Morris, and E. Guazzelli, Lateral Forces on a Sphere. *Oil & Gas Science and Technology*, 2004. **59**(1): 59-70.

[95] D'Avino, G., F. Snijkers, R. Pasquino, M. Hulsen, F. Greco, P. Maffettone, and J. Vermant, Migration of a sphere suspended in viscoelastic liquids in Couette flow: experiments and simulations. *Rheologica Acta*, 2012(3): 1-20.

[96] Lormand, B. and R. Phillips, Sphere migration in oscillatory Couette flow of a viscoelastic fluid. *Journal of Rheology*, 2004. **48**(3): 551.

[97] Gauthier, F., H. Goldsmith, and S. Mason, Particle motions in non-Newtonian media. *Rheologica Acta*, 1971. **10**(3): 344-364.

[98] Huang, P., J. Feng, H.H. Hu, and D.D. Joseph, Direct simulation of the motion of solid particles in Couette and Poiseuille flows of viscoelastic fluids. *Journal of Fluid Mechanics*, 1997. **343**(1): 73-94.

[99] D'Avino, G., T. Tuccillo, P.L. Maffettone, F. Greco, and M. Hulsen, Numerical simulations of particle migration in a viscoelastic fluid subjected to shear flow. *Computers & Fluids*, 2010. **39**(4): 709-721.

[100] Yang, S., J.Y. Kim, S.J. Lee, S.S. Lee, and J.M. Kim, Sheathless elasto-inertial particle focusing and continuous separation in a straight rectangular microchannel. *Lab on a Chip*, 2011. **11**(2): 266-273.

[101] Leshansky, A., A. Bransky, N. Korin, and U. Dinnar, Tunable nonlinear viscoelastic "focusing" in a microfluidic device. *Physical Review Letters*, 2007. **98**(23): 234501.

[102] Romeo, G., G. D'Avino, F. Greco, P.A. Netti, and P.L. Maffettone, Viscoelastic flow-focusing in microchannels: scaling properties of the particle radial distributions. *Lab on a Chip*, 2013. **13**(14): 2802-2807.

[103] Villone, M., G. D'Avino, M. Hulsen, F. Greco, and P. Maffettone, Numerical simulations of particle migration in a viscoelastic fluid subjected to Poiseuille flow. *Computers & Fluids*, 2011. **42**(1): 82-91.

[104] Villone, M., G. D'Avino, M. Hulsen, F. Greco, and P. Maffettone, Simulations of viscoelasticity-induced focusing of particles in pressure-driven micro-slit flow. *Journal of Non-Newtonian Fluid Mechanics*, 2011. **166**(23): 1396-1405.

[105] D'Avino, G., P.L. Maffettone, F. Greco, and M. Hulsen, Viscoelasticity-induced migration of a rigid sphere in confined shear flow. *Journal of Non-Newtonian Fluid Mechanics*, 2010. **165**(9): 466-474.

[106] D'Avino, G., G. Romeo, M.M. Villone, F. Greco, P.A. Netti, and P.L. Maffettone, Single line particle focusing induced by viscoelasticity of the suspending liquid: theory, experiments and simulations to design a micropipe flow-focuser. *Lab on a Chip*, 2012. **12**(9): 1638-1645.

[107] Macosko, C.W., *Rheology: Principles, Measurements, and Applications*. 1994, New York: Wiley-VCH.

[108] Vermant, J. and M. Solomon, Flow-induced structure in colloidal suspensions. *Journal of Physics: Condensed Matter*, 2005. **17**(4): R187.

[109] Solomon, M. and Q. Lu, Rheology and dynamics of particles in viscoelastic media. *Current Opinion in Colloid & Interface Science*, 2001. **6**(5-6): 430-437.

[110] Kokura, S., O. Handa, T. Takagi, T. Ishikawa, Y. Naito, and T. Yoshikawa, Silver nanoparticles as a safe preservative for use in cosmetics. *Nanomedicine: Nanotechnology, Biology and Medicine*, 2010. **6**(4): 570-574.

[111] Gallegos, C. and J. Franco, Rheology of food, cosmetics and pharmaceuticals. *Current Opinion in Colloid & Interface Science*, 1999. **4**(4): 288-293.

[112] Giesekus, H., Die bewegung von teilchen in strömungen nicht-Newtonscher flüssigkeiten. *Zeitschrift für Angewandte Mathematik und Mechanik*, 1978. **58**: 26.

[113] Grenard, V., N. Taberlet, and S. Manneville, Shear-induced structuration of confined carbon black gels: steady-state features of vorticity-aligned flocs. *Soft Matter*, 2011. **7**(8): 3920-3928.

[114] Hoekstra, H., J. Vermant, J. Mewis, and G. Fuller, Flow-induced anisotropy and reversible aggregation in two-dimensional suspensions. *Langmuir*, 2003. **19**(22): 9134-9141.

[115] Pignon, F., A. Magnin, and J.M. Piau, Butterfly light scattering pattern and rheology of a sheared thixotropic clay gel. *Physical Review Letters*, 1997. **79**(23): 4689-4692.

[116] Lin-Gibson, S., J. Pathak, E. Grulke, H. Wang, and E. Hobbie, Elastic flow instability in nanotube suspensions. *Physical Review Letters*, 2004. **92**(4): 4.

[117] Montesi, A., A.A. Pena, and M. Pasquali, Vorticity alignment and negative normal stresses in sheared attractive emulsions. *Physical Review Letters*, 2004. **92**(5): 58303.

[118] Walker, L.M., W.A. Kernick III, and N.J. Wagner, In situ analysis of the defect texture in liquid crystal polymer solutions under shear. *Macromolecules*, 1997. **30**(3): 508-514.

[119] Peterson, E.C. and V. Breedveld, Shear-induced demixing in polymeric membrane dopes. *Journal of Membrane Science*, 2013. **431**: 131-138.

[120] Breedveld, V., D. van den Ende, R. Jongschaap, and J. Mellema, Shear-induced diffusion and rheology of noncolloidal suspensions: Time scales and particle displacements. *Journal of Chemical Physics*, 2001. **114**(13): 5923-5936.

[121] Bird, R.B., W.E. Stewart, and E.N. Lightfoot, *Transport Phenomena*. 2006: Wiley.

[122] Semwogerere, D. and E.R. Weeks, *Confocal Microscopy*, in *Encyclopedia of Biomaterials and Biomedical Engineering*. 2005, Taylor & Francis: New York.

[123] Magda, J. and R. Larson, A transition occurring in ideal elastic liquids during shear flow. *Journal of Non-Newtonian Fluid Mechanics*, 1988. **30**(1): 1-19.

[124] Fielding, S., Complex dynamics of shear banded flows. *Soft Matter*, 2007. **3**(10): 1262-1279.

[125] Olmsted, P.D., Perspectives on shear banding in complex fluids. *Rheologica Acta*, 2008. **47**(3): 283-300.

VITA

EMILY C. PETERSON

Emily grew up in Bardstown, Kentucky. She received her B.S. in Chemical Engineering from the University of Louisville's J. B. Speed School of Engineering. In addition to rheology research, she enjoys quilting, gardening, and traveling. After completing her Ph.D., Emily will be joining Celanese Corporation in Florence, Kentucky.